

Spring 4-10-2017

ACTIVITY OF PGM-FREE ELECTROCATALYSTS FOR OXYGEN REDUCTION REACTION: PH AND CO- CATALYSIS EFFECTS

Mario Santiago Rojas Carbonell 8148369
University of New Mexico - Main Campus

Follow this and additional works at: https://digitalrepository.unm.edu/cbe_etds

 Part of the [Catalysis and Reaction Engineering Commons](#)

Recommended Citation

Rojas Carbonell, Mario Santiago 8148369. "ACTIVITY OF PGM-FREE ELECTROCATALYSTS FOR OXYGEN REDUCTION REACTION: PH AND CO-CATALYSIS EFFECTS." (2017). https://digitalrepository.unm.edu/cbe_etds/63

This Dissertation is brought to you for free and open access by the Engineering ETDs at UNM Digital Repository. It has been accepted for inclusion in Chemical and Biological Engineering ETDs by an authorized administrator of UNM Digital Repository. For more information, please contact disc@unm.edu.

Santiago Rojas-Carbonell

Candidate

Chemical and Biological Engineering

Department

This dissertation is approved, and it is acceptable in quality and form for publication:

Approved by the Dissertation Committee:

Dr. Plamen Atanassov, Chairperson

Dr. Kateryna Artyushkova

Dr. Alexey Serov

Dr. Fernando Garzon

Dr. Scott Calabrese-Barton

Dr. James Degnan

**ACTIVITY OF PGM-FREE ELECTROCATALYSTS FOR
OXYGEN REDUCTION REACTION: PH AND CO-CATALYSIS
EFFECTS**

by

SANTIAGO ROJAS-CARBONELL

B.S., Chemical Engineering,
Universidad Nacional de Colombia, 2011

M.S., Nanoscience and Microsystems
University of New Mexico, 2013

DISSERTATION

Submitted in Partial Fulfillment of the
Requirements for the Degree of

**Doctor of Philosophy
Engineering**

The University of New Mexico
Albuquerque, New Mexico

May, 2017

DEDICATION

Progress is a joint effort. I dedicate this work to all the people that I have come across in my life, from which I always learned something new. Specially to my parents, Jose Miguel Rojas Cristancho and Gloria Helena Carbonell Rojas. From them, I acquired the curiosity for discovery and the desire for constant advancement.

To my siblings: Emma Inés, Ángela María and Miguel David and the future families that will grow from each one of us.

“If you want to go fast, go alone. If you want to go far, go together.”

African Proverb

ACKNOWLEDGMENTS

I want to thank my mentor and advisor Dr. Plamen Atanassov. He has been an example of an outstanding scientist and leader throughout my studies, an example from which I have learned much more in addition to electrochemistry. I want to thank my committee members Dr. Kateryna Artyushkova, Dr. Alexey Serov, Dr. Fernando Garzon, Dr. Scott Calabrese-Barton and Dr. James Degnan for the enriching discussions that we have had regarding the research presented herein, discussions from which I have been able to learn in abundance and led to this publication.

Also, thanks to Dr. Carlo Santoro, who has been a guide and friend in the process of learning how to move forward with my research. I want to also acknowledge Dr. Sofia Babanova and all my professors during my stay at the University of New Mexico.

My colleagues have been also an important source of knowledge and ideas, and for that reason I am also thankful to them.

The acknowledgement for the financial support for each one of the projects is presented at the end of each chapter.

**ACTIVITY OF PGM-FREE ELECTROCATALYSTS FOR OXYGEN
REDUCTION REACTION: pH AND CO-CATALYSIS EFFECTS**

by

SANTIAGO ROJAS-CARBONELL

B.S., Chemical Engineering,
Universidad Nacional de Colombia, 2011

M.S., Nanoscience and Microsystems,
University of New Mexico, 2013

Ph.D., Engineering,
University of New Mexico, 2017

ABSTRACT

Fuel cells offer a source to the current and always increasing demand for electric power. But as any new technology, there are challenges that need to be addressed to render it feasible for the market place. One of this challenges is finding the appropriate materials to catalyze the oxygen reduction reaction (ORR) that occurs in the cathode. Oxygen is used as an oxidant in a significant portion of the fuel cells due to its readily availability and high reduction potential. Now, one the bottlenecks that stops the large-scale adoption is the expensive and rare metals that have been used as catalysts for this reaction. One solution to this issue came with the development of platinum-metal group free (PGM-free) catalysts, which are composed of abundant and low cost elements like carbon, nitrogen and transition metals.

These PGM-free catalysts have demonstrated their ability to effectively catalyze the ORR in highly alkaline and highly acidic media, as these have been the usual operating conditions for fuel cells that they were developed for.

Due to this success, these PGM-free catalysts have attracted the attention for other applications, like the use in physiological devices or in microbial fuel cells, where the pH is far away from acid or alkaline. This has led to the need to understand how to introduce PGM-free catalyst in fuel cells that operate at pHs around neutrality and to learn about the way their activity towards the ORR is affected by changes in the concentration of hydronium and hydroxyl ions.

The current study addresses these two issues. To begin with, four different transition metals were used in the synthesis of the PGM-free catalysts and tested at neutral pH. It was found that the iron containing PGM-free catalyst provides the highest current densities and lower hydrogen peroxide production. This same PGM-free catalyst was compared against platinum at neutral pH and demonstrated to have higher ORR performance and stability than the precious metal catalyst.

Enzymes like bilirubin oxidase (BOx) catalyze the ORR at pH around neutrality, as they were developed by the biological systems to facilitate this reaction within them. The next achievement in this study was to successfully integrate BOx onto the PGM-free catalyst, obtaining a co-catalytic effect. This led to the next discovery, which consisted in unveiling what are the chemical and morphological characteristics of the PGM-free catalyst that make the integration of the BOx optimal.

The closing component of this study is the exploration of the pH effect on the surface chemistry and the electrochemical activity towards the ORR of a PGM-free catalyst. It was found that the pH has an effect in surface chemistry of the PGM-free catalyst and this leads to a change in the kinetic and electron transfer parameters of the catalytic process.

TABLE OF CONTENTS

LIST OF FIGURES	xi
LIST OF TABLES	xvi
LIST OF ABBREVIATIONS	xvii
INTRODUCTION	1
STATEMENT OF OBJECTIVES.....	4
TRANSITION METAL-NITROGEN-CARBON CATALYSTS FOR OXYGEN REDUCTION REACTION IN NEUTRAL ELECTROLYTE.....	5
Abstract	5
Introduction	6
Materials and methods	7
Catalysts preparation	8
Electrochemical measurements and analysis.....	8
Results and discussion.....	10
Disk current, e ⁻ transfer mechanism and H ₂ O ₂ production	10
Effect of loading on ORR kinetics	12
Durability tests Durability	14
Conclusions.....	16
Acknowledgement.....	17
HYBRID ELECTROCATALYSTS FOR OXYGEN REDUCTION REACTION: INTEGRATING ENZYMATIC AND NON-PLATINUM GROUP METAL CATALYSIS.....	18
Abstract	18
Introduction	19

Methods	22
Catalyst synthesis	22
Catalytic ink preparation	23
Rotating ring disc electrode measurements	24
Fabrication of gas-diffusion cathodes	25
Gas-diffusion cathodes testing	25
Results and discussion.....	26
Conclusions.....	38
Acknowledgments	39
INTEGRATION OF PLATINUM GROUP METAL-FREE CATALYSTS AND BILIRUBIN OXIDASE INTO A HYBRID MATERIAL FOR OXYGEN REDUCTION: INTERPLAY OF CHEMISTRY AND MORPHOLOGY	41
Abstract	41
Introduction	42
Experimental Section	46
Catalysts preparation	46
Surface morphology of PGM-free catalysts	48
Pore-size distribution determination for PGM-free catalysts.....	49
Chemical characterization of PGM-free catalysts.....	49
Catalyst ink preparation.....	50
Electrochemical measurements	50
Results and Discussion	51

Electrochemical activity	51
Effect of PGM-free catalyst surface chemistry and morphology on electrochemical performance	55
Effect of surface morphology on electrochemical performance	58
Correlation between PGM-free catalyst surface morphology assessment techniques	62
Conclusions.....	64
EFFECT OF PH ON THE ELECTROCHEMICAL ACTIVITY OF IRON-NICARBAZIN DE-RIVED PGM-FREE ELECTROCATALYSTS FOR OXYGEN REDUCTION REACTION.....	66
Introduction	66
Materials and methods	71
Catalyst synthesis	71
Electrochemical Measurements	73
Chemical Characterization	75
Results And Discussion.....	75
Electrochemical Activity.....	75
Characterization Of Surface Chemistry	80
Correlation Between Surface Chemistry and Electrochemical Activity	88
Conclusions.....	94
List of publications	95
REFERENCES.....	97

LIST OF FIGURES

Figure 1. Disk and ring current densities (a), number of electrons transferred (b) and peroxide yield (c) of Mn, Fe-, Co- and Ni-AAPyr catalysts (loading $600 \mu\text{g cm}^{-2}$ and RRDE speed of 1200 rpm).....	12
Figure 2. Disk and ring current densities (a), number of electrons transferred (b) and peroxide yield (c) of Fe-AAPyr catalysts with different loadings, scan rate of 5 mV s^{-1} at 1200 rpm. (d) Kinetic current densities calculated with the Koutecky-Levich analysis at different rotation speeds for five loadings.....	14
Figure 3. (a) Disk and ring current densities for Fe-AAPyr catalyst after different cycles (loading $600 \mu\text{gcm}^{-2}$), (b) Disk and ring current densities for Pt (nominal loading of 0.04mgcm^{-2}) after different cycles, (c) number of electrons transferred and (d) peroxide yield for Fe-AAPyr catalyst after different cycles. Scan rate of 5mV s^{-1} at 1200 rpm.	16
Figure 4. Schematic representation of the incorporation of bilirubin oxidase with Fe-AAPyr catalyst, making a hybrid material capable of efficient oxygen reduction.....	22
Figure 5. SEM images of Fe-AAPyr/multi-walled carbon nanotubes ink. (a) depicts the abundance of carbon nanotubes and highly porous Fe-AAPyr catalyst. From (b) it can be seen in detail the close interconnection between the highly porous Fe-AAPyr catalyst.....	27
Figure 6. (a) Representative RDE measurements of Fe-AAPyr, BOx immobilized on multi-walled carbon nanotubes, designed in this study hybrid Fe-AAPyr/CNTs-	

BOx composite. Scan rate 10 mV s^{-1} , 0.1 mol dm^{-3} oxygen saturated phosphate buffer with 0.1 mol dm^{-3} KCl (pH 7.5), rotation rate 1600 rpm. (b) RDE measurements of Fe-AAPyr/CNTs-BOx composite at various rotation rates in 0.1 mol dm^{-3} oxygen saturated phosphate buffer with 0.1 mol dm^{-3} KCl (pH 7.5).
 31

Figure 7. Number of electrons transferred and hydrogen peroxide yield (%) per molecule of O_2 reduced. 33

Figure 8. (a) Cyclic voltammetry of 0.5:0.5 Fe-AAPyr/CNTs-BOx electrode in oxygen saturated 0.1 mol dm^{-3} phosphate buffer, 0.1 mol dm^{-3} KCl, pH 7.5. Scan rate 10 mV s^{-1} , 10 cycles. (b) RDE measurements of Fe-AAPyr/CNTs-BOx composite at various rotation rates in 0.1 mol dm^{-3} oxygen saturated phosphate buffer with 0.1 mol dm^{-3} KCl (pH 7.5). 36

Figure 9. Representative potentiostatic polarization curves of three gas-diffusion cathodes: CNTs-Fe-AAPyr with Fe-AAPyr catalyst only, CNTs-BOx, where the enzyme is the catalyst for oxygen reduction reaction and the hybrid system Fe-AAPyr/CNTs-BOx with both of the catalyst being used. 37

Figure 10. Linear sweep voltammetry for ORR with the (a) PGM-free catalysts alone and (b) PGM-free catalyst with the BOx under saturated oxygen; scan rate: 5 mV s^{-1} , rotation rate: 1600 rpm, loading: 0.6 mg cm^{-2} , and pH 7.5 adjusted with 0.1 mol L^{-1} PBS containing 0.1 mol L^{-1} KCl as a supporting electrolyte. The selected design potential of 885 mV vs. RHE is shown as the dashed line. 52

Figure 11. a) Current densities for ORR catalyzed by the PGM-free catalyst alone and the PGM-free material with BOx at the design potential of 885 mV vs. RHE.

b) Magnitude of enhancement of the current density of the hybrid catalysts (the difference between current density with enzyme and without enzyme).....	54
Figure 12. a) ORR current density (j) enhancement vs. nitrogen content in the PGM-free catalysts. b) ORR j enhancement vs. the fraction of nitrogen in pyridinic moieties in the PGM-free materials; inset: diagram of the structure of the pyridinic moiety. c) ORR j enhancement vs. fraction of nitrogen forming pyrrolic moieties; inset: diagram of the structure of the pyrrolic moiety. Nitrogen atoms are represented in green and carbon atoms in gray. All enhanced current densities were measured at the design potential of 885 mV vs. RHE.	56
Figure 13. SEM images of three selected PGM-free catalysts taken at a magnification of 400 K to visually illustrate the differences. These three samples are presented as a representative subset of the PGM-free catalysts that had the lowest (catalyst 1), medium (catalyst 2), and highest (catalyst 3) enhancement when BOx was introduced.....	58
Figure 14. ORR j enhancement vs. percentage of roughness of the PGM-free catalysts for ranges: a) 3–5 nm, b) 2–20 nm, and c) 40–80 nm. Current densities were measured at the design potential of 885 mV vs. RHE	60
Figure 15. Pore-size distribution of the three selected PGM-free catalysts that exhibited the largest differences in terms of ORR j enhancement when BOx was introduced: catalyst 1 (a), catalyst 2 (b), and catalyst 3 (c), indicating the models used for fitting, and the pore range (vertical dashed lines). (d) Percentage of pores within the three selected ranges for the three PGM-free catalysts.	62

Figure 16. SEM images of three of: a) catalyst 1, b) catalyst 2, and c) catalyst 3. Images after applying the DWT by using the 3–5 nm filter of d) catalyst 1, e) catalyst 2, and f) catalyst 3.	63
Figure 17. Fraction of surface roughness of selected catalysts 1, 2, and 3 owed to features in size range (a) 3–5 nm and (b) 10–12 nm as calculated using the DWT vs. relative surface area attributable to pores between (a) 3–5 nm and (b) 10–12 nm as determined by the nitrogen adsorption isotherm using the DFT model.....	64
Figure 18. Disc current density vs potential for the electrolytes having different pH values. Scan rate of 5 mV s ⁻¹ , 1600 RPM and oxygen saturation.	76
Figure 19. Potential for which the ORR current density reaches 0.1 mA cm ⁻² vs Ag/AgCl electrode (a) and vs RHE electrode (b). Half way potential for the ORR vs RHE electrode (c) and vs Ag/AgCl electrode (d).....	77
Figure 20. Relative atomic percent of chemical species at different pH: (a) pyridinic nitrogen, (b), nitrogen coordinated with iron, (c) hydrogenated nitrogen, (d) graphitic nitrogen, (e) protonated nitrogen, (f) nitrogen bound to hydroxyls, (g) carbon singly bound to oxygen, (h) carbon double bounded to oxygen and (i) carboxylic acid functional group. Cluster of groups categorized by pH ranges presented in Table 2 are signaled with the respective circle. Black for the range between pH 2.4 and 6.08. Magenta for the range between 7.23 and 9.8 and blue for the range between 10.56 and 12.48.....	82

Figure 21. (a) logarithm of the kinetic current density as a function of change in pH. (b) Number of electrons transferred as a function of pH. Circles represent the groups defined in table 2.	85
Figure 22. (a) logarithm of the exchange current density vs pH. (b) charge transfer coefficient for the rate limiting step vs pH.	86
Figure 23. Logarithm of the ratio of kinetic current density and electron transfer current density vs pH.	88
Figure 24. Relative percentage of iron-nitrogen species of the PGM-free catalyst after being exposed to the different pHs vs ORR kinetic and electron transfer parameters. (a) Electron transfer coefficient, (b) Exchange current density, (c) kinetic current density, (d) peroxide yield estimated by the ring current, (e) half way potential and (f) potential at 0.1 mA cm^{-2}	89
Figure 25. Relative percentage of pyridinic nitrogen of the PGM-free catalyst after being exposed to the different pHs vs ORR kinetic and electron transfer parameters. (a) Electron transfer coefficient, (b) Exchange current density, (c) kinetic current density, (d) peroxide yield estimated by the ring current, (e) half way potential and (f) potential at 0.1 mA cm^{-2}	91
Figure 26. Relative percentage of pyrrolic nitrogen of the PGM-free catalyst after being exposed to the different pHs vs ORR kinetic and electron transfer parameters. (a) Electron transfer coefficient, (b) Exchange current density, (c) kinetic current density, (d) peroxide yield estimated by the ring current, (e) half way potential and (f) potential at 0.1 mA cm^{-2}	93

LIST OF TABLES

Table 1. List of the techniques used to characterize the PGM-free catalyst and the hybrid catalysts and the information obtained from them.	45
Table 2. Precursors and heat treatment conditions used for the PGM-free catalyst synthesis	47
Table 3. Surface chemistry composition measured by peak deconvolution of XPS spectra.....	55
Table 4. Percentage of surface roughness within the three selected ranges for the PGM-free catalysts analyzed in this study	59
Table 5. Buffers used as electrolytes for each pH value.....	73
Table 6. Summary of the possible chemical groups present in the PGM-free catalysts and the associated pK _a values that have been reported.....	79

LIST OF ABBREVIATIONS

AApyr	Aminoantipyrine
BET	Brunauer–Emmett–Teller
BJH	Barrett–Joyner–Halenda
BOx	Bilirubin Oxidase
CNT	Carbon nanotube
CV	Cyclic voltammogram
DI	deionized water
DWT	discrete wavelet transform
EFC	enzymatic fuel cell
FC	Fuel cell
GDE	Gas diffusional electrode
GDL	Gas diffusional layer
K-L	Koutecky-Levich
LSV	Linear sweep voltametry
MCO	multicopper oxidase
MFC	Microbial fuelcell
M-N-C	Transition metal-nitrogen-carbon
NCB	Nicarbazin
OCP	Open circuit potential
ORR	Oxygen reduction reaction
PBSE	1-pyrenebutanoic acid, succinimidyl ester
PGM	Platinum-group metal
PGM-free	Platinum-group metal free
Pk_a	Logarithmic acid dissociation constant
RDE	Rotating disk electrode
RDS	Rate determining step
RHE	Reversible hydrogen electrode
RRDE	Rotating ring disk electrode
SEM	Scanning electron microscopy
SSM	Sacrificial support method
TBAB	Tetrabutylammonium bromide modified Nafion
UHP	Ultra high purity
XPS	X-ray photoelectron spectroscopy

INTRODUCTION

The current demand for portable power sources has increased the interest in fuel cell technologies, as they provide high power densities and represent a system that can be truly zero emissions. The first fuel cells developed used platinum as a catalyst for the electrochemical reaction, and were a successful power source used to take the man to the moon in the late sixties. The downside of the technology used for space exploration was the use of platinum loadings, which cost and availability rendered this kind of technology unfeasible for widespread applications.

For the cathode side of the fuel cell, where the electrochemically catalyzed oxygen reaction takes place, a group of materials have surged as an alternative to platinum. They are known as platinum-group metal free catalysts (non-PGMs), which are self-supported structures constituted of metal, nitrogen and carbon. The readily available elements that constitute these materials make them a competitive opportunity for this challenge, as they could be the link between the fuel cell performance and the intended price point for market entry. The materials manufactured by our group has been already tested in prototype cars ¹ and are currently in manufacturing scale up by a spin-off company ² with aims on transportation and deployable big power sources.

So far, extensive research has been done on the performance of this group of catalysts at the regular operating conditions of the fuel cells that they were developed for, namely either highly alkaline or acidic, and mechanistic pathways

that the electrochemical reactions follow have been proposed by our and other groups ³⁻⁸. Due to the plurality of chemical species present in these materials, it is of key importance to trace the catalytic performance to the specific chemical moieties that are facilitating the reaction, where the different steps of the oxygen reduction reaction are carried out. We unveiled the importance of particular nitrogen-iron moieties for the ORR ⁹. Along with the interest in the plurality of chemical species that the non-PGMs exhibit ⁸⁻¹¹, come the particular morphology that this carbonaceous materials possess, as they display intricate interconnections of pores ranging from micropores to macropores, and it has been found by our group that the morphology also plays a role in the electrocatalytic activity, as the active sites, which are located along the walls or edges of this pores, need to be accessible for the reagents and easily abandoned by the products of the oxygen reduction reaction, for it to take place in optimal conditions. An imaging model to characterize this materials was proposed by our group ¹².

Until now, the importance of the chemistry and morphology of the PGM-free catalyst have been described, yet, it is still not fully understood how the changes in electrolyte composition alters the catalyst functioning, as this changes are suspected to alter the composition of the chemical species in the surface and neighborhood of the electrode in ways that are not proportional to the changes in the bulk of the electrolyte ¹³⁻¹⁷. These alterations could modify the catalytic ability of this materials, making this problem an interesting challenge in chemical engineering.

This changes in the surface chemistry can originate from either the adsorption of protons, hydroxyl or hydroperoxyl ions or the quasi-specifically adsorbed hydrated cations and the anions coming from salts, which might interact with the electrocatalytic surface and perform the role of spectator species, reducing the activity of the catalyst due to blocking in the active site ^{3,54,13,16}, but also could increase the reaction occurrence if they participate in the reaction, as it has been proposed for the case of the hydroxyl ion ¹⁵.

STATEMENT OF OBJECTIVES

1. Assess the ORR electrochemical activity at neutral pH of PGM-free catalyst containing different transition metals and compare it to platinum in terms of activity and durability.
2. Explore the integration of the highest performing PGM-free catalyst determined from objective 1, with an enzyme that catalyzes the ORR. This with aims to obtain a co-catalytic effect at neutral pHs, enhancing the overall current density and open circuit potential.
3. Determine what are the intrinsic chemical and morphological characteristics of the PGM-free catalysts that would improve the integration of enzymes into the hybrid catalysts studied in objective 2.
4. Unveil what is the impact of changes in pH onto the electrochemical activity of the PGM-free catalysts towards ORR and explore their origin in the changes of surface chemistry of the catalyst itself.

TRANSITION METAL-NITROGEN-CARBON CATALYSTS FOR OXYGEN REDUCTION REACTION IN NEUTRAL ELECTROLYTE

This chapter corresponds to the article published in Electrochemistry Communications. ¹⁸

Santiago Rojas-Carbonell, Carlo Santoro, Alexey Serov, Plamen Atanassov

Abstract

Platinum group metal-free (PGM-free) catalysts based on M-N-C types of materials with M as Mn, Fe, Co and Ni and aminoantipyrine (AAPyr) as N-C precursors were synthesized using sacrificial support method. Catalysts kinetics of oxygen reduction reaction (ORR) was studied using rotating ring disk electrode (RRDE) in neutral pH. Results showed that performances were distributed among the catalysts as: Fe-AAPyr N Co-AAPyr N Mn- AAPyr N Ni-AAPyr. Fe-AAPyr had the highest onset potential and half-wave potential. All the materials showed similar limiting current. Fe-AAPyr had an electron transfer involving 4e⁻ with peroxide formed lower than 5%. Considering H₂O₂ produced, it seems that Co-AAPyr, Mn-AAPyr and Ni-AAPyr follow a 2 × 2e⁻ mechanism with peroxide formed during the intermediate step. Durability test was done on Fe-AAPyr for 10,000 cycles. Decrease of activity was observed only after 10,000 cycles.

Introduction

Oxygen reduction reaction (ORR) at the cathode is often the limiting steps in the reduction reactions happening generally into FCs dealing with fuels like hydrogen^{11,19}. Those limitations have been studied deeply in acidic and alkaline environments but not in neutral media^{11,20–22}. ORR follows different patterns in function of the pH environment in which the reaction occurs. H⁺ and OH⁻ are required to complete the reaction in acidic and alkaline media respectively^{23,24}. Neutral media (pH=7) has a low concentration (10⁻⁷ M) of H⁺ and OH⁻ that affects negatively the ORR kinetics. High overpotentials are shown in the existing literature^{11,20–22}. Microbial fuel cells (MFCs) operate at neutral conditions and room temperature in order to allow bacteria activity and survivor and this lowers the ORR performances. Catalysts are then used to enhance the reaction rate. Three different typologies of catalysts are investigated in MFC^{20–22}. The first one is based on platinum group metals as inheritance of the most studied acidic or alkaline fuel cells. This choice cannot be justified due to the high catalyst cost compared to the low power output produced. Moreover, MFCs operates in very polluted environment and interaction of anions with Pt is known to deactivate the catalytic activity in short time^{25–27}.

The second choice has been introduced in the past years and it concerns the utilization of carbonaceous-based materials but unfortunately overpotentials are very high and kinetics remains weak^{28,29}. The third choice is the utilization of M-N-C types of catalysts in which M can be platinum group metal (PGM)^{30–33} or completely PGM-free with M being an earth abundant transition metal like Mn,

Fe, Co and Ni.M-N-C catalysts were deeply studied in acidic and alkaline media^{9,34–36} and recently the most pursued in neutral media^{20–22,37–41}. PGM-free catalysts showed high performances and durability in long terms operations compared to Pt^{26,27,42}. Only few mechanistic studies showing catalysts kinetics in neutral media are presented in literature focusing on Fe-based^{40,43–45} or carbonaceous catalysts^{46,47}. None of the studies faced the mechanistic activity and the kinetics of M-N-C with M as Co, Ni and Mn that are the other earth abundant metals together with Fe mostly used to substitute the more expensive Pt. Kinetics behavior of those catalysts is quite elusive and not well understood. Moreover, H₂O₂ yield production, electron transfer mechanisms and loading effect on kinetic current density have not been shown for any catalysts working in neutral media. In this work, we studied the kinetics of four PGM-free catalysts based on the same synthetic process and the same precursors (aminoantipyrine) using rotating ring disk electrode (RRDE) method. Disk current, Tafel plots, H₂O₂ production, electron transfer and loading effect on kinetic current density are discussed. Durability test (10,000 cycles) on Fe-AAPyr is presented and a comparison with Pt is shown. This work enhances the understanding of PGM-free catalysts working in neutral conditions.

Materials and methods

Catalysts preparation

Sacrificial support method (SSM) was used to synthesis the catalysts investigated. Aminoantipyrine (AAPyr) was used as organic precursor for the synthesis. ($\text{Fe}(\text{NO}_3)_3 \times 9\text{H}_2\text{O}$, $\text{Co}(\text{NO}_3)_2 \times 6\text{H}_2\text{O}$, $\text{Mn}(\text{NO}_3)_2 \times 4\text{H}_2\text{O}$, $\text{Ni}(\text{NO}_3)_2 \times 6\text{H}_2\text{O}$) were the metallic salts mixed with AAPyr and impregnated with fumed silica ($\sim 250 \text{ m}^2 \text{ g}^{-1}$). Ball milling was used to ground the mixed materials. Heat treatment was then applied in a constant flow (100 mL min^{-1}) of UHP nitrogen. Temperature was raised till $950 \text{ }^\circ\text{C}$ ($25 \text{ }^\circ\text{C min}^{-1}$) and stabilized for 30min. After pyrolysis, the mixture was cool down at room temperature and silica was etched using 20 wt % HF for 12 h. The catalyst was washed and then dried overnight. Obtained catalysts were named in function of the metal used that was Mn, Fe, Co, Ni.

Electrochemical measurements and analysis

Rotating ring disk electrode (RRDE) technique on Mn-AAPyr, Fe-AAPyr, Co-AAPyr, Ni-AAPyr inks was used to evaluate the catalysts kinetics. The inks were prepared uniformly suspending 5 mg of each catalyst into 0.075% of 1100 EW Nafion solution (FuelCellStore, USA) and then sonicating for three times (30 s) for a correct dispersion. Different loadings (50, 100, 200, 400 and $600 \mu\text{g cm}^{-2}$) were tested. Experiments were done in neutral conditions with electrolyte solution composed by potassium phosphate buffer (0.1 M) and KCl (0.1 M). The solution was purged with pure oxygen for over 30 min. RRDE setup allows to measure the disk current produced by the catalysts and also the peroxide produced as intermediate of the $4e^-$ transfer through the ring current. Linear

sweep voltammetry (LSV) was run from 1.08 V to 0.18 V (vs RHE) at scan rate of 5 mV s⁻¹ in separate triplicates. Disk (j_D) and ring (j_R) currents densities are correlated by Eq. (1.1) in which the electrons transferred are estimated.

$$n = \left| \frac{4 \times j_D}{j_D - j_R} \right|$$

Eq 1.1

The estimated electrons transferred are also used for identifying the H₂O₂ produced (%) during the ORR process as showed by Eq. (1.2)

$$x = \frac{4-n}{2} \times 100$$

Eq 1.2

Durability tests were done to Fe-AAPyr (loading 600 μg cm⁻²) cycling 10,000 times from 1.08 V to 0.18 V (vs RHE) at scan rate of 50 mV s⁻¹. The acquisition of the reported LSV (10, 100, 1000, 3000 and 10,000 cycles) was done at scan rate of 5 mV s⁻¹. Koutecky-Levich equation Eq. (1.3) was used and $|j_d|^{-1}$ was plot against ω^{-1} . i_k and n can be extrapolated from the system.

$$\frac{1}{j_d} = \frac{1}{j_k} + \frac{1}{0.62nFC_{O_2}D_{O_2}^{2/3}v^{-1/6}\omega^{1/2}A}$$

Eq 1.3

i_k is the electrode potential dependent kinetic current density of the ORR, n is the average number of electrons transferred per catalytic event (4 is the maximum), F is the Faraday's constant ($96,487 \text{ C mol}^{-1}$), C_{O_2} is the concentration of O_2 in the electrolyte ($1.117E^{-6} \text{ mol mL}^{-1}$), D_{O_2} is the O_2 diffusion coefficient in aqueous media ($1.9E^{-5} \text{ cm}^2 \text{ s}^{-1}$), and ν is the kinetic viscosity of the electrolyte ($0.01073 \text{ cm}^2 \text{ s}^{-1}$), ω is the angular momentum in $\text{rad}\cdot\text{s}^{-1}$, and A is the electrode sectional area.

Results and discussion

Disk current, e⁻ transfer mechanism and H₂O₂ production

Disk currents (Figure 1a), electrons transferred (Figure 1b) and peroxide yields (Figure 1c) are here presented for every catalyst. Different trends can be noticed into the disk current (Figure 1a). Higher onset potential was measured by Fe-AAPyr (0.98 V (vs RHE)) followed by Co-AAPyr (0.892 V (vs RHE)), Mn-AAPyr (0.864 V (vs RHE)) and Ni-AAPyr (0.802 V (vs RHE)). The onset potential trends followed the current densities produced from the kinetic limited region until reaching the transport limited plateau. Fe-AAPyr had the highest disk current followed by Co-AAPyr, Mn-AAPyr and Ni-AAPyr with the latter as the lowest value measured (Figure 1a). Fe-AAPyr, Co-AAPyr and Mn-AAPyr reached a similar diffusion limited current at 0.185 V (vs RHE) quantified as $\approx 4.5 \text{ mA cm}^{-2}$. Ni-AAPyr had current of $\approx 4 \text{ mA cm}^{-2}$ at that same potential. As for the half-wave potential, the trend is as follows: 0.807 V for Fe, 0.782 V for Co, 0.716 V Mn and 0.571 V for Ni. The electrons transferred at 0.185 V (vs RHE) are estimated to be between 3.5 and 4 with exact number of 3.96 for Fe-AAPyr, 3.84 for Co-AAPyr,

3.67 for Mn-AAPyr and 3.64 for Ni-AAPyr (Figure 1b). Interestingly, at higher potentials Co-AAPyr and Ni-AAPyr had lower electron transferred of 3.00 and 2.87 respectively (Fig. 1b). Also Mn-AAPyr had slightly lower number of electron transferred (3.50) at higher potential (Figure 1b). At the contrary, Fe-AAPyr was the only catalysts showing the same electrons transferred (3.96) along the range investigated (Figure 1b). Peak peroxide yield of 50%, 24% and 56% was formed by Co-AAPyr, Mn-AAPyr and Ni-AAPyr respectively at lower overpotentials investigated (Figure 1c). Fe-AAPyr had low production of peroxide quantified in 2–3%. Peroxide data are necessary for further explaining the electron transfer mechanisms involving the catalysts investigated. In fact, Fe-AAPyr seems to have an apparent direct $4e^-$ transfer mechanism, evidenced by low peroxide production. This mechanism is preferred since the maximum number of electrons is electrochemically transferred during the reaction. In contrast, the high peroxide produced at low overpotentials for Co-AAPyr, Mn-AAPyr and Ni-AAPyr indicates that the peroxide intermediate is produced and then electrochemically oxidized to water at higher overpotentials. This allows to speculate that probably those catalysts have $2 \times 2e^-$ transfer mechanisms during ORR. Peroxide production in MFCs is an undesired process since peroxide can negatively affect the electroactive bacteria on the anode electrode. Those results indicated a superior electrocatalytic activity of Fe-AAPyr compared to the other PGM-free catalysts investigated. The origin of such selectivity towards a $4e^-$ mechanism for the Fe based catalyst versus the $2 \times 2e^-$ transfer mechanism for the other metals has been modeled by density functional theory calculations ^{48–50}.

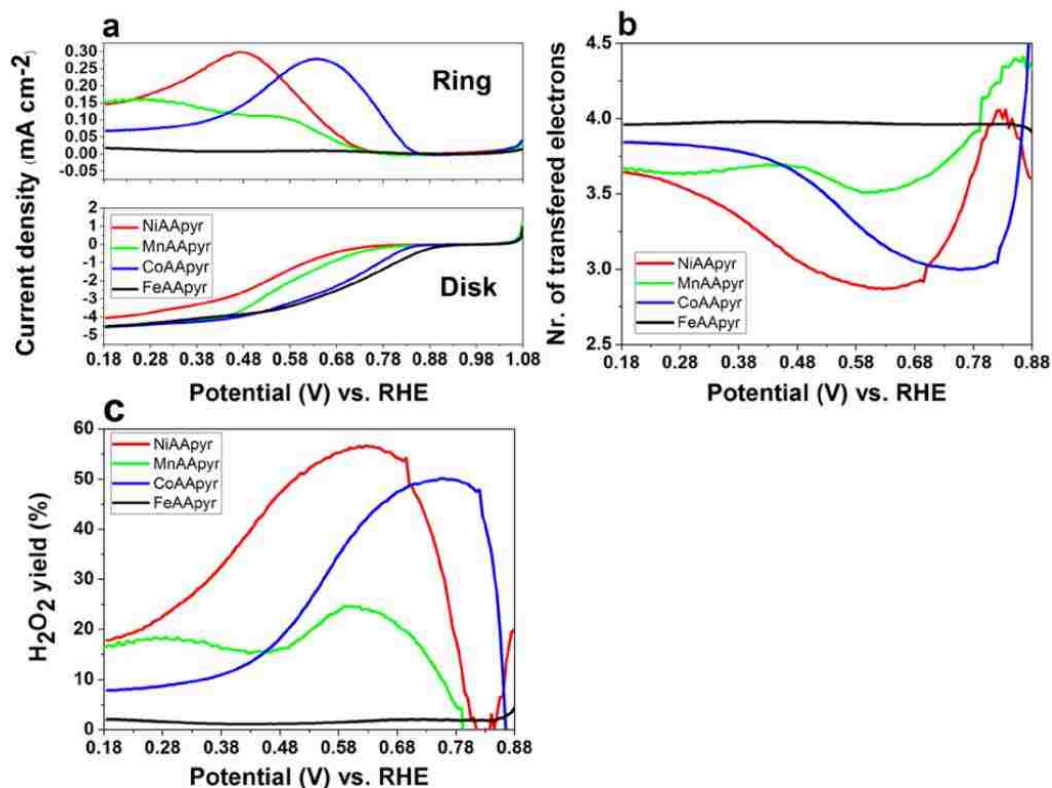


Figure 1. Disk and ring current densities (a), number of electrons transferred (b) and peroxide yield (c) of Mn, Fe-, Co- and Ni-AAPyr catalysts (loading $600 \mu\text{g cm}^{-2}$ and RRDE speed of 1200 rpm).

Effect of loading on ORR kinetics

The effect of the catalyst loading on the ORR kinetics was studied for Fe-AAPyr, as it was the best performing catalysts investigated (Figure 2). Limiting current densities enhanced substantially increasing the loading from 50 to $200 \mu\text{g cm}^{-2}$ (Figure 2a). This indicates that the reaction mechanism of Fe-AAPyr follows a $2 \times 2e^-$ transfer process, as an increase in loading increases the limiting current densities and decreases the peroxide yield (Figure 2c). This is due to a fast H_2O_2 reduction within the catalytic layer, conclusion that is supported by the $4e^-$ transfer mechanism seen at all potentials and loadings (Figure 2b). H_2O_2 peroxide production was always lower than 10% for all the loading investigated.

Peroxide decrease with increase of loading is due to H_2O_2 entrapment inside a thicker catalyst layer, being further reduced before reaching the platinum ring (Figure 2c). Figure 2d displays the kinetic current densities calculated by the Koutecky-Levich analysis for each loading. The increase in kinetic current density between the loadings of 50 and 200 $\mu\text{g cm}^{-2}$ demonstrated that higher availability of active sites within the catalytic layer turn into faster oxygen reduction. This supports the idea of a two-steps electron transfer process, as the peroxide intermediates are more readily reduced to water. A further increase in loading led to a decrease in the kinetic current density, which indicates that probably the reactants are not reaching the active sites fast enough, entrapped inside a thicker catalytic layer. Those results confirm that Fe-AAPyr is an excellent catalyst for ORR in neutral media, yielding high currents and low peroxide evolution.

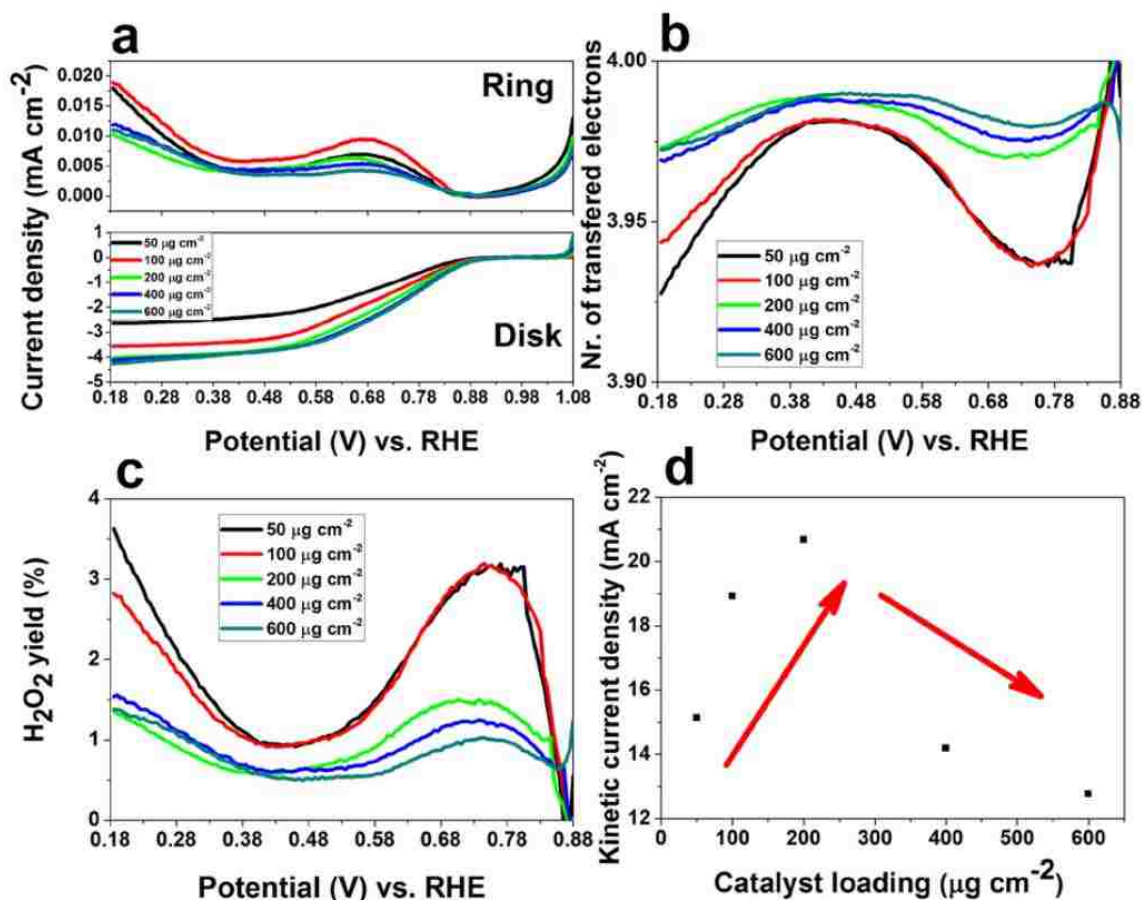


Figure 2. Disk and ring current densities (a), number of electrons transferred (b) and peroxide yield (c) of Fe-AAPyr catalysts with different loadings, scan rate of 5 mV s^{-1} at 1200 rpm. (d) Kinetic current densities calculated with the Koutecky-Levich analysis at different rotation speeds for five loadings.

Durability tests Durability

Durability test was done on Fe-AAPyr catalyst being the best performing PGM-free catalysts here investigated. Cycles number 10, 100, 1000, 3000 and 10,000 are represented (Figure 3a). Disk current does not change importantly in the first 3000 cycles but only after 10,000 cycles, which is an indicator of the high stability of the catalyst (Figure 3a). A reduction of only 2.5% in limiting current was detected between cycle 100 and 3000 and an additional 5% till cycle 10,000 (Figure 3a). For the case of platinum (Figure 3b), there was a decrease of 30% in

the limiting current density between the cycle 1000 and 3000 and then an additional 40% decrease between the cycle 3000 and 10,000. This indicates the superior stability of Fe-AAPyr over Pt. Half-wave potential decreased 30% at the 10,000-cycle compared to the beginning of life. This could point towards the degradation of the active sites that carry out the first step of the reaction, the reduction of oxygen to peroxide. The overall number of electron transferred during the reaction was ≈ 3.8 after 10,000 cycles (Figure 3c). In contrast, the peroxide production decreased as the durability test progressed (Figure 3d), dropping from a yield of 9% (10 cycles) to 5% (10,000 cycles). The decrease is most significant between 100 cycles and 1000 cycles. This phenomenon can be explained by the leaching of peroxide forming species from the Fe-AAPyr catalyst during the cycles. Fe-AAPyr showed high durability in neutral media with a 30% decrease of the half-wave potential after 10,000 cycles and relatively stable in H_2O_2 produced.

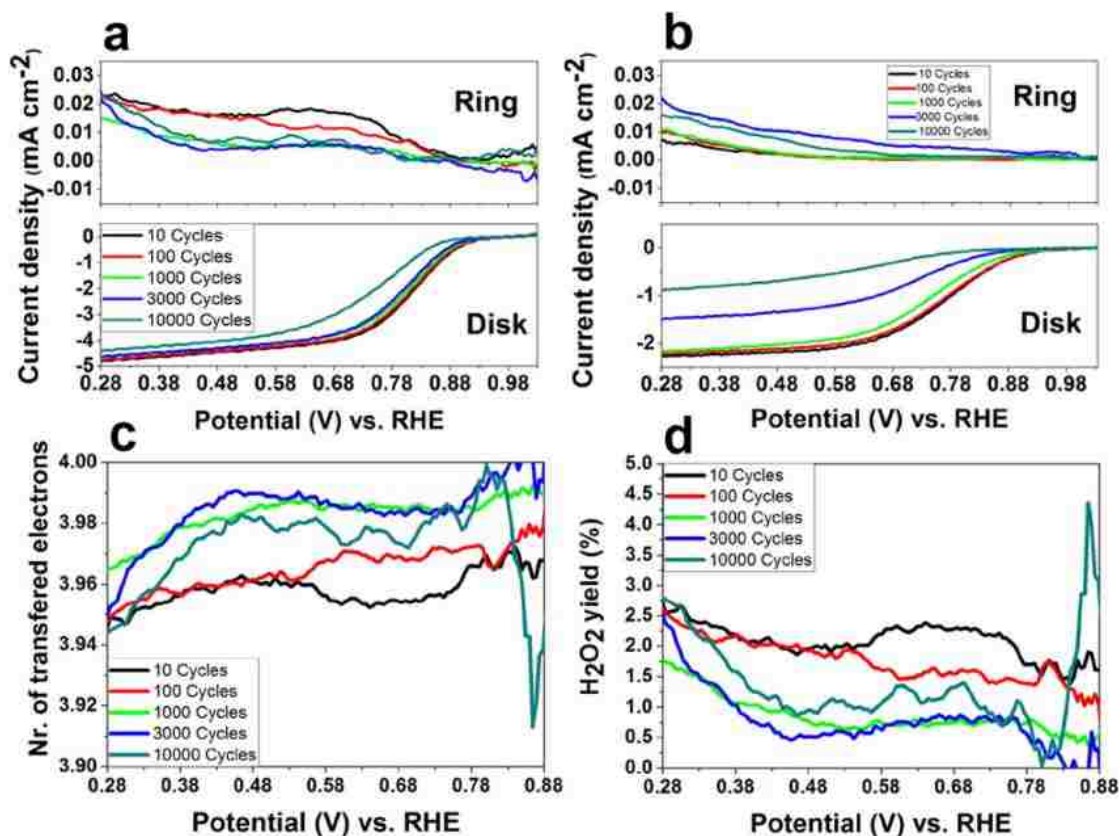


Figure 3. (a) Disk and ring current densities for Fe-AAPyr catalyst after different cycles (loading 600 μgcm^{-2}), (b) Disk and ring current densities for Pt (nominal loading of 0.04 mgcm^{-2}) after different cycles, (c) number of electrons transferred and (d) peroxide yield for Fe-AAPyr catalyst after different cycles. Scan rate of 5 mV s^{-1} at 1200 rpm.

Conclusions

The effect of the metal towards the ORR catalytic activity was investigated. Fe-AAPyr, Co-AAPyr, Mn-AAPyr and Ni-AAPyr kinetics were compared using the RRDE technique. Results showed that Fe-AAPyr had higher current densities obtained compared to the other catalysts. Fe-AAPyr followed an apparent 4e⁻ transfer mechanism, with low H₂O₂ produced. Electrochemical performances of Co-AAPyr, Mn-AAPyr and Ni-AAPyr showed lower output and electron transfer mechanism that can be speculated as 2 × 2e⁻ mechanism, in which the second step is not as fast as in the iron containing catalyst. Fe-AAPyr was cycled 10,000

times and stability parameters were studied. Current density decreased 7.5% between the beginning and the end of the 10,000 cycles test. Fe-AAPyr can be considered a valuable catalyst for ORR in neutral media due to its high performances, low H₂O₂ yield and high stability in long terms operations. Superior stability of the PGM-free catalyst was demonstrated when compared with Pt.

Acknowledgement

This work was supported by the Bill & Melinda Gates Foundation (OPP1139954).

HYBRID ELECTROCATALYSTS FOR OXYGEN REDUCTION REACTION: INTEGRATING ENZYMATIC AND NON-PLATINUM GROUP METAL CATALYSIS

This chapter corresponds to the article published in *Electrochimica Acta* ⁵¹.

Santiago Rojas-Carbonell, Sofia Babanova, Alexey Serov, Yevgenia Ulyanova, Sameer Singhal, Plamen Atanassov.

Abstract

For the first time, oxygen reduction reaction has been demonstrated on a system which integrates enzymatic and non-platinum based catalysts simultaneously. This achievement is of a great importance as it offers the possibility of exploring concomitantly two very different types of catalysts, combining the advantages of both in enhancing oxygen reduction reaction rate. The engineered catalytic hybrid material not only possesses lower overpotentials compared to the purely non-PGM catalyst, but also is capable of achieving higher current densities in comparison to purely enzymatic catalyst. The hybrid catalyst undergoes oxygen reduction with the desired 4 electron transfer process, leading to the formation of water as a final product. The achieved current density of 1.2 mA cm^{-2} is believed to be the highest reported for bilirubin oxidase based gas-diffusion cathode reported so far.

Introduction

The development of new generation of medical devices such as pacemakers, insulin pumps and biological sensors, designed for ensuring the survival of individuals with complex medical conditions, led to increased interest in the area of power sources, necessary for continual operation of such devices. The simplest solution, available to researchers at that time, was to introduce a primary battery as a power source. Unfortunately, batteries have finite operational lifetime and must be replaced regularly, which usually involves surgical intervention. With the high risk of introducing the constituents of the battery, that in case of an accidental leak could represent a serious toxic risk for the patient, the first pacemakers were powered by nickel-cadmium (NiCd) batteries ⁵². Later, NiCd power sources were replaced with lithium-iodine (LiI) ones, which although having more advantages and being currently used, share the same drawbacks of the common batteries. The main disadvantage of any battery is the possibility of rapid discharge. When the capacity of the battery is running down, not giving enough time to be replaced, the life of the user is put at risk ⁵³.

The development of enzymatic fuel cell (EFC) technology sparked immense interest in the area of alternative power sources, and not just for implantable medical devices ^{54,55}. Numerous applications were considered, especially for low power devices in off-grid locations ^{56,57}. EFCs were considered as potential power supplies for charging emergency response kits for camping enthusiasts, powering sensing devices for remote military surveillance or recharging cell

phones in underdeveloped regions of the world. Case in point is Sub-Saharan Africa, where cell phones have become an essential part of communication and commerce in an area where more than 70% of the population does not have access to a stable source of electricity (the grid). This technology could use sugars from ubiquitous sources: fruits, tree sap and even sugar packages, to generate electricity and thus represents a good candidate to face the above-mentioned challenges.

Although EFCs theoretically have great application potential in numerous areas, so far they have been commercially explored only for the design of biosensors. The main reason for that is the low electrical output and short operational stability of these systems⁵⁸. During the years of research in EFCs it has been shown that the performance of the bio-cathode is the limiting factor for the overall system operation⁵⁹. As a result, great efforts have been dedicated to the optimization of the enzymatic cathodes, such as design of gas-diffusion electrodes with improved oxygen supply^{60–63} and/or modification of the electrode surface for enhanced bio/nano interface interactions^{60,64–67}. Currently, the highest performing enzymatic cathodes, which rely on direct electron transfer mechanism, generate current densities in the range of 0.5–0.8 mA cm⁻²^{61,62,67–69} under ambient air conditions and up to 2 mA cm⁻² with pure O₂⁶⁹. Attempts to utilize this technology in microbial fuel cells have conducted to successful outcomes by our group⁷⁰, opening the door for the usage in water purification systems that employ this advances.

The reported herein study is based on the utilization of exceptionally innovative approach for engineering a novel catalytic cathode material. This approach is based on the incorporation of non-platinum (non-PGM) catalyst materials with enzymes, both of which being capable of catalyzing oxygen reduction reaction. The transition metal-nitrogen-carbon material (M-N-C), 4-Aminoantipyrine and iron derived catalyst (Fe-AAPyr), belongs to the group of non-platinum based catalysts synthesized, characterized and optimized by our group^{3,5,34}. This group of catalysts is considered to be most promising candidates for replacing Pt in proton-exchange fuel cells. M-N-C catalysts, synthesized from metal salt and nitrogen/carbon precursor molecules, are capable of carrying out oxygen reduction reaction with efficiencies comparable to Pt, especially at high pHs⁷¹. The newly developed approach of making M-N-C type of catalysts based on the so called “Sacrificial Support Method” allows achieving high density of active sites, easily accessible to oxygen, as well as mitigating the problem with water management^{4,35,72}. The low cost of and availability of the precursors used for the synthesis process makes M-N-C catalysts highly desirable materials for oxygen reduction reaction. This is of prominent importance when designing fuel cells that will be employed in commercial devices. Although M-N-C materials by themselves are state of the art cathodic catalysts, the oxygen reduction carried out by them is characterized with high overpotential at neutral pH, which limits their application in fuel cells operating in physiological conditions. To overcome the disadvantages of purely enzymatic and purely inorganic ORR catalysis, Bilirubin Oxidase and Fe-Aminoantipyrine (Fe-AAPyr) catalyst were incorporated into the

design of enzymatic/inorganic “hybrid” electrode for ORR (Figure 4), which demonstrates low overpotential and increased current densities in a broad range of potentials, under neutral conditions.

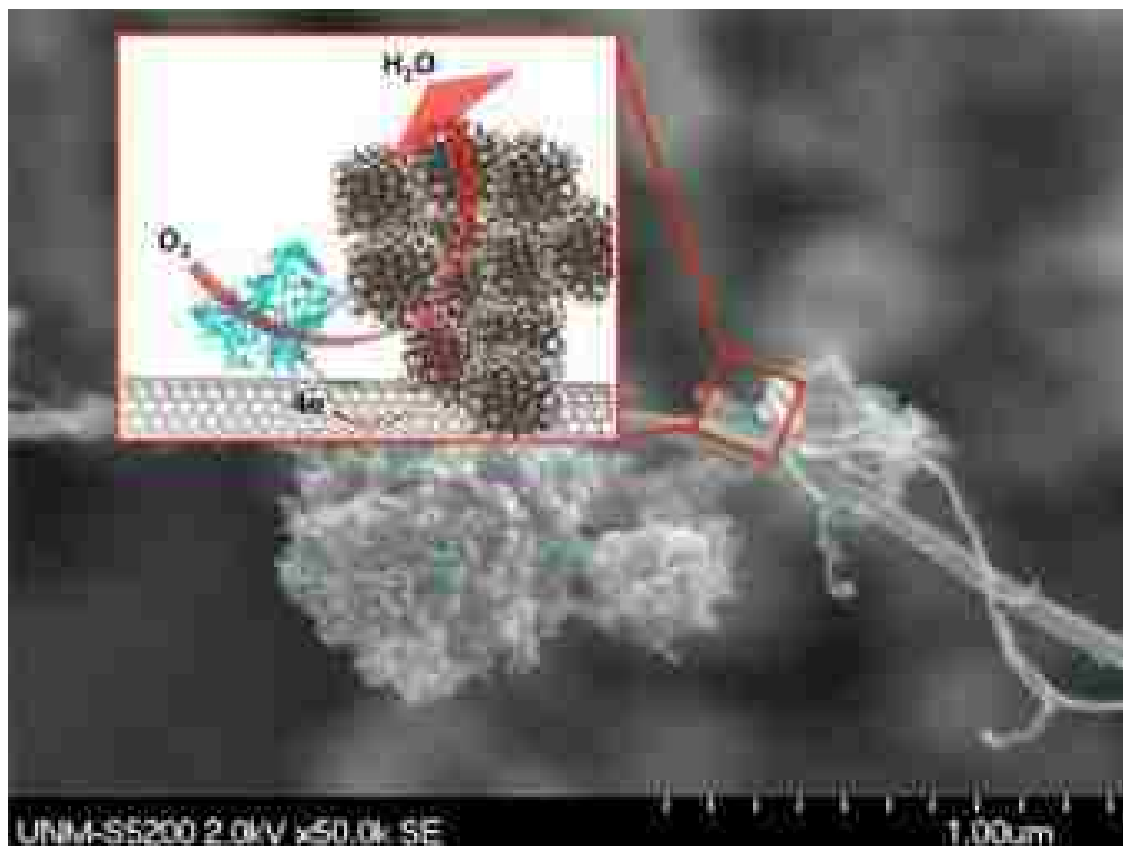


Figure 4. Schematic representation of the incorporation of bilirubin oxidase with Fe-AAPyr catalyst, making a hybrid material capable of efficient oxygen reduction.

Methods

Catalyst synthesis

Fe-AAPyr catalyst was synthesized using the sacrificial support method (SSM) developed previously by our group^{3,34}. This procedure consisted of wet impregnation of the carbonaceous support and iron precursors (4-Aminoantipyrine and Fe(NO₃)₃·9H₂O, both purchased from Sigma Aldrich) over

the surface of fumed silica (Cab-O-Sil™ EH-5, surface area:400 m² g⁻¹). The impregnation occurred under sonication over an 8 hour period of time. Once the suspension was completely homogeneous, it was left to dry at 85 °C for 12 hours, resulting in a solid material that was manually ground using an agate mortar in to fine powder. The powder was then pyrolyzed under UHP nitrogen atmosphere (flow of 100 cc min⁻¹) at 800 °C, with a heating rate of 3 °C min⁻¹. After pyrolysis, the silica support was etched from the catalyst using a hydrogen fluoride solution (37%, Sigma Aldrich) over a 12 hours period. The excess of HF was washed by DI water until neutral pH and powder was dried overnight at $T = 85$ °C.

Catalytic ink preparation

Suspensions of 9.5 mg ml⁻¹ Fe-AAPyr with various Fe-AAPyr: multi-walled carbon nanotubes (MWNT) ratios in water were prepared. Tetrabutylammonium bromide modified Nafion (TBAB-Nafion, kindly provided by Dr. Shelley Minter from The University of Utah) was then added to the suspensions to provide adhesion of the ink to the electrode surface. The modified Nafion was dissolved in ethanol before the addition of the catalyst suspension and had a concentration of 79.3 mg ml⁻¹. The Nafion-containing suspension was sonicated for 30 minutes to ensure complete dispersion. The next step involved addition of 1-pyrenebutanoic acid, succinimidyl ester (PBSE), suspended in ethanol to a final concentration of 10 mmol dm⁻³. The solution was left to react for 1 hour to allow for π - π stacking of the pyrene moiety of the PBSE and the carbonaceous material⁷³. A stock solution (200 mg ml⁻¹) containing Bilirubin Oxidase (BOx,

Amano, Japan) was prepared by dissolving the enzyme in 0.1 mol dm⁻³ phosphate buffer solution (pH 7.5). A 2 µl aliquot of the BOx stock solution was mixed with 48 µl of the suspension from the previous step and left to react for 16–18 hours in order to allow appropriate time for enzyme immobilization.

Rotating ring disc electrode measurements

The rotating ring disc electrode measurements were performed in a 125 mL glass electrochemical cell using a WEB30-Pine bipotentiostat and a Pine Instruments Rotator (Pine Instruments, Raleigh, NC). The experiment was performed in a standard three-electrode setup with platinum wire and Ag/AgCl acting as counter and reference electrodes, respectively.

The working electrode was glassy carbon rotating ring disk electrode covered with 10 µl of the prepared ink. Electrode was allowed to dry completely under ambient laboratory conditions. The disc potential was swept from 0.8 V to -0.1 V vs. Ag/AgCl and the ring was polarized at 1.1 V vs. Ag/AgCl. The scan rate was 10 mV s⁻¹ and a rotating speed of 1600 rpm was chosen to minimize transport limitations. The electrochemical measurements were taken under saturated oxygen conditions. This was achieved by bubbling oxygen through the cell at room temperature and ambient pressure. The electrolyte used for the test was a 0.1 mol dm⁻³ potassium phosphate buffer solution (pH 7.5). Potassium chloride (Sigma Aldrich) was added to this electrolyte to obtain a concentration of 0.1 mol dm⁻³. This buffer solution was prepared in house by using Sigma Aldrich potassium monophosphate and potassium diphosphate and HPLC grade water

(OMNISOLV EMD). The pH of the solution was verified by Omega PHB600R pH meter.

Fabrication of gas-diffusion cathodes

For the fabrication of the gas-diffusion cathodes, the first step consisted of preparing teflonized carbon black materials. The teflonization process was a wet impregnation of Poly(tetrafluoroethylene) (PTFE, Sigma Aldrich) over the carbon black (XC72, Cabot Corporation)⁶².

Carbon black materials with a 35% and 50% of teflonization, named XC35 and XC50 respectively, were individually ground to obtain fine powders. The first layer of the 50% teflonized carbon black (XC50, 75 mg) was placed on top of a nickel mesh (Dexmet Corporation) and manually compacted in a die of 1.5 cm diameter. In a separate container, the ground 35% teflonized carbon black was mixed with the Fe-AAPyr catalyst in a ratio of 72.5: 22.5 XC35: Fe-AAPyr (Fig. S6, in the supplementary information of the paper). This ratio was selected based on the optimization study. The total loading of this layer was 75 mg. This mixture was placed on top of the previously hand pressed XC50 layer and both layers were fused together by pressing with a hydraulic press (Cramer) for 10 minutes at a pressure of 720 psi.

Gas-diffusion cathodes testing

Gas-diffusion electrodes were placed in a polycarbonate hardware for testing. This cell consisted of single chamber cylindrical cell with a diameter of 1.4 cm. The total volume of the chamber was 2.15 cm³. This chamber was open to air on

the side where the gas-diffusion electrode was positioned. The other opening of the chamber was sealed. The electrolyte used for testing was the same one for the RRDE experiments. For the contact with the nickel current collector from the GDE a stainless steel mesh was used. The cell was secured using plastic bolts in order to ensure good electrical connection between the stainless steel support and nickel mesh of the GDE as well as to prevent any possible electrolyte leakage. The counter electrode was a platinum wire (99.9% Sigma Aldrich) with a length of 1.4 cm. The reference electrode, a sealed Ag/AgCl (Dri-Ref Reference Electrode, World Precision Instruments) and the electrochemical measurements were performed with VersaSTAT (Princeton Applied Research) and were done in triplicates to ensure reproducibility.

The SEM images were taken using S-5200 Ultra-High Resolution Field Emission SEM, Hitachi High-Technologies Corporation, Tokyo, Japan.

Results and discussion

BOx belongs to the family of the multicopper oxidases (MCOs) along with Ascorbate Oxidase, Laccase and several others. This enzyme is capable of reducing molecular oxygen to water at the electrode surface⁷⁴⁻⁷⁶. The ORR process is carried out via direct 4 electron transfer, a mechanism that is most desirable and efficient in terms of product and current generation. The integration of BOx into nanomaterial matrix, as previously demonstrated by our research group, preserves the 4e⁻ transfer mechanism of ORR, providing high surface area for enzyme-electrode interactions⁷⁴, where the comparable in size diameter of

carbon nanotubes (CNTs) and BOx enables direct contact of the support material with the enzyme active center ⁷⁵. To further enhance the current output of BOx cathodes, Fe-AAPyr catalyst was incorporated into the CNT-BOx composite. Fe-AAPyr material along with multi-walled carbon nanotubes was used to create a catalytic matrix for BOx immobilization. In Figure 5 we present Scanning Electron Microscope images that show in detail the highly porous Fe-AAPyr catalyst in close contact with the carbon nanotubes. From Figure 5a it is evident the abundance of the two materials and from Figure 5b the close interconnection between the two of them.

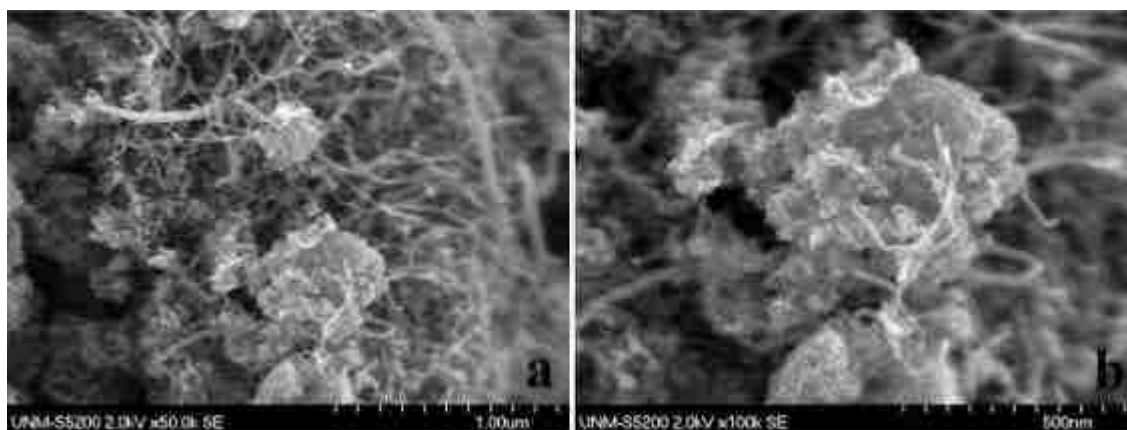


Figure 5. SEM images of Fe-AAPyr/multi-walled carbon nanotubes ink. (a) depicts the abundance of carbon nanotubes and highly porous Fe-AAPyr catalyst. From (b) it can be seen in detail the close interconnection between the highly porous Fe-AAPyr catalyst

Due to the high hydrophobicity of the Fe-AAPyr material, direct immobilization of the enzyme on the catalyst surface was undesirable as it could alter the enzyme tertiary structure. Therefore the M-N-C material was dispersed with CNTs, which provided uniform distribution of the non-platinum based catalysts as well as increased the hydrophilic nature of the surface, making it more “friendly” for enzyme immobilization. The morphology of Fe-AAPyr-CNT hybrid was found to

be similar to previously reported by our group ⁷⁷, where Transmission Electron Microscopy images are presented, along with surface area measurements using Brunauer–Emmett–Teller (BET) methods.

1-pyrenebutanoic acid, succinimidyl ester (PBSE) was utilized for enzyme attachment to the CNTs ^{73,78,79}. Ink, containing Fe-AAPyr, multi-wall carbon nanotubes, modified Nafion ⁸⁰, BOx, PBSE and solvent was fabricated. This ink was deposited on the surface of a glassy carbon rotating ring disk electrode (RRDE) and tested through linear sweep voltammetry at 10 mV s^{-1} in 100 mmol dm^{-3} , oxygen saturated phosphate buffer solution (pH of 7.5) with a rotation of 1600 rpm to guarantee a constant concentration of oxygen at the electrode surface. Controls, fabricated employing either enzyme or Fe-AAPyr-based inks, were also tested in a similar fashion.

The influence of the following parameters on the generated current densities was investigated: (i) ratio of Fe-AAPyr and CNTs; (ii) PBSE and enzyme amounts as well as (iii) time for enzyme immobilization, (Figures S1-S4, in the supplementary information of the paper). An optimal ink composition was established based on the screening process. This ink was composed of Fe-AAPyr and CNTs in 0.5:0.5 ratio (w/w), suspended in TBAB-Nafion solution, which acted as dispersing and binding agent simultaneously. The reason we found for this optimal ratio between the non-platinum metal group catalyst and carbon nanotubes is that we want to have a high loading of the first while allowing a significant amount of the second, as the carbon nanotubes are the anchoring sites where the enzyme will bind to the carbonaceous matrix by means of the tethering agent PBSE, and this binding

is essential to ensure a correct integration between the two catalysts. The optimum enzyme content was determined to be 8 mg ml^{-1} , sufficient enough for notable enzymatic catalysis but not too high to block the non-PGM active centers. It was established that BOx:PBSE ratio exceeding 1:4 does not lead to further improvement of the electrochemical performance, indicating effective immobilization of the total amount of enzyme present in the system, especially after 18 hours of immobilization. The optimized ink demonstrated significantly ($n = 3$, $P = 0.01$) higher current densities throughout the whole potential window tested in comparison to Fe-AAPyr and CNTs-BOx electrodes (Figure 6a). The ORR onset potential of the hybrid system, $E_{\text{onset}} = 0.50 \pm 0.01 \text{ V vs. Ag/AgCl}$, corresponded to the onset potential of the enzymatically catalyzed oxygen reduction, demonstrating enzymatic activity. Thus in comparison to purely Fe-AAPyr catalyst ($E_{\text{onset}} = 0.20 \pm 0.03 \text{ V vs. Ag/AgCl}$), the overpotential of ORR was decreased 2 times. At the same time, the current density of the hybrid catalyst was 2.7 times higher at $-0.10 \text{ V vs. Ag/AgCl}$ as compared to purely enzymatic or inorganic catalysis. It should be mentioned that under neutral pH conditions the enzyme-CNTs composite material possessed notably higher onset potential and current densities than Fe-AAPyr, which was not surprising since Fe-AAPyr has the lowest activity at pH 7⁵. The increased current densities demonstrated by the hybrid catalyst at low potentials as compared to individual catalyst components of the system, most likely resulted from improved dispersion of the Fe-AAPyr in the presence of the enzyme and the CNTs (Fig. S5, in the supplementary information of the paper) along with higher catalytic activity of the M-N-C catalyst at these

potentials. However, current densities obtained at potentials above 0.20 V vs. Ag/AgCl were clearly a consequence of the enzymatic ORR process. Thus, the performance of the hybrid composite material can be separated into two regions: (i) >0.20 V vs. Ag/AgCl where the enzymatic activity ensures high onset potential and current generation and (ii) <0.20 V vs. Ag/AgCl, where the well dispersed Fe-AAPyr is responsible for the current output of the system (Figure 6b).

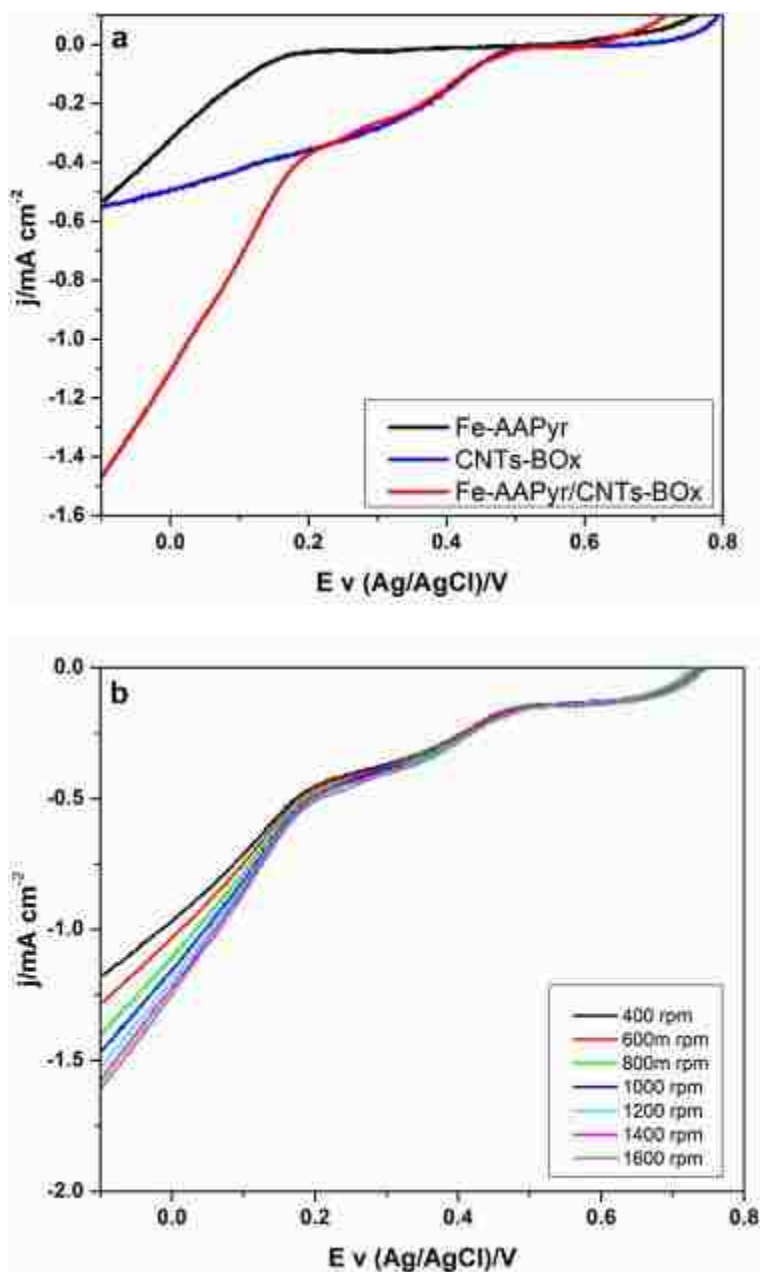


Figure 6. (a) Representative RDE measurements of Fe-AAPyr, BOx immobilized on multi-walled carbon nanotubes, designed in this study hybrid Fe-AAPyr/CNTs-BOx composite. Scan rate 10 mV s^{-1} , 0.1 mol dm^{-3} oxygen saturated phosphate buffer with 0.1 mol dm^{-3} KCl (pH 7.5), rotation rate 1600 rpm. (b) RDE measurements of Fe-AAPyr/CNTs-BOx composite at various rotation rates in 0.1 mol dm^{-3} oxygen saturated phosphate buffer with 0.1 mol dm^{-3} KCl (pH 7.5).

Four electron conversion of oxygen is known for both of the active components of the designed herein hybrid system^{3,74}. During the reduction reaction carried out by BOx, oxygen is directly reduced to water via $4e^-$ transfer⁷⁴. For the M-N-C

catalyst identical reduction process occurs in two steps: $2e^-$ reduction of oxygen to hydrogen peroxide followed by another $2e^-$ reduction of hydrogen peroxide to water³. Four electrons were also shown to be involved in the ORR of the hybrid system at all potentials where ORR was observed (Figure 7). The number of electrons, exchanged during the oxygen reduction were calculated based on charge/mass balance analysis, where the ratio between the current generated as a result of ORR was normalized to the amount of peroxide produced, taking into account the collection efficiency of the Rotating Ring Disk Electrode (RRDE) electrode (Eq. 2.1)⁷⁴:

$$n = \frac{4}{1 + (i_R / \eta i_D)} \quad 2.1$$

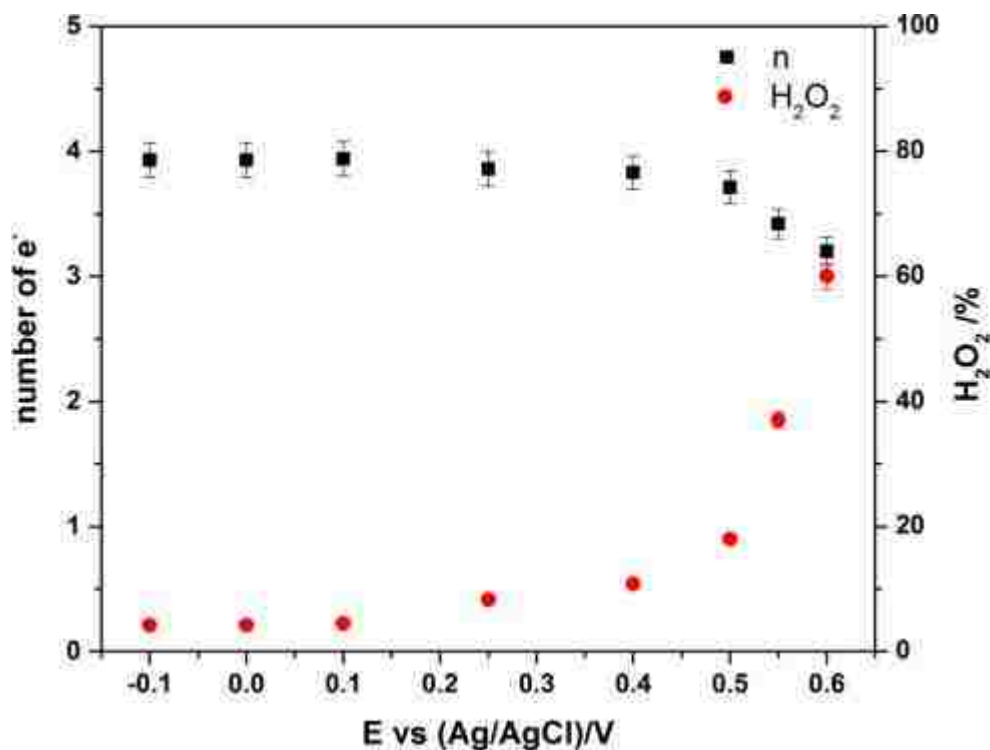


Figure 7. Number of electrons transferred and hydrogen peroxide yield (%) per molecule of O_2 reduced.

The same approach was used to calculate the amount of hydrogen peroxide produced during the oxygen reduction (Eq. 2.2) ⁷⁴:

$$\%H_2O_2 = 100 * \left[\frac{2i_R}{\eta i_D + i_R} \right]$$

Eq. 2.2

where n is the number of electrons transferred, i_R is the ring current, i_D is the disk current and η is collection efficiency of the RRDE (37%) ⁷⁴.

Although RRDE measurements give an indication of the number of electrons being exchanged during the ORR, clear information about the mechanism of the reaction cannot be derived since this method assumes single site mechanism.

However, the 4 electrons calculated demonstrate that the mechanism is not altered towards the production of hydrogen peroxide as a final product. This is evidenced by the percentage of H_2O_2 generated during the ORR (Figure 7). The amount of H_2O_2 decreases below 5% at potentials lower than 0.20 V vs. Ag/AgCl, where the Fe-AAPyr shows activity, indicating the ability of this hybrid catalyst to further reduce H_2O_2 to water³. Furthermore, the H_2O_2 produced does not accumulate, but is further reduced to H_2O by the non platinum based catalyst as it has been determined in our previous study¹⁸. In order to address the impact that the produced peroxide could have over the enzyme activity, a cyclic voltammetry study of the hybrid electrode in oxygen saturated 0.1 mol dm⁻³ phosphate buffer (pH 7.5) has been performed, where 10 cycles were carried out (Figure 8a). As it can be seen, no significant decrease in the generated current was observed after the 6th cycle. The higher current decrease was seen in between the first three cycles, after which the readings in between the cycles overlap. Figure 8b represents the residual activity of the enzyme in the system among the 10 cycles. This residual activity was determined as the percentage decrease in the current recorded at 0.4 V vs. Ag/AgCl. This current can be ascribed to the catalytic activity of the enzyme toward ORR, as the Fe-AAPyr is not active for ORR at this potential. The activity of the enzyme after 10 cycles is still >90% of the initial one, indicating that the small amounts of H_2O_2 being produced during the ORR do not have a notable impact on the enzyme performance. The decrease in the current density among the first cycles can be attributed to the loosening of some of the enzymes that did not get

completely attached to the carbonaceous matrix by means of the PBSE. After this loosely attached enzymes fell off the matrix, the remaining ones, which are the majority as seen from the low decrease in the residual activity during this early cycles, continued their electrochemical activity for the subsequent runs. This, due to the properly anchoring of the remaining BOx molecules by means of the tethering agent.

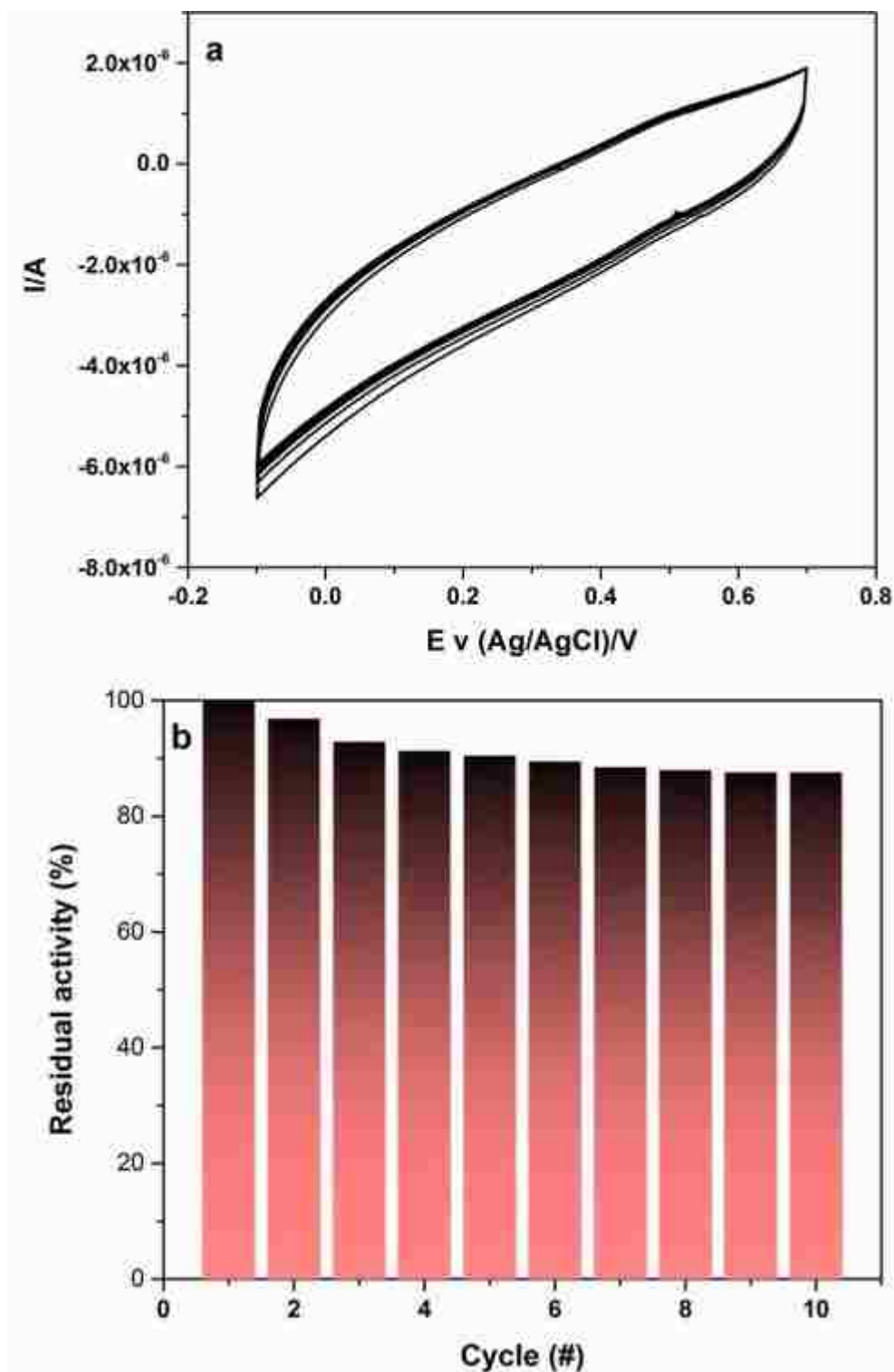


Figure 8. (a) Cyclic voltammetry of 0.5:0.5 Fe-AAPyr/CNTs-BOx electrode in oxygen saturated 0.1 mol dm^{-3} phosphate buffer, 0.1 mol dm^{-3} KCl, pH 7.5. Scan rate 10 mV s^{-1} , 10 cycles. (b) RDE measurements of Fe-AAPyr/CNTs-BOx composite at various rotation rates in 0.1 mol dm^{-3} oxygen saturated phosphate buffer with 0.1 mol dm^{-3} KCl (pH 7.5).

Once the advantage of the hybrid system was demonstrated, the Fe-AAPyr/CNTs-BOx composite was explored in the development of gas-diffusion cathodes for oxygen reduction. The main benefit of this design is the passive supply of oxygen from air through the cathode, which eliminates the need for aerating the electrolyte and provides higher oxygen content, an ideal scenario for commercial application^{81,82}. Potentiostatic polarization curves were carried out to study the performance of the hybrid GDE. Results showed high open circuit potential (OCP), identical to that of the enzymatic cathode and two times increase in the cathode current densities, reaching values far exceeding those of either BOx or Fe-AAPyr electrodes (Figure 9).

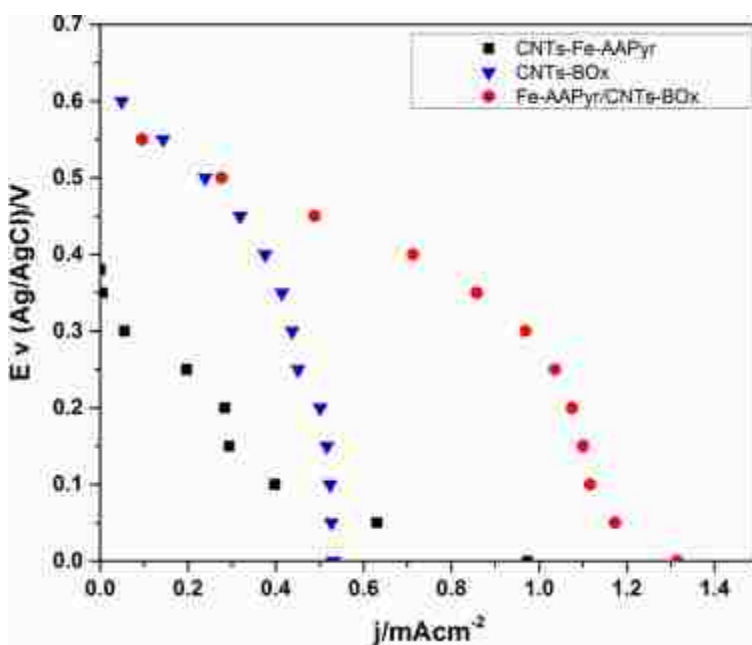


Figure 9. Representative potentiostatic polarization curves of three gas-diffusion cathodes: CNTs-Fe-AAPyr with Fe-AAPyr catalyst only, CNTs-BOx, where the enzyme is the catalyst for oxygen reduction reaction and the hybrid system Fe-AAPyr/CNTs-BOx with both of the catalyst being used.

In contrast to the results from the RDE measurements, no visual separation of the two catalytic processes was observed, suggesting better integration of the

two catalytic units. In addition to the catalytic properties, Fe-AAPyr is a self-supported material with well-developed pore structure. On the mesoscale, pore sizes were 50–70 nm, provided by the diameter of the silica particles used during the synthesis process³. This morphological feature is very important for fuel cell operation in an “air-breathing” mode, where ORR occurs at the gas-liquid-solid tri-phase interface. Furthermore, the hydrophobic character of the non-PGM material facilitates the oxygen diffusion through the electrode. The high surface area of the M-N-C catalyst ($\sim 500 \text{ m}^2 \text{ g}^{-1}$)³ provides also large area of contact with oxygen leading to high current densities, but only at high overpotentials (Figure 8). At the same time, enzymatic gas-diffusion cathode composed of teflonized carbon black as GDL and BOx immobilized on CNTs as catalytic layer shows low overpotential and very high activity at high potentials. Unfortunately, the enzymatic GDE suffers from high mass-transport losses and poor performance at low potentials as evidenced by the shape of the polarization curve. Thus, the integration of BOx and non-platinum based catalyst in the design of GDE not only combines the advantages of the two catalysts but shows dramatically improved performance, demonstrating high current densities throughout the whole potential window tested. The recorded current density of 1.2 mA cm^{-2} is the highest reported for BOx-based gas-diffusion cathode.

Conclusions

The present study demonstrates the successful integration of enzymatic and non-platinum based catalysts into a single hybrid system for ORR. This development is of great importance as it offers the possibility of integrating two

greatly different catalysts and explores the advantages of both in enhancing ORR rate. The performed RRDE measurements show onset potentials of 0.50 ± 0.01 V vs. Ag/AgCl, typical for enzymatic ORR catalysis, along with 2.7 times increase in achievable current densities at the low potential region. Thus, the designed hybrid material possesses lower overpotential when compared to the inorganic portion of the composite and is capable of achieving higher current densities as compared to the enzymatic component of the hybrid catalyst. Both of the described achievements were observed in the design of ink based as well as gas-diffusion cathode. The designed hybrid catalyst undergoes oxygen reduction with the desired 4 electrons being involved in the process, leading to the formation of water as a final product. Along with the success of the integration of the inorganic and enzymatic catalytic units, we also demonstrated that two, so different in nature and operation “materials”, could be explored in the design of advantageous catalysis systems that has not been though as possible so far, opening the door of dramatically improving the operational characteristics of enzymatic electrodes and broadening the areas of their practical application.

Acknowledgments

This research was supported by the U.S. Air Force Research Laboratory (STTR contract FA9550-12-C-0081). The content of this manuscript does not necessarily reflect the position or the policy of the Government, and no official endorsement should be inferred.

We thank Dr. Shelley Minter from The University of Utah, who kindly provided the modified TBAB-Nafion.

INTEGRATION OF PLATINUM GROUP METAL-FREE CATALYSTS AND BILIRUBIN OXIDASE INTO A HYBRID MATERIAL FOR OXYGEN REDUCTION: INTERPLAY OF CHEMISTRY AND MORPHOLOGY

This chapter corresponds to the article published in ChemSusChem⁸³

Santiago Rojas-Carbonell, Dr. Sofia Babanova, Dr. Alexey Serov, Dr. Kateryna Artyushkova, Michael J. Workman, Dr. Carlo Santoro, Alex Mirabal, Prof. Scott Calabrese-Barton, and Prof. Plamen Atanassov

Abstract

Catalytic activity toward the oxygen reduction reaction (ORR) of platinum group metal-free (PGM-free) electrocatalysts integrated with an enzyme (bilirubin oxidase, BOx) in neutral media was studied. The effects of chemical and morphological characteristics of PGM-free materials on the enzyme enhancement of the overall ORR kinetics was investigated. The surface chemistry of the PGM-free catalyst was studied using X-ray Photoelectron Spectroscopy. Catalyst surface morphology was characterized using two independent methods: length-scale specific image analysis and nitrogen adsorption. Good agreement of macroscopic and microscopic morphological properties was found. Enhancement of ORR activity by the enzyme is influenced by chemistry and surface morphology of the catalyst itself. Catalysts with a higher nitrogen content, specifically pyridinic moieties, showed the greatest enhancement. Furthermore, catalysts with a higher fraction of surface roughness

in the range of 3–5 nm exhibited greater performance enhancement than catalysts lacking features of this size.

Introduction

Fuel cell (FC) technology is opening doors to satisfy the environmentally conscious high-energy demand that our modern lifestyles require. FCs have been used for transportation, stationary power systems, and electronic devices. One of the main concerns regarding this promising technology is the high cost and low availability of some of the materials constituting these systems, specifically the anode and cathode catalysts.^{84,85}

Biological FCs are electrochemical devices in which electrochemistry is facilitated by microbes or enzymes. These devices are capable of oxidizing organic molecules and converting the chemical energy directly into electricity.^{86–89} Owing to the presence of biological specimens, operating conditions must remain in the circumneutral window of pH and mild temperature.^{90,91}

Generally, the reduction of an oxidant at the cathode is the limiting step within the biological FC systems.^{92,93} Oxygen is the most utilized oxidizing agent at the cathode as it is readily available in the atmosphere at no cost and possesses relatively high theoretical potential.^{94,95} Nevertheless, the oxygen reduction reaction (ORR) has challenges needed to overcome, such as high overpotentials and slow reaction kinetics. Solving these limitations is difficult as the reaction mechanism at neutral conditions remains uncertain and the reaction proceeds with increased difficulty as pH approaches neutrality.^{26,92,96,97}

Looking to solve these two problems, namely i) slow ORR kinetics and ii) high price of the common catalysts materials, several groups have taken on the task of developing alternative catalysts to replace platinum at the cathode electrode.^{3,35,39,92,98,99} Platinum group metal-free catalysts (PGM-free) are a new class of materials that are comprised of earth abundant transition metal (e.g., Mn, Fe, Co, and Ni), nitrogen, and carbon, making them an affordable and readily available source of materials for ORR in FCs.^{30,39,98–103}

PGM-free materials were successfully demonstrated for the operating conditions of FCs in which the pH is highly acidic or alkaline.^{3,5,7,104–106} Those catalysts were also used to complete ORR in biological systems (e.g., microbial FC, MFC)^{20–22,26,27,37,38,40,43,44,107} at mild operational conditions, neutral pH, and room temperature.

These relatively new applications have raised the need to understand the effect pH has on ORR rate especially for PGM-free materials. Researchers have recently found a shift in the reaction mechanism that coincides with the transition between acidic and basic pH.^{5,96} These same studies also demonstrated that PGM-free catalysts have a minimum in the ORR kinetic current at neutral pH. The reduced kinetics was explained by the low H^+ and OH^- concentration, both participating in the ORR reaction.

It was found that at neutral pH, enzymes such as bilirubin oxidase (BOx), and ascorbate oxidase demonstrate the highest kinetics with overpotentials less than 100 mV.^{57,73,91,108–113} Unfortunately, because of the low turnover number based

on few active centers compared to inorganic catalysts (Pt or PGM-free), enzymes are subject to limiting currents that are quite small, lowering the total current density of the FC.^{70,113}

In summary, the advantages of enzymes over PGM-free compounds are fast kinetics and low overpotentials,^{70,113} whereas the main advantage of PGM-free materials is their higher current density. At the same time, enzymes suffer from low current and PGM-free catalysts are having high overpotentials. To overcome these limitations, herein, we integrated enzymes with PGM-free catalysts.

It was previously demonstrated that there can be a significant increase in performance when PGM-free catalysts are integrated with enzymes and that the performance depends on the integration conditions.^{51,114} To maximize the performance of a hybrid catalyst based on PGM-free material and BOx, the effects of their physiochemical characteristics of the PGM-free catalyst were examined.

Herein, the morphology and chemistry of the PGM-free catalyst were studied, and correlations with electrochemical performance of the hybrid catalyst are reported. Length-scale specific surface morphology is critical to understand the surface environment in which enzyme molecules will be binding. Indeed, ensuring proper anchoring sites will mark the difference between successful and unsuccessful attachment of the enzyme and determine the resulting performance.⁵¹

The surface of the PGM-free material was imaged using scanning electron microscopy (SEM) and characterized by applying discrete wavelet transform (DWT).¹² From this analysis, parameters of surface feature size and connectivity between material particles were studied. Further characterization was performed on nitrogen isotherms using Brunauer–Emmett–Teller (BET), Barrett–Joyner–Halenda (BJH), and density functional theory (DFT) analyses. Correlations between surface analysis, pore-size distributions, and performance enhancement are presented. The surface chemical composition of PGM-free catalyst was studied using X-ray Photoelectron Spectroscopy (XPS). The XPS spectra were analyzed in order to characterize the particular chemical species that PGM-free catalysts possess.⁹ This analysis explored the surface chemistry of PGM-free materials, and how it correlates with performance enhancement when enzymes were integrated. A summary of the characterization techniques and the information found with each one of them is presented in Table 1.

Table 1. List of the techniques used to characterize the PGM-free catalyst and the hybrid catalysts and the information obtained from them.

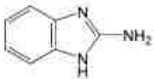
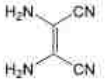
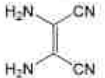
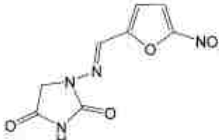
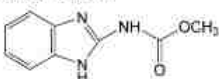
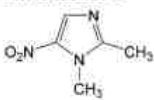
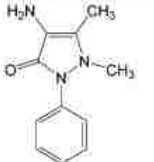
Technique	Variables measured	Information Found
RDE	current density as function of potential in presence and absence of BOx	electrochemical activity toward ORR
XPS	N, O, Fe, C; pyridinic N, pyrrolic N, Fe bound to N, percent of C–C bonds, percent of C–N bonds	percentage of N, C, and Fe chemical species in the PGM-free catalyst surface
SEM	detailed topographic images of the PGM-free catalyst surface to be analyzed with the DWT technique; two magnifications were employed: 25 and 100 K	surface images of the PGM-free showing porous structure with different feature sizes
DWT	ranges of feature sizes: 3–5, 12–20, and 40–80 nm	image-based surface feature size distribution
nitrogen adsorption	BET surface area, BJH pore-size distribution, DFT pore-size distribution	pore-size distribution based on N ₂ adsorption

Experimental Section

Catalysts preparation

PGM-free catalysts were prepared using the Sacrificial Support Method (SSM) with minor modifications from the originally published procedure.^{26,51,72,77} The synthesis method consisted of the wet impregnation of organic precursors, listed in Table 2, onto fumed silica (CAB-O-SIL M5; surface area: $\sim 250 \text{ m}^2 \text{ g}^{-1}$). Iron nitrate ($\text{Fe}(\text{NO}_3)_3 \cdot 9 \text{ H}_2\text{O}$) was added to this mixture as an iron source. The wet suspension was left to dry at $85 \text{ }^\circ\text{C}$ overnight, and then ball milled until a fine powder was obtained. This powder was then heat treated in a controlled atmosphere.

Table 2. Precursors and heat treatment conditions used for the PGM-free catalyst synthesis

PGM-free catalyst	Precursor used	First heat treatment	Second heat treatment ^[a]
catalyst 1	2-aminobenzimidazole 	900 °C, 100 mL.min ⁻¹ N ₂ , 1 hour	950 °C, 100 mL.min ⁻¹ 7% NH ₃ , 0.5 hour
catalyst 2	diaminomaleonitrile 	900 °C, 100 mL.min ⁻¹ N ₂ , 1 hour	950 °C, 100 mL.min ⁻¹ 7% NH ₃ , 0.5 hour
catalyst 3	diaminomaleonitrile 	950 °C, 100 mL.min ⁻¹ 7% NH ₃ , 0.5 hour	950 °C, 100 mL.min ⁻¹ 7% NH ₃ , 0.5 hour
catalyst 4	nitrofurantoin 	900 °C, 100 mL.min ⁻¹ N ₂ , 1 hour	N/A
catalyst 5	carbendazim 	950 °C, 100 mL.min ⁻¹ N ₂ , 0.5 hour	N/A
catalyst 6	dimetridazole 	900 °C, 100 mL.min ⁻¹ N ₂ , 1 hour	N/A
catalyst 7	4-aminoantipyrine 	900 °C, 100 mL.min ⁻¹ N ₂ , 1 hour	N/A

[a] The heating rate for each one of the two heat treatments was 25 °C per minute for all the samples; silica etching after first heat treatment was done with a mixture of hydrofluoric acid (20 wt%) and nitric acid (35 wt%) for 12 hours. [b] N/A signifies that no second heat treatment was applied to that catalyst.

For catalysts 1, 2, 4, 6, and 7, the first heat treatment was done at 900 °C under UHP (ultrahigh purity) nitrogen with a constant flow rate (100 mL.min⁻¹) for a duration of one hour. For catalyst 3, the pyrolysis was performed at 950 °C under ammonia (7 % balanced with nitrogen) with a constant flow rate (100 mL.min⁻¹) and lasting 30 minutes. Last, the pyrolysis of catalyst 5 was done at 950 °C under

UHP nitrogen with a constant flow rate (100 mL min^{-1}) for a duration of 30 minutes. The heating rate for all samples was $25 \text{ }^\circ\text{C}$ per minute, starting from room temperature, and then holding the temperature for specified time, after which the pyrolyzed materials were removed from the furnace to cool down.

After pyrolysis, silica was etched with a solution containing hydrofluoric acid (20 wt %) and nitric acid (35 wt %) for 12 hours and then washed with deionized (DI) water until neutral pH was obtained. The wet samples were dried overnight to remove any water remaining from the washing procedure.

A second heat treatment was applied to catalysts 1, 2, and 3. The conditions of this step were the same for the three samples: $950 \text{ }^\circ\text{C}$ for 30 min under ammonia (7 % balanced with nitrogen) with a constant flow rate of 100 mL min^{-1} . The heating rate was again $25 \text{ }^\circ\text{C}$ per minute.

Surface morphology of PGM-free catalysts

Surface analysis of PGM-free catalysts was performed. The catalyst powders were mounted on conductive carbon tape and imaged in a Hitachi S-5200 ultrahigh resolution (UHR) Field Emission SEM (FE-SEM) at 2 kV in Secondary Electron (SE) mode. The images for analysis were taken at magnifications of 25 and 100 K. Images for visual display were also collected at 300 and 400 K magnification. Images were analyzed using DWT analysis. Wavelet decompositions and analysis calculations were performed using MATLAB with Image Processing Toolbox, Wavelet Toolbox, Optimization Toolbox, and routines previously published.¹² To account for differences in SEM contrast settings and

material interactions with the electron beam, the roughness at each detail level was normalized to the total roughness of the image. This normalization generates a relative fraction of the roughness at each detail level, independent of SEM settings. The surface characteristics of each catalyst were calculated from the average of ten images taken at randomly selected locations.

Pore-size distribution determination for PGM-free catalysts

Nitrogen adsorption–desorption isotherms for PGM-free catalysts were obtained using a Micromeritics ASAP 2020 Nitrogen adsorption analyzer. The surface area was calculated using BET methodology.¹¹⁵ Pore-size distributions were obtained from the isotherms using the BJH¹¹⁶ and nonlocal DFT approaches.^{117–119} BJH calculations were performed using the desorption branch of the isotherm, whereas DFT used the adsorption branch. All samples are smoothed using Accelerated Surface Area and Porosimetry System (ASAP) 2020 software for BJH analysis.

Chemical characterization of PGM-free catalysts

The surface chemistry of PGM-free catalyst powders was studied by XPS. Spectra were acquired at Kratos Axis Ultra DLD spectrometer utilizing Al K α monochromatic sources. Three areas per samples were analyzed. Survey spectra were acquired at 80 eV pass energy, while high resolution O 1s, C 1s, N 1s, and Fe 2p spectra were acquired at 20 eV pass energy. No charge neutralization was necessary. CasaXPS software was used to process the spectra to provide an elemental composition and to curve fit spectra for information on chemical speciation of nitrogen.¹⁰⁹

Catalyst ink preparation

Inks of hybrid catalysts were prepared by mixing individual inks of PGM-free catalysts and BOx. PGM-free inks were created by mixing the catalyst material (5 mg) with DI water (1 mL). Then, Tetrabutylammonium bromide modified Nafion (TBAB-Nafion, kindly provided by Prof. Shelley Minteer, University of Utah) was added to obtain a concentration of 15 wt% ionomer. To ensure complete dispersion, the samples were sonicated three times (3 W for 30 s). The enzyme ink, containing BOx from *Myrothecium verrucaria* (Amano, Japan), was prepared by dissolving BOx in potassium phosphate buffer (PBS, 0.1 mol dm⁻³, pH 7.5) to reach a desired BOx concentration of 200 mg mL⁻¹. The last step for the ink preparation was mixing the PGM-free catalyst suspension (48 μL) with the BOx-containing ink (2 μL). For the test of PGM-free catalyst alone, the ink was prepared to reach the same PGM-free content as for the hybrid catalyst ink.

Electrochemical measurements

Rotating disk electrode (RDE) technique was used for the electrochemical characterization of the inks. Three aliquots (10 μL each) of the catalyst suspensions were drop cast over glassy carbon disk of the RDE and allowed to dry. A loading of 600 μg cm⁻² was reached by applying the 30 μL of the ink. The electrochemical measurements were performed in a 125-mL electrochemical cell using a WEB30-Pine bipotentiostat and a Pine Instruments Rotator (Pine Instruments, Raleigh, NC). The electrolyte was potassium PBS (0.1 mol dm⁻³, pH 7.5) with potassium chloride as supporting electrolyte (0.1 mol dm⁻³). A sealed, saturated Ag/AgCl reference electrode was used. The counter electrode was a

graphite rod. The disk potentials were swept between 1285 and 685 mV vs. RHE (600 and 0 mV vs. Ag/AgCl) with a scan rate of 5 mV s⁻¹. The rotation rate during LSV was 1600 rpm.

Results and Discussion

Synthesis of PGM-free catalysts can be achieved using different organic precursors, each precursor yielding different activity and physiochemical properties of the catalyst.⁹ The precursors for the synthesis of PGM-free materials used in this study were: aminobenzimidazole,⁷⁷ diaminomaleonitrile, nitrofurantoin, carbendazim,⁷² dimetridazole, and aminoantipyrine,²⁶ as shown in Table 2. The catalysts described in Table 2 were tested with and without integration of BOx to explore the interplay of electrochemical interaction, individual electrocatalytic performance in neutral media, and evaluate the influence of surface chemistry and surface morphology of the PGM-free catalysts on enzyme integration and ORR activity.

Electrochemical activity

Linear sweep voltammetry (LSV) was performed to study the electrocatalytic activity of the different PGM-free catalysts (Figure 10). We can see that all tested samples are active toward the ORR with varying levels of performance. The PGM-free catalyst derived from aminobenzimidazole had the highest current density at all potentials tested, whereas the carbendazim-derived catalyst had the lowest. The descending order (according to precursor) of activity for the PGM-free catalyst:

aminobenzimidazole>diaminomaleonitrile>dimetridazole>diaminomaleonitrile>aminoantipyrene>nitrofurantoin>carbendazim. Interestingly, two catalysts derived from the same precursor (diaminomaleonitrile) exhibit different current densities owing to differences in the synthesis procedure and thus different physiochemical properties. These differences are discussed in the following sections.

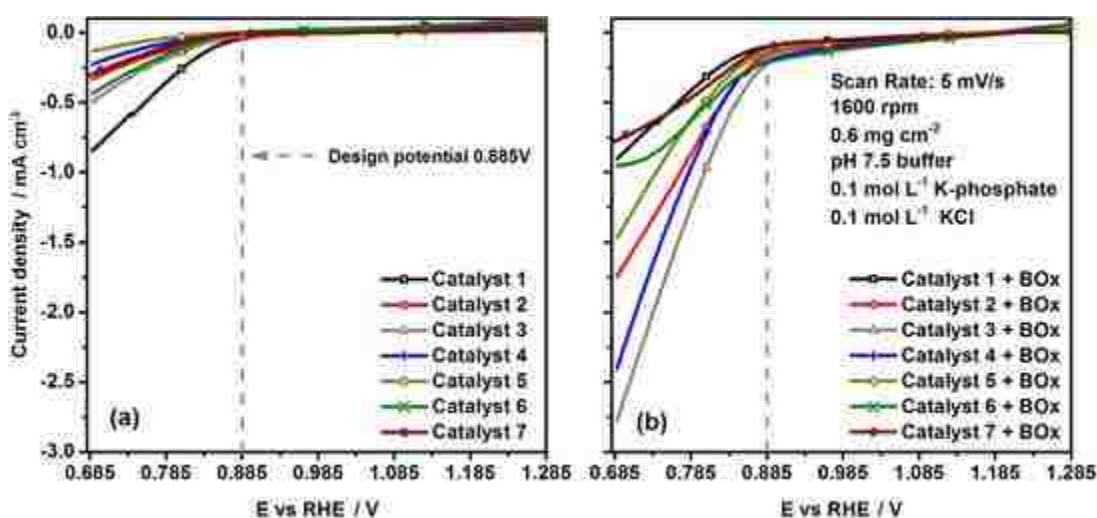


Figure 10. Linear sweep voltammetry for ORR with the (a) PGM-free catalysts alone and (b) PGM-free catalyst with the BOf under saturated oxygen; scan rate: 5 mV s^{-1} , rotation rate: 1600 rpm, loading: 0.6 mg cm^{-2} , and pH 7.5 adjusted with 0.1 mol L^{-1} PBS containing 0.1 mol L^{-1} KCl as a supporting electrolyte. The selected design potential of 885 mV vs. RHE is shown as the dashed line.

Then, the study focused on the integration of enzymes (in this case BOf) with PGM-free catalysts and the resulting change in electrocatalytic activity (Figure 10b). The methodology for the integration of enzymes and PGM-free catalysts was studied and optimized in detail previously,⁵¹ where a significant increase in the operation window for the enzymatic cathode was presented for the first time. In this previous study, we showed a comparison between the activity of BOf, PGM-free material, and a hybrid catalyst obtained after optimizing the formulation for the integration of the two catalysts. Herein, we focus on the role that the

chemical and morphological properties of the PGM-free catalyst play on the integration with BOx.

Figure 10 b illustrates the improvement in the catalytic activity toward ORR that these hybrid catalysts possess as evidenced by a general trend of higher current densities and more positive onset potentials (on average the onset potential shifted from 885 to 1185 mV vs. RHE) compared to the PGM-free catalysts alone. The increase in the onset potential to the value of 1185 mV for all PGM-free catalysts+BOx is an indicator that the enzymatic catalyst is active, as this is the onset potential for ORR catalized by BOx at pH of 7.5.⁵¹ The onset potential of ORR on the PGM-free catalysts is dependent on the materials properties and at this pH is at least 150 mV lower than the enzymatic reaction, as shown in Figure 10a.

A potential of 885 mV versus RHE was chosen as a comparison point for the current densities. This specific value was chosen as it is considered the operational potential for cathodes utilized in enzymatic FCs. The current densities at this potential are displayed in Figure 11 a.

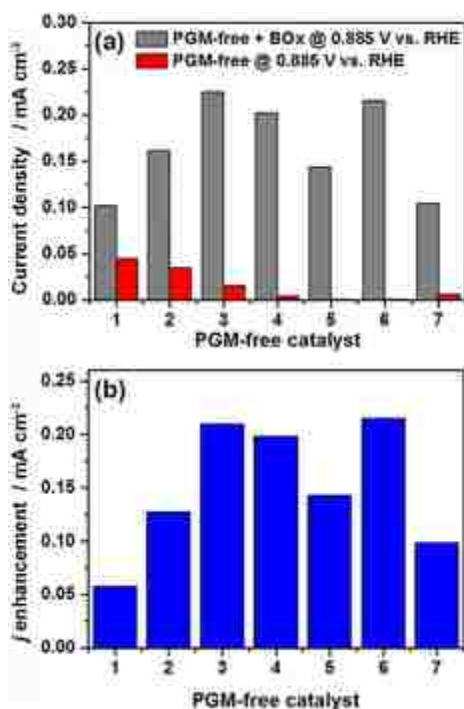


Figure 11. a) Current densities for ORR catalyzed by the PGM-free catalyst alone and the PGM-free material with BOx at the design potential of 885 mV vs. RHE. b) Magnitude of enhancement of the current density of the hybrid catalysts (the difference between current density with enzyme and without enzyme).

The enhancement of the current densities achieved with the introduction of BOx into the PGM-free catalysts is evident from Figure 11 a. The ORR current densities for all hybrid catalysts were several times higher than the PGM-free alone. No correlations were observed between the performance of the PGM-free catalyst alone and either the enhancement effect or total current density with the addition of BOx. This indicates that some characteristics of the PGM-free materials affect their interaction with the enzyme. This is clearly illustrated by Sample 1, which had the highest current density in absence of BOx but the lowest such after adding the enzyme. The magnitude of current density enhancement as a result of enzyme addition was calculated by subtracting the current density obtained by the PGM-free catalyst alone from the current density

of the hybrid catalyst formed by adding BOx to the PGM-free material (Figure 11 b).

Effect of PGM-free catalyst surface chemistry and morphology on electrochemical performance

Surface characterization techniques were employed to study the properties of PGM-free materials and their effect on enzyme/PGM-free catalyst interactions. XPS was used as a surface chemistry characterization tool owing to its ability to elucidate the specific chemical environment of elements in the catalyst. PGM-free materials are composed of nitrogen, carbon, oxygen, and iron forming a plurality of moieties.⁹ Curve fitting and deconvolution were performed as previously reported by Artyushkova et al.¹²⁰ Results of this analysis are detailed in Table 3.

Table 3. Surface chemistry composition measured by peak deconvolution of XPS spectra.

PGM-free catalyst	C [rel %]	N [rel %]	O [rel %]	Fe [rel %]	Pyridinic N [rel %] ^[a]	N bound to Fe [rel %] ^[a]	Pyrrolic N and N oxides [rel %] ^[a]	Aliphatic C [rel %] ^[b]	C–N defects [rel %] ^[b]	Surface C oxides [rel %] ^[b]
catalyst 1	92.6	3.2	4.1	0.09	18.5	11.5	65.2	39.3	12.6	20.3
catalyst 2	88.5	4.5	7.0	0.26	23.7	13.3	57.6	31.7	13.2	26.0
catalyst 3	90.9	5.6	3.4	0.30	24.9	11.0	59.8	31.1	13.2	20.0
catalyst 4	85.3	6.0	8.6	0.16	21.5	20.4	52.4	26.9	15.1	22.7
catalyst 5	88.8	4.7	6.5	0.10	23.6	16.7	56.2	30.2	12.8	20.3
catalyst 6	85.9	8.7	5.3	0.22	22.9	18.2	53.7	25.9	15.7	22.2
catalyst 7	93.7	3.5	2.8	0.10	20.4	11.0	64.6	34.4	12.5	19.4

[a] Relative to total atomic nitrogen. [b] Relative to total atomic %.

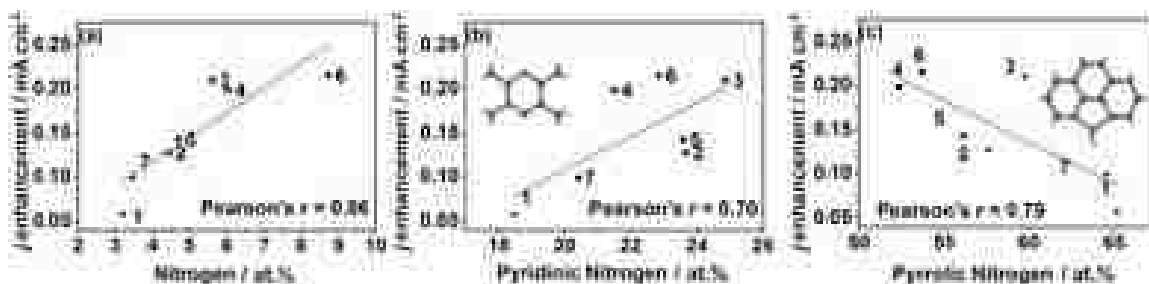


Figure 12. a) ORR current density (j) enhancement vs. nitrogen content in the PGM-free catalysts. b) ORR j enhancement vs. the fraction of nitrogen in pyridinic moieties in the PGM-free materials; inset: diagram of the structure of the pyridinic moiety. c) ORR j enhancement vs. fraction of nitrogen forming pyrrolic moieties; inset: diagram of the structure of the pyrrolic moiety. Nitrogen atoms are represented in green and carbon atoms in gray. All enhanced current densities were measured at the design potential of 885 mV vs. RHE.

From the nine surface chemical moieties measured by XPS, three were found to correlate with current density enhancement of the hybrid catalyst toward (Figure 12): i) the total atomic percentage of nitrogen, ii) the percentage of pyridinic nitrogen relative to the total nitrogen, and the iii) pyrrolic nitrogen and nitrogen oxides. The first relationship showed a positive correlation, giving an increase in the current density of the hybrid catalyst with an increase in the nitrogen atomic percentage (Figure 12a). Previously, it was shown^{9,26,120} that nitrogen is one of the constituents of PGM-free active sites, rendering nitrogen as indispensable for the catalytic activity of this type of catalysts. We can also hypothesize that the higher nitrogen content will lead to increased hydrophilicity of the catalyst, which would provide a “friendly” environment for enzymes. Nitrogen is present as multiple chemical types in PGM-free catalysts.⁹ Correlations between various detected nitrogen species and performance of the hybrid catalysts were also explored. Pyridinic nitrogen was found to have a strong positive correlation with performance. As seen in Figure 12b there is an increase in the current density enhancement of the hybrid catalyst with increasing fraction of nitrogen in pyridinic

form. It was previously reported that pyridinic nitrogen structures are associated with the reduction of the hydrogen peroxide intermediate into water, following a 2 e transfer mechanism.^{9,121} This is beneficial for the integration of the enzyme, as hydrogen peroxide could denaturize the enzyme owing to its ability to act as an oxidizer.^{122,123} Pyrrolic nitrogen is another important species in PGM-free catalysts. It has been reported that the pyrrolic nitrogen reduces oxygen by a 2 e pathway and generates hydrogen peroxide.¹⁰⁹ The results displayed in Figure 12c are consistent with these findings as the increase in pyrrolic moieties led to a decrease in the current density enhancement achieved by the hybrid catalysts. It is interesting to mention that modification of carbon electrodes with a pyrrole-containing organic compound (bilirubin) was found to have a remarkable positive effect on BOx cathodes.^{51,114} Studies previously conducted by our group demonstrated that the significant positive effect observed is owed to an enzyme–substrate recognition event and subsequent proper enzyme orientation,¹²⁴ not to surface chemistry alone. The modification procedure was beneficial for positioning BOx closer relative to the support by providing optimal orientation of the enzyme and facilitating the interfacial electron transfer by decreasing the distance between the electrode surface and the T1 Cu. Both events are not possible with the catalysts discussed herein, thus, the observed positive effect of pyridinic nitrogen lays elsewhere. The high values of the Pearson product-moment correlation coefficient indicate strong correlation between the chemistry of the PGM-free catalyst and the enhanced current density. Still, the correlation is

not exact as the morphology of the PGM-free also plays a role in the magnitude of such enhancement, as discussed later herein.

Effect of surface morphology on electrochemical performance

Analysis of catalyst morphology was achieved through analysis of nitrogen adsorption isotherms, SEM imaging, and DWT analysis. Image-based morphological characterization of the PGM-free catalysts was done by acquiring ten SEM images at 25 and 100 K magnifications for each material. From the SEM images, length-scale specific roughness was calculated. Visual exemplification of the measured differences can be seen in Figure 13.

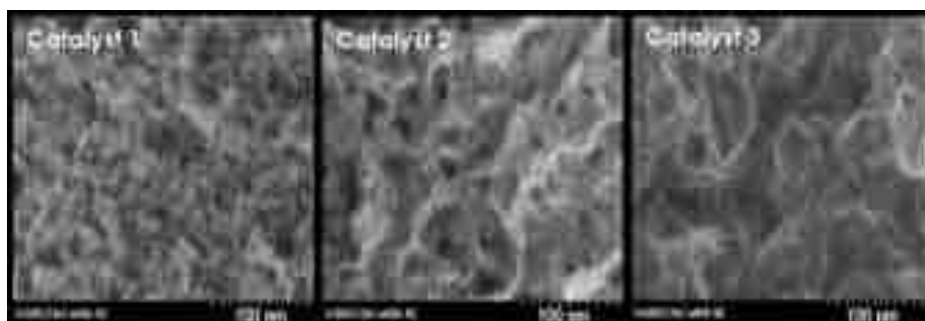


Figure 13. SEM images of three selected PGM-free catalysts taken at a magnification of 400 K to visually illustrate the differences. These three samples are presented as a representative subset of the PGM-free catalysts that had the lowest (catalyst 1), medium (catalyst 2), and highest (catalyst 3) enhancement when BOx was introduced.

These three catalysts are selected as a subset of the seven samples, as they represent the highest (catalyst 3, Fe-diaminomaleonitrile), medium (catalyst 2, Fe-diaminomaleonitrile), and lowest (catalyst 1, Fe-aminobenzimidazole) enhancement when BOx was introduced. To obtain quantitative length-scale specific surface morphology of the PGM-free catalysts, the DWT was applied to SEM images at 25 and 100 K magnification for each one of the seven samples, for a total of 140 SEM pictures. Data for each sample are the average of 10

images from randomly selected locations. This technique has previously been successfully employed to determine feature sizes from SEM images¹² and allowed us to extract discrete waves for three specific dimension ranges from the SEM images. From these discrete waves, it was possible to estimate the percentage of surface roughness within three selected size ranges for each one of the PGM-free catalysts. These ranges were 3–5, 12–20, and 40–80 nm and are presented in Table 4.

Table 4. Percentage of surface roughness within the three selected ranges for the PGM-free catalysts analyzed in this study

PGM-free catalyst	Range		
	3–5 nm [%]	12–20 nm [%]	40–80 nm [%]
catalyst 1	1.1	5.0	14.3
catalyst 2	1.6	11.2	11.7
catalyst 3	2.2	7.9	13.2
catalyst 4	1.8	7.2	18.7
catalyst 5	1.0	8.8	23.3
catalyst 6	2.1	7.9	20.9
catalyst 7	1.3	6.0	18.1

We believe that surface morphology of the PGM-free catalyst affects its interactions with enzymes. Figure 14a elucidates a positive correlation between an increase in the fraction of features with sizes between 3–5 nm and increase in current density toward ORR facilitated by the hybrid catalyst.

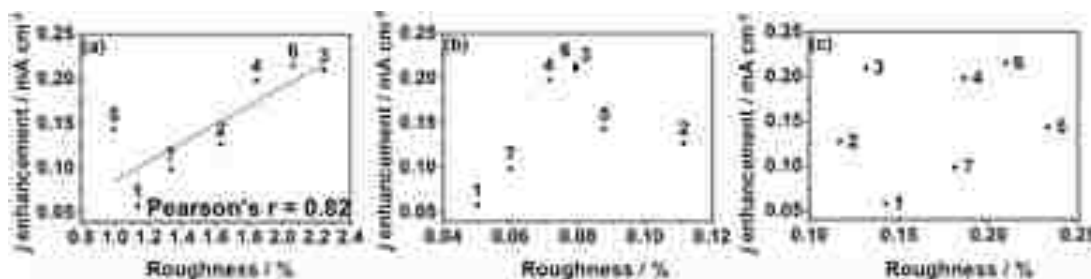


Figure 14. ORR j enhancement vs. percentage of roughness of the PGM-free catalysts for ranges: a) 3–5 nm, b) 2–20 nm, and c) 40–80 nm. Current densities were measured at the design potential of 885 mV vs. RHE

This observation is supported by the high value of the Pearson product-moment correlation coefficient presented in Figure 14a. Still, the correlation is not exact, as the surface chemistry of the PGM-free catalyst was found to also play a role in the magnitude of current enhancement for the hybrid catalyst and described in the previous section. The importance of the features between 3 and 5 nm is highlighted when the crystallographic dimensions of BOx are examined. Cracknell et al.¹²⁵ studied the crystallographic structure of BOx and found it to have an overall size of 5.3, 8.4, and 14.3 nm in each direction. From the results shown in Figure 14a, it is clear that PGM-free catalysts, which possess a higher ratio of pores within 3–5 nm range, provide a better surface for enzyme immobilization and activity without being large enough to envelop the entire enzyme. Also, these pores would favor the longitudinal orientation of BOx, increasing the chances that the T1 center of the enzyme will be aligned with the PGM-free catalyst moieties, thereby increasing the interaction between BOx and PGM-free catalysts. In the case of larger pores, between 12 and 20 and between 40 and 80 nm, no significant trend was found (Figure 14b, c), which is expected as these features would not favor any particular enzyme orientation. Based on

the results of DWT analysis, the importance of surface features between 3–5 nm for enhanced integration of PGM-free materials and BOx has been elucidated. It was previously shown that DWT surface analysis of SEM images correlates with true roughness as measured by atomic force microscopy (AFM).¹² However, this technique does not differentiate between peaks and pores. To verify the above-described results, the pore-size distribution of PGM-free catalyst was determined from nitrogen adsorption isotherms. Nitrogen adsorption isotherms were analyzed with two commonly employed models for the PGM-free materials: the nonlocal DFT and BJH model. In general, the mesopore size range is in good agreement between the two models.¹¹⁷ As the BJH model does not apply to micropores (>2 nm), and the features of interest are close to this limit, analysis using DFT was employed. For nitrogen adsorption isotherm analysis, only the three selected PGM-free catalysts were tested (catalysts 1, 2, and 3). The results obtained after analyzing the nitrogen adsorption isotherms, are shown in Figure 15.

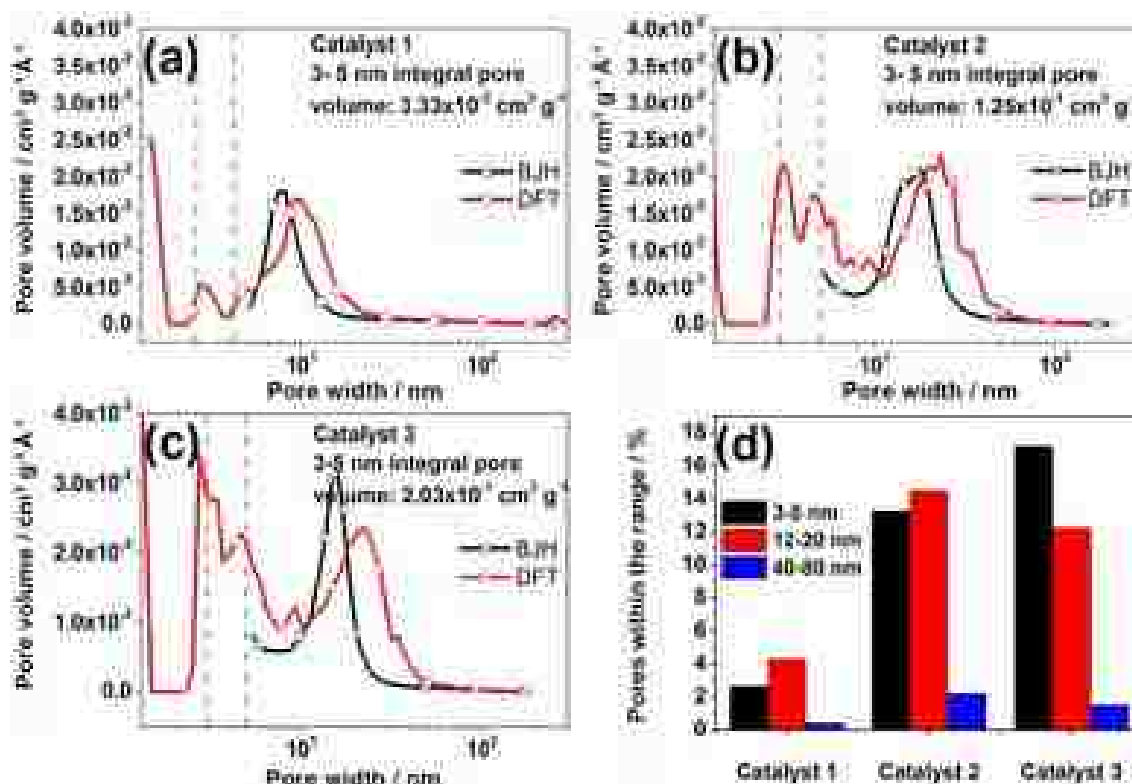


Figure 15. Pore-size distribution of the three selected PGM-free catalysts that exhibited the largest differences in terms of ORR j enhancement when BOx was introduced: catalyst 1 (a), catalyst 2 (b), and catalyst 3 (c), indicating the models used for fitting, and the pore range (vertical dashed lines). (d) Percentage of pores within the three selected ranges for the three PGM-free catalysts.

The DFT model shows an increase in the fraction of pores with sizes between 3–5 nm (range marked with the two-dashed gray parallel lines) from catalyst 1 to 2 to 3. This increase in the volume of pores in this size range is in agreement with the DWT surface analysis and supports the hypothesis that the enzyme is favorably interacting with 3–5 nm pores on the surface of the catalyst.

Correlation between PGM-free catalyst surface morphology assessment techniques

A good agreement between the surface morphology of PGM-free catalysts obtained from image-based DWT and the results from pore-size distribution

assessed by N₂ gas adsorption method was obtained. The relative surface area attributable to pores of a specific size range was determined by dividing the incremental surface area of the pores within the range, determined by the application of the DFT model to the nitrogen adsorption isotherms, by the total surface area established by the same methodology.

A schematic of the DWT approach is presented in Figure 16. Figure 16a–c shows SEM images of three of the PGM-free catalysts and Figure 16d–f shows detail level images extracted by DWT filtering representing details in the 3–5 nm range.

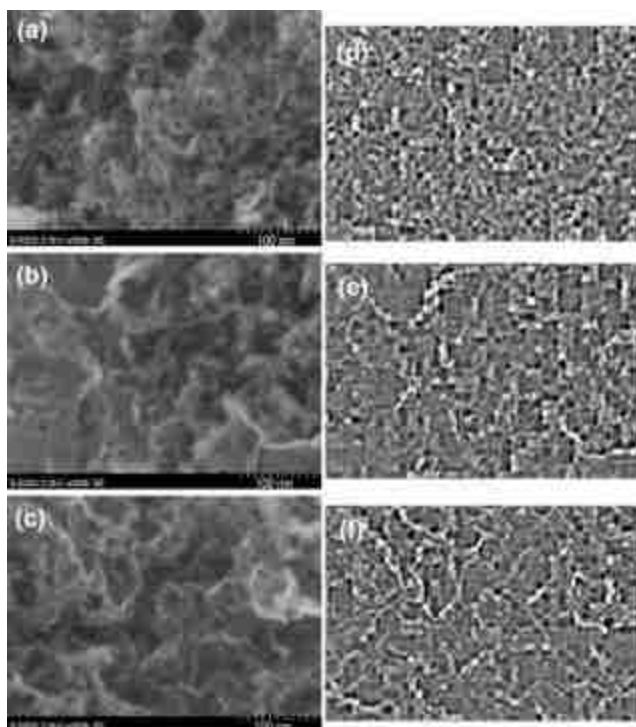


Figure 16. SEM images of three of: a) catalyst 1, b) catalyst 2, and c) catalyst 3. Images after applying the DWT by using the 3–5 nm filter of d) catalyst 1, e) catalyst 2, and f) catalyst 3.

Percentage of surface roughness extracted from DFT (Table 4) between the ranges of 3–5 and 12–20 nm are respectively listed in the ordinates of Figure

17a, b versus the relative surface area calculated from DFT. There is a strong correlation between the results obtained by the DWT and DFT techniques, showing the applicability of DWT as a tool to evaluate the surface morphology of catalysts at the hierarchy of scales using SEM images.

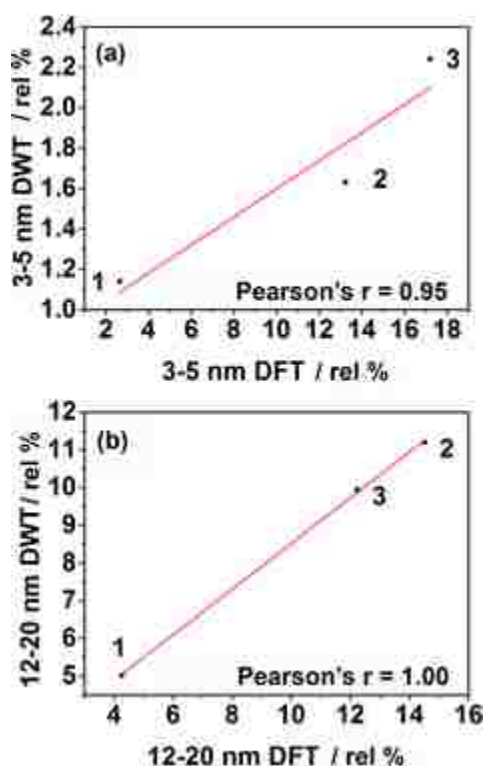


Figure 17. Fraction of surface roughness of selected catalysts 1, 2, and 3 owed to features in size range (a) 3–5 nm and (b) 10–12 nm as calculated using the DWT vs. relative surface area attributable to pores between (a) 3–5 nm and (b) 10–12 nm as determined by the nitrogen adsorption isotherm using the DFT model.

Conclusions

The primary chemical and morphological parameters of PGM-free materials determined as key parameters affecting their integration with enzymes such as bilirubin oxidase (BOx) were presented here. Hybrid catalysts for ORR, composed of PGM-free materials and BOx, possess the high onset potentials of

enzymatic catalysts while retaining the high current densities of PGM-free catalysts.

Analysis of surface chemistry showed that higher nitrogen content in the PGM-free catalyst yielded higher current densities for the hybrid catalysts. The amount of pyridinic nitrogen strongly correlated with catalyst performance. In contrast, the higher amount of pyrrolic type of nitrogen had a negative effect on catalyst performance. The tendency of pyrrolic nitrogen to perform 2 e transfer reduction of oxygen to hydrogen peroxide results in the production of a strong oxidant with the capacity to denaturize the enzyme. The positive effect of total and pyridinic nitrogen is stronger than the negative effect of pyrrolic nitrogen owing to the ability of pyridinic nitrogen to rapidly reduce the hydrogen peroxide intermediate to water. The surface morphology of PGM-free materials was studied using microscopic length-scale separation of SEM images and macroscopic gas adsorption measurements. The results of these two techniques were found to be in good agreement. The higher fraction of pores in a size range of 3–5 nm has a positive impact on the performance of the hybrid catalyst. The chemistry and morphology of PGM-free materials have important roles in increasing the performance of hybrid catalysts. This allows selection and development of better PGM-free electrocatalysts for integration with enzymes and enhanced catalysis.

EFFECT OF PH ON THE ELECTROCHEMICAL ACTIVITY OF IRON-NICARBAZIN DE-RIVED PGM-FREE ELECTROCATALYSTS FOR OXYGEN REDUCTION REACTION.

This chapter corresponds to manuscript that will be submitted to the Journal of the American Chemical Society. This chapter is still under analysis and writing.

Santiago Rojas-Carbonell, Kateryna Artyushkova, Alexey Serov, Carlo Santoro, Plamen Atanassov

Introduction

Fuel cells are electrochemical devices that transform the chemical energy contained into the fuel into useful electricity. Different types of fuel cells are studied and they are categorized in function of: i) operating temperature (low, medium high temperature)¹²⁶; ii) fuel utilized (e.g. hydrogen, methanol, etc)^{127,128}; iii) electrolyte used (e.g. solid polymeric membrane, liquid electrolyte, etc)^{129–131}; iv) working pH (acidic, neutral, alkaline)^{132,133}; v) presence of biotic catalysts (e.g. microbes, enzymes, etc)^{134–136,88,56}

The interesting part that generally unites the fuel cells is the utilization of oxygen as oxidant due to its high availability in atmosphere at practically no additional cost and its high redox potential.¹³² Reduction of oxygen at the cathode is a reaction that is deeply studied in acidic^{11,137}, neutral^{24,138} and alkaline media^{11,139}. Several catalysts are used to accelerate the ORR. Three main groups of catalysts are used: i) Pt and Pt-alloys; ii) carbonaceous metal-free materials; iii) PGM-free with M-N-C.

The first choice is the most used and the most efficient in acidic media^{140–142}. Pt has excellent electrocatalytic activity towards ORR. Unfortunately, Pt is very expensive and cannot be a sustainable and cost-effective choice for large-scale applications (e.g. automotive applications). Moreover, Pt is very sensitive to poisoning or interaction with anions and consequently its intrinsic activity lower with the pH variation from acidic to alkaline media¹⁴³.

Pt is absolutely not a logical solution in working conditions in which pollutants are present (e.g. microbial fuel cells) and the Pt catalyst is subject to a fast degradation and deactivation^{25–27}. At alkaline pH, Pd has actually higher performances compared to Pt but still it does belong to the platinum group metal materials and therefore is not abundant and quite expensive. The high cost is anyway the main reason for which the scientific community is trying to find alternatives through low cost and available materials that have comparable performances compared to platinum¹⁴⁴.

In this direction, two are the main materials have been identified as promising to be further investigated. Those materials are i) metal-free carbonaceous materials^{145,146} and ii) platinum group metal-free carbon-nitrogen rich materials^{11,147,21}. Carbonaceous materials have several characteristics like high surface area, high chemical stability, high electrical conductivity, low cost and commercially available that makes them promising as materials. Those carbonaceous materials are mainly carbon, carbon nanofibers^{145,146,148,149}, activated carbon^{145,146,47,150}, modified carbon black^{145,146,151,152}, graphene^{145,146,153–155}, etc.¹⁵⁶.

Catalytic activity towards ORR unfortunately is quite low in acidic^{145,146} and alkaline media^{145,146}, while in neutral media can be comparable and competitive with platinum group metal-free carbon-nitrogen rich materials^{22,157,28}. Moreover, ORR with carbonaceous materials is more durable than Pt in presence of pollutants. Therefore, carbonaceous materials are mainly used as catalysts support rather than as catalyst material itself.

Platinum group metal-free catalysts are also called M-N-C in which M is an earth abundant transition metals such as Mn, Fe, Co or Ni atomically dispersed with carbon-nitrogen rich matrix^{18,158}. Usually high temperature treatment (pyrolysis) is used to fabricate those materials starting from a metal salt and an organic precursor^{35,6,98,37,30,159-161}. M-N-C catalysts have demonstrated important performances in acidic media¹⁶²⁻¹⁶⁴, outstanding and unprecedented results in neutral media^{158,107,40,45} and comparable and superior performances compared to Pt in alkaline media¹⁶⁵⁻¹⁶⁷. Naturally, those considerations reflect the kinetics of the catalysts with the utilization of rotating ring disk electrode (RRDE) technique^{168,85}. More complicated situation appears to be the integration of the catalysts within the catalytic layer of the membrane electrode assembly (MEA)^{169,170}. This integration seems to be particularly difficult to optimize and it does not pursue the steps usually followed for MEAs with Pt catalysts. M-N-C are very resistant to pollutions in acidic and alkaline media and they showed high resistance to sulfur in neutral media. In neutral media, M-N-C catalysts have been tested in working microbial fuel cells for over 16 months continuous operations with decreases in performances within 35%⁴². At last, M-N-C utilizes

abundantly available transition metals and therefore the cost is significantly low compared to the one of Pt and it could certainly be suitable for scale up and large utilization.

As mentioned before there are three main pH of interest in which fuel cells find applications: proton exchange membrane fuel cell, microbial fuel cells and alkaline fuel cells. ORR follows different reaction mechanisms if the reaction takes place in acidic or alkaline media. In fact, in acidic media, ORR can follow a 2e- transfer mechanism with production of H₂O₂ or a 4e- transfer mechanism with final product H₂O²³. A 2x2e- mechanism can also be done with different sites acting during the reaction as recently shown⁹. H₂O₂ can be further reduced to water through chemical or electrochemical reactions. H⁺ is a main reagent participant to the reaction. In alkaline media, OH⁻ plays an important role to the ORR being a main reagent. Also in this case, the mechanism can follow a 2e- mechanism forming HO₂⁻ + OH⁻ or a direct 4e- with the generation of OH⁻²³. A 2x2e- mechanism can also take place during the reaction^{11,139}. The reaction happening in neutral media is the less studied and probably also the most problematic due to the less availability of H⁺ and OH⁻ at that pH. It is not understood well which mechanisms are involved. Recently, Malko et al. have conducted a pH study on Fe-N-C catalyst and they showed a reaction mechanism of acidic-type till pH 11 and after the mechanism switched to an alkaline-type⁹⁶.

Considering the three type of catalysts identified above, Pt and Pt-alloys have a direct and 4e- mechanism⁷, carbonaceous metal-free catalysts instead have a

2e- mechanism⁴⁷ and M-N-C catalysts can have a 2e-, 2x2e- or 4e-^{18,9}. ORR on M-N-C is quite complicated and very fascinating. In fact, M-N-C catalysts have a multitudinous of active sites that are related with nitrogen and the metal (e.g. pyridinic, pyrrolic, graphitic, metal-nitrogen directly coordinated, etc) that contributes differently to the electron transfer mechanism as showed recently⁹, as well as oxygen species which might be affected by changes in pH¹⁷¹⁻¹⁷⁷. It has not been identified yet the effect of those active sites on the performances of the catalysts at different pHs in which ORR operates. In fact, no positive or negative relationship between catalyst surface chemistry and electrochemistry at different pH has been associated. Up to now, the importance of the chemistry and morphology of the PGM-free catalyst have been identified and studied but the investigations in literature have focus on just one specific pH that is generally 1, 7 and 14. To the best of our knowledge, it has never been presented a study that explains the interaction between change in electrolyte (also in pH) and M-N-C catalyst functioning. Some studies have been carried out on the pH effect on oxygen reduction reaction mechanism of pure platinum^{17,178}, but this results are hard to translate into the PGM-free catalyst, as the existence of multiplicity of chemical species has been well observed.

In this study, Fe-N-C was synthesized using sacrificial support method (SSM) and Nicarbazin as organic precursor. Surface chemistry of the catalyst was measured using x-ray photoelectron spectroscopy (XPS) to identify and quantify the active sites. Electrochemical measurements of the catalyst were done using RRDE in 18 different electrolytes with pHs that varied from 1.11 to 13.5. For the

first time, in this work, a clear relationship between catalyst performances, surface chemistry and working pH is shown. Particularly, the operating pH and therefore the electrolyte composition affect the surface chemistry of the catalyst and consequently the electrocatalytic activity in that specific environment. Four different reaction mechanisms have been identified within the 14 pH unit and correlated with the dissociation constant of the specific catalyst active sites.

Materials and methods

Catalyst synthesis

The PGM-free catalyst used in this study is Iron-Nicarbazin derived and prepared following the sacrificial support method described before ⁷² while making some changes. To prepare it, the following materials were mixed with the respective proportion by weight being: 55.6% nicarbazin (Sigma Aldrich, 98%); 11% of in house prepared Stöber spheres¹⁷⁹; 13.9% of LM-150 fumed silica (CAB-OT); 13.9% of OX-50 hydrophilic fume silica (Aerosil) and 5.6% of iron nitrate nonahydrate (Sigma Aldrich, 99.95%). Once this precursor materials were mixed, DI water was added to make a homogeneous suspension by constant stirring at 45°C and 300 RPMs and was left to dry over a 16-hour period, while keeping stirring. Once this material was dry, it was transferred to an oven set at 85°C to remove the remaining water over a period of 16 hours.

The dry solid mixture was then ground, using agate labware, in a planetary ball mill at 50 Hz for 30 minutes. With this, a fine powder of the precursors impregnated onto the silicon based constituents was achieved, then transferred

into a ceramic crucible, which was beforehand cleaned with nitric acid for 3 days to remove any trace metal it could have.

The subsequent heat treatments (HT) were carried out in a tubular furnace using a quartz tube. The first HT was performed under a reductive atmosphere of 7% hydrogen balanced with nitrogen with a $100 \text{ cm}^3 \text{ min}^{-1}$ flow rate. The temperature of the furnace was left to reach 525°C , after which the quartz tubing containing the crucible with the precursor powder was introduced. The temperature was increased to reach 900°C at a rate of 75°C per minute and then augmented at a smaller rate of 10°C per minute until 975°C . Once this terminal temperature was reached the HT continued for an additional 45 minutes. After this time, the quartz tubing was removed from the furnace and left to cool down at room temperature while keeping the reductive atmosphere.

Once the pyrolyzed material reached room temperature, it was ground in a planetary ball mill at 50 Hz for 30 minutes, using agate labware. This fine powder was then leached for 3 days with a 2:1 mixture of hydrofluoric acid (Solvay, 25%) and nitric acid (Sigma Aldrich, 35%) to remove the silica and metallic particles.

After the etching, the suspension was washed with DI water until the supernatant had a neutral pH and then left to dry at 85°C for 16 hours. Once dry, the leached solid was ground again using the planetary ball mill. This fine powder was then transferred to an acid cleaned ceramic boat and subjected to a second HT. The second HW was carried out under 7% ammonia balanced with nitrogen and a flow rate of $100 \text{ cm}^3 \text{ min}^{-1}$. The temperature of the furnace was stabilized at

975°C, after which the quartz tube containing the sample was introduced and left for 30 minutes. Then, the tube was removed from the furnace and left to cool down to room temperature. The PGM-free catalyst was now ready after carrying out once last grinding in the planetary ball mill.

Electrochemical Measurements

The rotating ring disk electrode (RRDE) technique was used to assess the electrochemical performance of the PGM-free catalyst. A loading of $175 \mu\text{g cm}^{-2}$ of catalyst was reached by depositing onto the mirror polished glassy carbon disk an ink prepared by suspending $5 \mu\text{g}$ of catalyst in $850 \mu\text{L}$ of isopropanol and $150 \mu\text{L}$ of Nafion (0.5% in isopropanol). This loading provided a complete coverage of the glassy carbon.

The electrolytes used were prepared by selecting the appropriate buffer that would provide buffering capacity for the required pH range. The pH values were measured an Orion Star A111 pH meter (Thermo Scientific). The buffers used were the following:

Table 5. Buffers used as electrolytes for each pH value

pH	Constituents	pH	Constituents
1.11	Phosphoric acid	6.08	Potassium biphosphate, potassium dihydrogenphosphate
1.33	Sulphuric acid	7.23	Potassium biphosphate, potassium dihydrogenphosphate
1.6	Perchloric acid	8.36	Potassium biphosphate, potassium dihydrogenphosphate
2.4	Phosphoric acid, potassium dihydrogenphosphate	9.58	Sodium bicarbonate and sodium carbonate
2.8	Citric acid-potassium dihydrogenphosphate	9.8	Boric acid, potassium hydroxide
3.62	Malic acid, potassium hydroxide	10.56	Sodium bicarbonate and sodium carbonate

4.63	Malic acid, potassium hydroxide	11.18	Boric acid, potassium hydroxide
5.2	Acetic acid, potassium acetate	12.48	Boric acid, potassium hydroxide
5.54	Potassium biphosphate, potassium dihydrogenphosphate	13.51	Potassium hydroxide

The RRDE cyclic voltammeteries (CV) were carried out in a 125 -mL electrochemical cell using WEB30-Pine bipotentiostat and a Pine Instruments Rotator (Pine Instruments, Raleigh, NC). A graphite rod was the counter electrode and a sealed saturated Ag/AgCl electrode the reference. For the conversion between the Ag/AgCl electrode to RHE, the appropriate factor of $0.59 \cdot \text{pH} + 0.242$ was added to the measured potential, as it is recommended by the manufacturer (Super Dri- no leak Ref Reference Electrode, World Precision Instruments).

The RRDE was started by saturating the electrolyte with oxygen and then performing a CV for 100 cycles. The potentials were scanned between 0.01 and 1.1 V vs RHE, at 1600 RPM and at a scan rate of 50 mV s^{-1} . After this, the CVs were measured at a scan rate of 5 mV s^{-1} and the rotation speeds were varied from 400 RPM to 2000 RPM in increments of 200 RPM. The RRDE platinum ring was held at a constant potential that would ensure the electrochemical decomposition of hydrogen peroxide into oxygen and protons, serving as a probe for peroxide generation by the PGM-free catalyst located in the disk. From cross-referencing the Pourbaix diagram of hydrogen peroxide with the one of water (to ensure that the potential selected falls within the stability window of water), we were able to determine that the potential of the RRDE ring needed to be 1.1-

0.057*pH vs SHE, which was converted to the Ag/AgCl reference by subtracting the 0.242V difference suggested by the manufacturer.

Chemical Characterization

The PGM-free catalyst surface chemistry was analyzed with XPS. The chemistry of the catalyst after interacting with a subset of the electrolytes was also analyzed. This was attained by adding 100 μ L of the electrolyte to 1 μ g of catalyst and left to interact overnight. The samples were then analyzed in the XPS in a similar manner as for the catalyst alone.

Results And Discussion

Electrochemical Activity

A representative sample of the results obtained from the linear sweep voltammetry tests of the activity towards the oxygen reduction reaction of the PGM-free catalyst under study are presented in Figure 18. From this results it is possible to see that there are substantial changes in the shapes of the linear sweep for the disk. This suggests differences in the mechanisms through the catalytic process is occurring. Nevertheless, it is difficult to clearly discern a trend only from this figure.

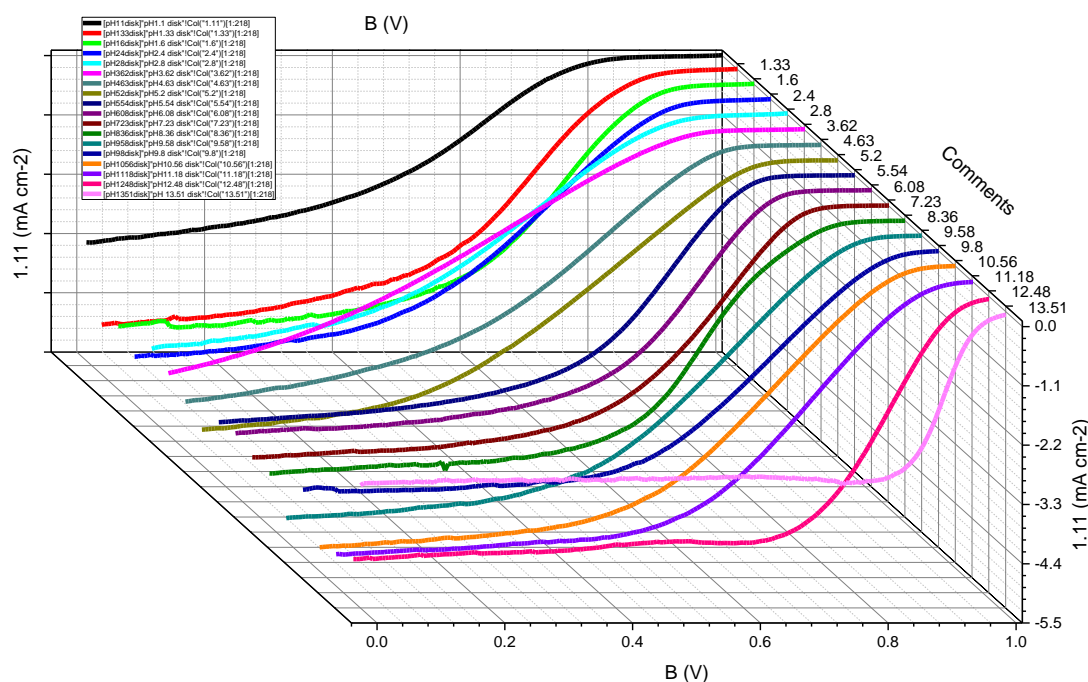


Figure 18. Disc current density vs potential for the electrolytes having different pH values. Scan rate of 5 mV s⁻¹, 1600 RPM and oxygen saturation.

A way to explore these differences in a clearer way consists in determining what is the potential for which a current density of 0.1 mA cm⁻² is reached. These results fall within the vicinity of a kinetic limited region, therefore allowing us to have an assessment of how the kinetics of the electrocatalytic ORR are changing with pH. These results are presented in Figure 19 and show that once the pH dependence on the potential is removed with the conversion to RHE electrode (a), there is still a dependence of the current density with the pH, especially at pH values further away from acidity. There is an expected contribution of the pH change when the potential is reported vs Ag/AgCl electrode (b) which should have a value of 60 mV per pH for a change that is only caused by the pH. In this plot, it is clear that this is only the case for the pH values below 2.4, but then

change to different slopes at higher pH values, indicating a change in potential that is not only dependent on the proton concentration for pH values above 2.4.

The half way potential ($E_{1/2}$) is used also as a parameter to determine the catalytic activity towards the ORR. It was calculated by using the first derivative method and presented in Figure 18(c) and (d). From the ($E_{1/2}$) values, it is possible to evidence again the existence of the four different trends that were seen for the current densities in the kinetic limited region.

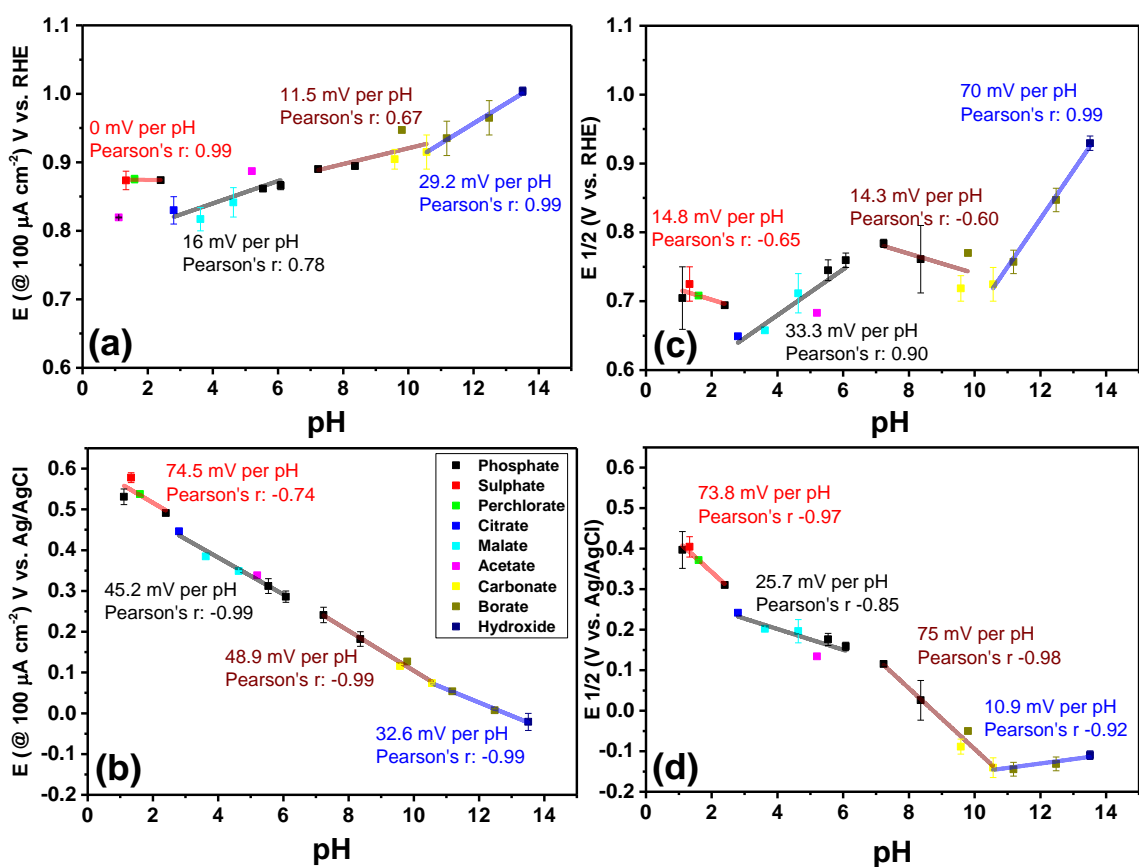


Figure 19. Potential for which the ORR current density reaches 0.1 mA cm^{-2} vs Ag/AgCl electrode (a) and vs RHE electrode (b). Half way potential for the ORR vs RHE electrode (c) and vs Ag/AgCl electrode (d).

Looking into the chemistry of the PGM-catalyst itself helps to understand the origin of such differences in the ORR activity in the PGM-free catalyst when pH is

varied. Several groups^{46,171–175,180} have investigated on the multiple acid dissociation constants (pK_a) that carbon materials that contain oxygen and nitrogen species display. The importance of the pK_a lies in the fact that at pH values higher than the pK_a , that chemical specie will lose its protons and become ionic, increasing the effective concentration of protons in solution. In the opposite manner, at pH values lower than the pK_a , that chemical specie will capture protons, reducing the effective concentration of hydronium ions in the solution. This multiplicity of pK_a values have been associated with the with the different oxygen and nitrogen containing moieties and can be summarized in table 2

In table 2, it is possible to see that the ranges of pK_a values correspond to the shifts in the trends observed in figure 2, as different species lose protons at different stages of pH variation. During the first stage, up to a pH of 2.4, all the functional groups from the PGM-free catalyst are expected to be protonated, with the exception of graphitic nitrogen. In the second stage, which is from a pH of 2.4 to 6.08, there is the successive deprotonation of carboxylic acid and hydroquinone functional groups, leading to an expected pH dependence in way the ORR occurs. Once the neighborhood of pH 6.5 is reached, the pyridinic nitrogen which are located in the edges of the graphitic planes are expected to be deprotonated, leading to an abrupt change in the pH effect on the ORR. The next stage is the one that exists between the pH 7.23 a pH 10.56, when the pyrone type structures and the phenolic groups lose their protons. Lastly, after the pH of 10.56 is surpassed, all the functional groups but the pyrrolic and in plane pyridinic nitrogen, will stay deprotonated, leading to a major dependence of

the ORR with an increase in hydroxyl groups, as the increase in these with pH will not be counterbalanced with any other protons coming from the already deprotonated functional groups.

Table 6. Summary of the possible chemical groups present in the PGM-free catalysts and the associated pK_a values that have been reported.

pK _a	Group	1.1 to 1.6	2.4 to 6.08	7.23 to 9.8	10.56 to 13.5
- 29.46	Graphitic Nitrogen ¹⁸¹	Not H+	Not H+	Not H+	Not H+
2 to 6	Carboxylic ¹⁷⁴	H+	Change	Not H+	Not H+
6.5	Pyridinic (edge) ^{181,182}	H+	H+	Not H+	Not H+
8.5	Lactonic-Pyrone	H+	H+	Change	Not H+
10	Phenolic	H+	H+	Change	Not H+
17.5	Pyrrolic	H+	H+	H+	H+
28.57	Pyridinic (in plane)	H+	H+	H+	H+

Characterization Of Surface Chemistry

In order to quantify the changes in the surface chemical environment of the PGM-free catalyst caused by the variation of pH that were just proposed, a subset of pH buffers was let to equilibrate with the PGM-free catalyst and then the changes in the chemical species were measured using XPS. Other groups have demonstrated that this type of procedure is successful for the determination of pK_a values of the protonated amines and carboxylic groups in biomolecules¹⁸³. Herein we focus on the nitrogen and oxygen species of the PGM-free and on how pH changes affect their relative existence in the surface of the catalysts. Figure 3 shows that changes in the pH of the electrolyte lead to the expected change in the surface species of the PGM-free catalysts. It is important to note the existence of clusters that correspond to the groups identified in Figure 19 by means of electrochemical activity and in table 2 by pK_a ranges. For the case of pyridinic nitrogen (a), the expected increase in their relative percent is seen at pH above the pK_a value of 6.5 that corresponds to this specie. At the same time, there is a rapid decrease at acid pH, due to their acid character at pHs lower than 6.5. This is confirmed by the increase in hydrogenated nitrogen at acid pHs (c), which is the chemical specie to be forming when the pyridinic nitrogen is exposed at acid pHs.

Regarding the nitrogen-iron centers in (c), it is clear that the existence of them is reduced by increased pH values. This points towards the idea that iron centers are attracting the hydroxyl ions.^{7,8} With regards to the graphitic nitrogen (d), its pK_a has been calculated to be well below the acid pHs tested¹⁸¹, removing the

expectation for them to be protonated at any pH. In the other hand, their possible positive charge could be attracting hydroxyls at slightly acid pHs, which is exposed by their progressive diminished number when moving from acid pH towards neutrality, where it reaches the minimum value, indicating saturation.

For the case of the nitrogen oxides (f), there is an increase with the increase concentration of hydroxyl ions.

There is a negligible change in the relative amount carbon single bound to oxygen oxides at most of pH (g). An explanation for this is that they carbon oxides would have the tendency to form phenol type groups at pH values below 10, which is it's pK_a .

The figure (h) points towards the maximum of quinone type structures at a value that has been proposed within the range of $pK_a \approx 4.9$ that has been proposed for this specie. The relative amount carboxylic acid (i) species show a minimum at pH values just above their pK_a range, indicating that this species has been deprotonated at the pH above 6. It is important to mention some of the data points for the oxygen containing structures had to be removed due to the existence of similar species in the buffer used. For this reason, it is better to resort to the potentiometric titration values of this carbonaceous material, which should have similar pK_a values as the ones described in the literature ^{46,180}, which are 4.5, 6.5, 8.5 and 10 and can be assigned to the carboxylic acids, pyridinic nitrogen and pyrone structures.

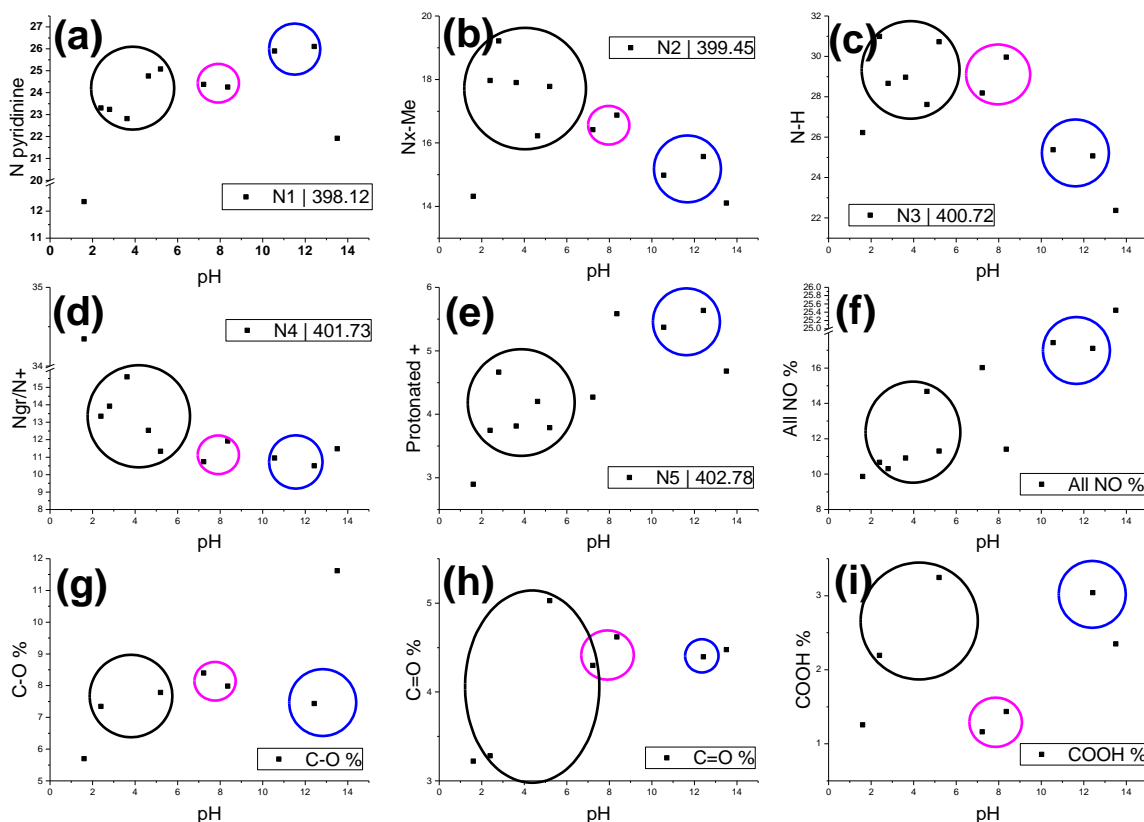


Figure 20. Relative atomic percent of chemical species at different pH: (a) pyridinic nitrogen, (b), nitrogen coordinated with iron, (c) hydrogenated nitrogen, (d) graphitic nitrogen, (e) protonated nitrogen, (f) nitrogen bound to hydroxyls, (g) carbon singly bound to oxygen, (h) carbon double bounded to oxygen and (i) carboxylic acid functional group. Cluster of groups categorized by pH ranges presented in Table 2 are signaled with the respective circle. Black for the range between pH 2.4 and 6.08. Magenta for the range between 7.23 and 9.8 and blue for the range between 10.56 and 12.48.

Now that the origin of the of the different trends observed with change in pH have been traced to changes in the surface chemistry of the PGM-free catalyst, the kinetic and electron transfer parameters for the ORR were calculated.

The kinetic parameters were determined from the Koutecky-Levich equation:

$$\frac{1}{j_d} = \frac{1}{j_k} + \frac{1}{0.62nFC_{O_2}D_{O_2}^{2/3}v^{-1/6}\omega^{1/2}A}$$

Where the disk current density at a specific potential can be used to estimate, what is the kinetic current density after removing the transport limitations represented by the second term of the equation. By plotting the inverse of the disk current density vs. the inverse of the square root of the rotation rate, the intercept of the plot allows to determine the kinetic current density (j_k) and the slope, the overall number of electrons (n) transferred during the reaction. The remaining constants correspond to: Faraday's constant (F) ($96,487 \text{ C mol}^{-1}$), concentration of oxygen in the electrolyte (C_{O_2}) ($1.117\text{E-}6 \text{ mol mL}^{-1}$), diffusion coefficient for oxygen in the electrolyte (D_{O_2}) ($1.9\text{E-}5 \text{ cm}^2 \text{ s}^{-1}$), the angular speed of the RRDE (ω , rad s^{-1}), the cross-sectional area of the glassy carbon electrode (A) (0.196 cm^2) and the kinetic viscosity of the electrolyte (ν), which was measured for each electrolyte using a Cannon Ubbelohde viscometer. The selected potential for all the pH tests was 400 mV vs RHE.

After carrying out the Koutecky-Levich analysis for each pH over the 9 rotation rates, the results kinetic current densities show two trends, displayed in Figure 20(a). There is an apparent pH independent kinetic current density at pH below 4.6, value after which there is a significant one and a half orders of magnitude increase. This seems to correspond with the pK_a value of the carboxylic acid species. After this significant jump in kinetic current density, there seems to be a progressive decrease of it with increased pH values. This results indicate that the change in proton and hydroxyl concentration only plays a significant role in the overall reaction kinetics for pH values that correspond to the equilibrium of carboxylic acid species. With regards the Koutechy-Levich slope (b), there

seems to be two distinctive trends that happen to have as switching point the same pH value as for the one observed for the kinetic current density. Higher values of the Koutecky-Levich slopes correspond to lower overall number of electrons transferred during the ORR, as there is an inverse relationship between the two values as seen from the slope component of the Koutecky-Levich equation. It is possible to see that between the lower pH up until the switching point at a pH of 5.2 there is an increase in the overall number of electrons transferred, indicating a trend to perform the four-electron transfer reduction of oxygen to water. After this pH value, there is a sudden decrease in the number of overall electrons transferred, with the subsequent increase with increase in hydroxyl concentration.

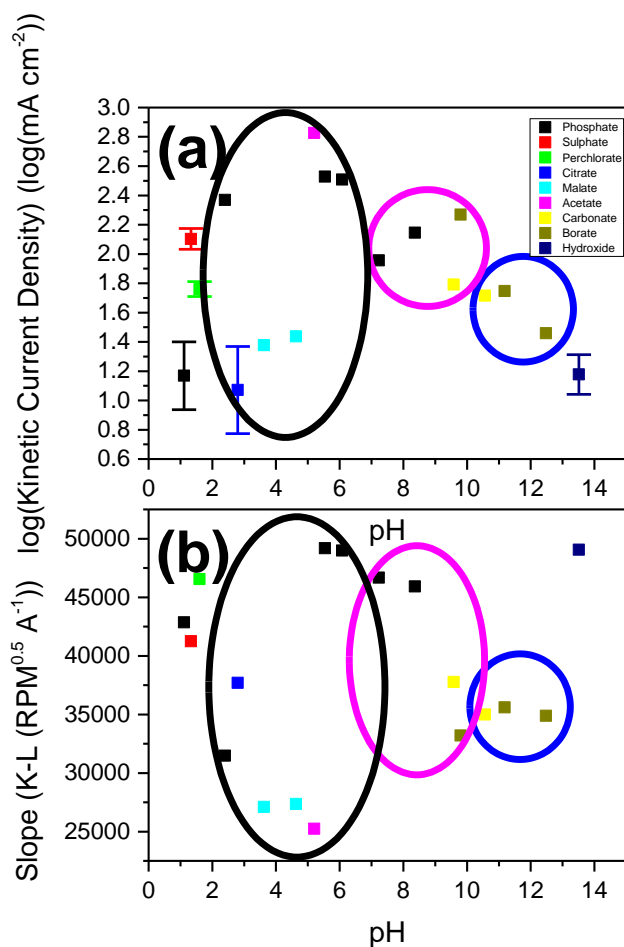


Figure 21. (a) logarithm of the kinetic current density as a function of change in pH. (b) Number of electrons transferred as a function of pH. Circles represent the groups defined in table 2.

The electron transfer parameters were determined for each pH value by using the Tafel plots at the kinetically limited region, located at potentials in proximity to the open circuit potential. The Tafel equation relates the overpotential with the electron transfer coefficient and the exchange current density. The expression is the following:

$$E = E^0 + \frac{2.303RT}{\alpha n_{\alpha} F} \log(j^0) - \frac{2.303RT}{\alpha n_{\alpha} F} \log(j_d)$$

Where a plot of the potential versus the logarithm of the disk current density allows calculating the charge transfer coefficient (α) for the rate limiting step from the slope and the exchange current density (j_0) from the intercept. This results are presented in Figure 22. The other constants from the Tafel equation correspond to: the thermodynamic potential of the ORR (E^0) (1.23 V vs RHE), the universal gas constant (R) ($8.314 \text{ J mol}^{-1} \text{ K}^{-1}$), the temperature (T) (298 K), Faraday constant (F) ($96,487 \text{ C mol}^{-1}$).

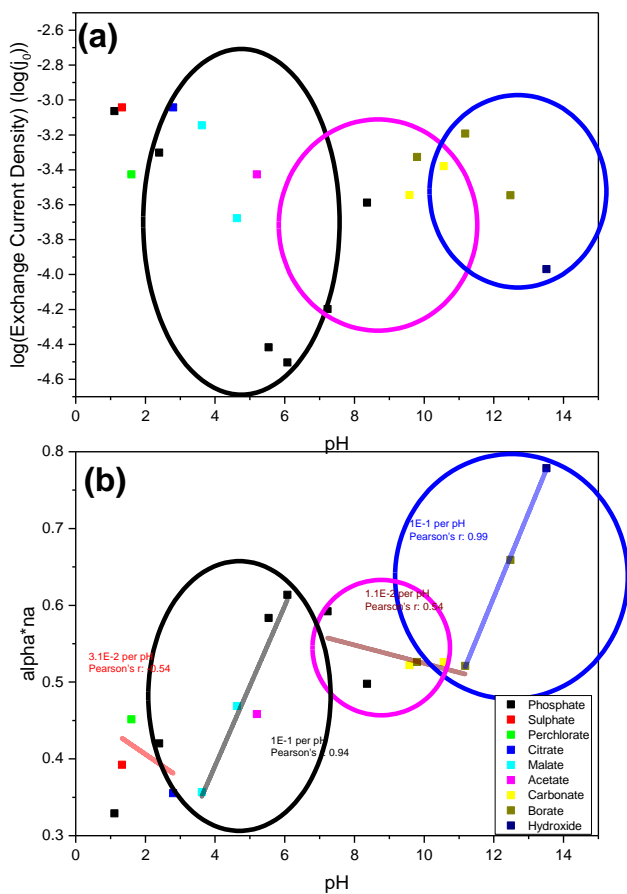


Figure 22. (a) logarithm of the exchange current density vs pH. (b) charge transfer coefficient for the rate limiting step vs pH.

Figure 22(a) indicates that there is a progressive decrease in the exchange current density when moving from acidic pH towards the switching pH of 5.2,

corresponding to the same pH value where the change in kinetic current density is also seen. This decrease in the exchange current density indicates that there is a higher difficulty for the electrons to be transferred between the catalyst and the oxygen molecules. Figure 22(b) presents the electron transfer coefficient, which indicates whether reaction is limited by the proton coupled electron transfer, for the case for values around 0.5 or by the coverage of species in the electrode, for values that tend to one ¹⁸⁴. There is a progressive trend from a proton coupled electron transfer limited reaction at acid pHs towards the surface coverage limitation at alkaline pHs.

A way to contrast the overall kinetic limitation from the electron transfer limitation as a function of pH is presented in Figure 23. The logarithm of the ratio of the kinetic current density and the electron transfer current density show that the kinetic current density is dominating the pH dependence at pH values between 5.54 and 9.8, coinciding with part of the second and most of the third transition region as identified in Table 6.

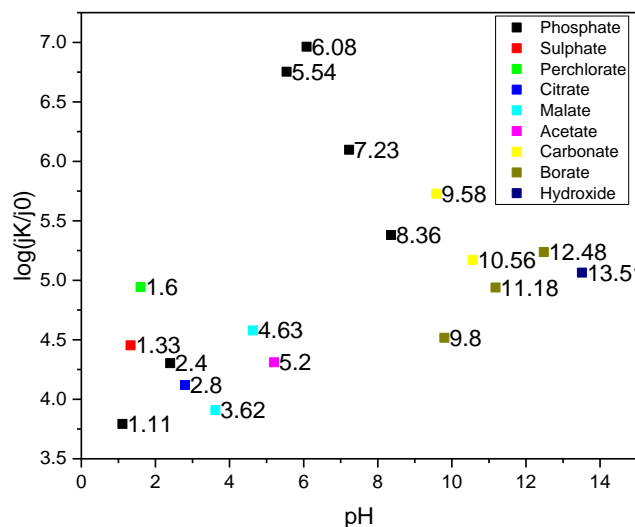


Figure 23. Logarithm of the ratio of kinetic current density and electron transfer current density vs pH.

Correlation Between Surface Chemistry and Electrochemical Activity

It has been proposed that the origin of the catalytic activity of the PGM-free catalyst come from the atomically dispersed iron coordinated with nitrogen, pyridinic nitrogen and pyrrolic nitrogen⁹. Therefore, it is of interest to see what is the correlation that exists between the surface chemistry of the catalyst that has been modified by changes in pH of the electrolyte and the electrochemical activity that it exhibits at that particular pH. Beginning with the relationships seen between the relative number of metallic centers as they were changed by the pH in Figure 24. Studies have found that the Fe-N centers are associated with a direct four electron transfer mechanism. It can be seen that the extremely acidic and alkaline pHs turn into similar amounts of Fe-N (lower than for the other pHs) but possess very electron transfer characters, while having similar kinetic current densities. This could signal that the main difference between the reaction mechanism at acid and alkaline pHs does not come from the overall kinetics of

the reaction but rather from the electron transfer process between the electrode and the surface species.

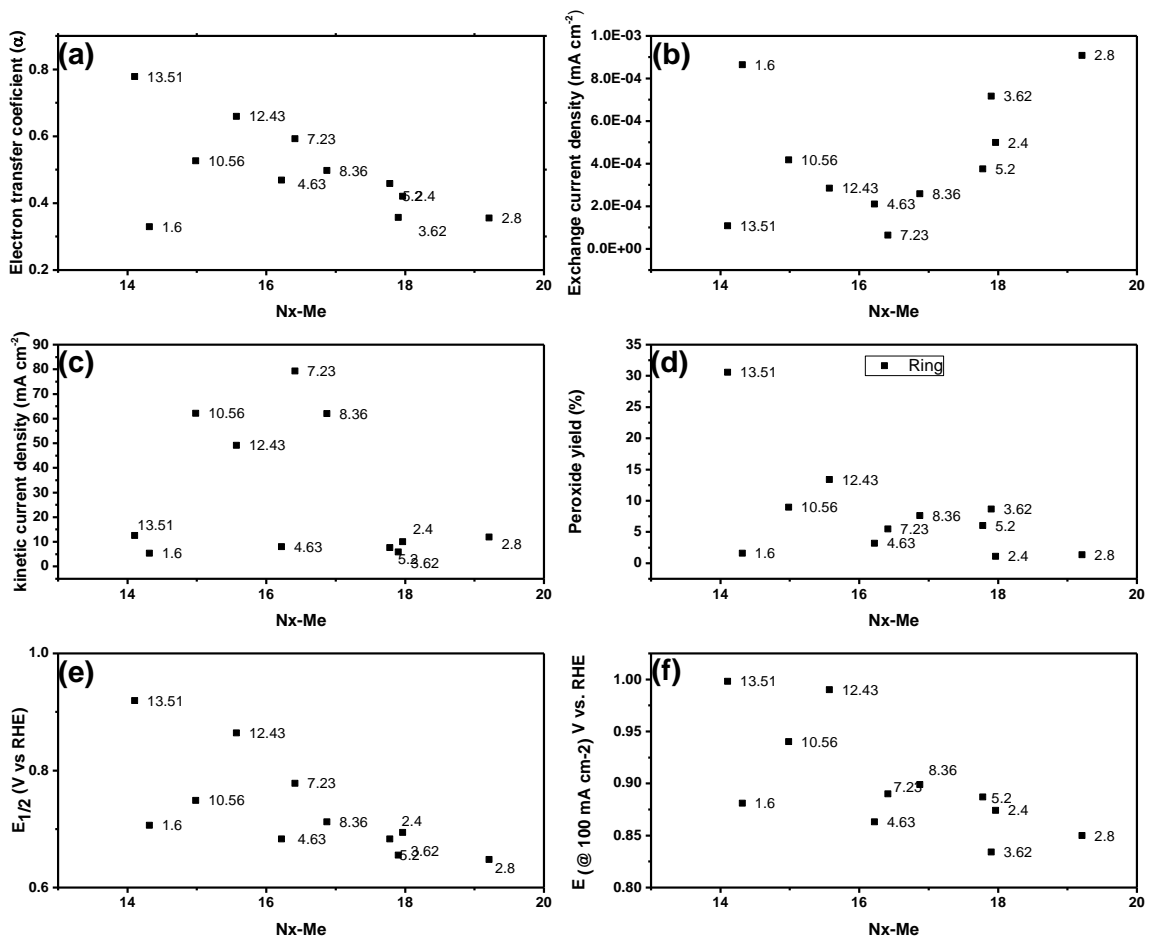


Figure 24. Relative percentage of iron-nitrogen species of the PGM-free catalyst after being exposed to the different pHs vs ORR kinetic and electron transfer parameters. (a) Electron transfer coefficient, (b) Exchange current density, (c) kinetic current density, (d) peroxide yield estimated by the ring current, (e) half way potential and (f) potential at 0.1 mA cm^{-2} .

The Figure 24 (a) shows the electron transfer coefficient moves from values close to 0.5, which are indicative proton coupled electron transferred limited reaction step for higher relative amounts of iron-nitrogen centers, which happen to be in the in the second grouping presented in Table 6 and correspond to slightly acidic conditions. Afterwards, as the pH increases, there is a reduction in

iron-nitrogen species that lead to an increase in the electron transfer coefficient, indicating that the rate limiting step is determined by the surface species concentration at higher pHs. Figure 24(b) a trend that there is a decrease in the exchange current density as the relative number of iron-nitrogen centers is diminished, reaching a minimum value at pH around neutrality.

Figure 24(c) shows clustering in the overall kinetic current densities around the different regions determined by changes in the surface chemistry of the PGM-free catalyst altered by the pH. Figure 24(d) shows an increase in hydrogen peroxide generated from the ORR as the relative number of Fe-N centers is decreased with an increase in pH, this could be an indicator that the ORR is yielding more peroxide as the iron centers are blocked by the higher concentration of hydroxyl ions at higher pHs. Figure 24(e) and (f) show that the half way potential and potential for 0.1 mA cm^{-2} increase with the decrease in Fe-N centers and they form clusters in the same manner as it was proposed by the pK_a values.

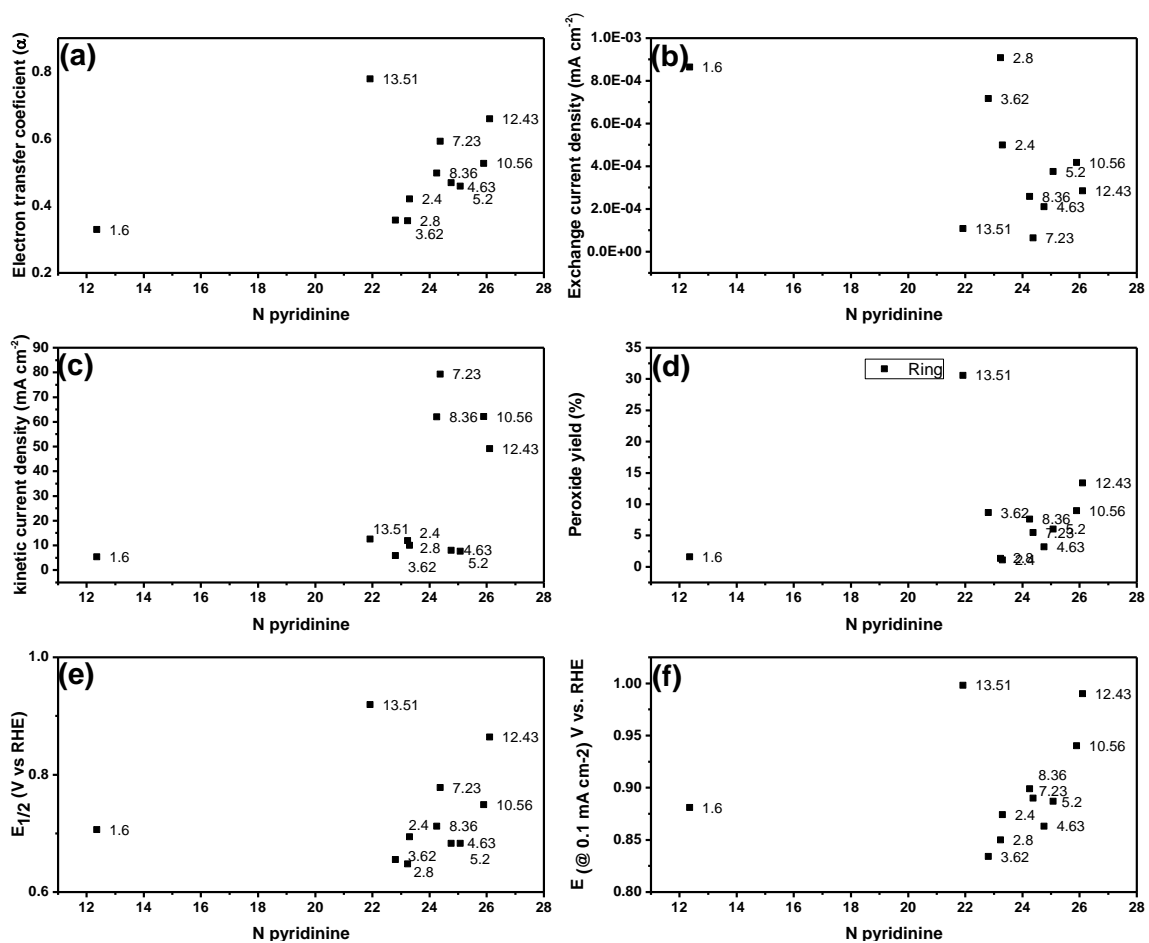


Figure 25. Relative percentage of pyridinic nitrogen of the PGM-free catalyst after being exposed to the different pHs vs ORR kinetic and electron transfer parameters. (a) Electron transfer coefficient, (b) Exchange current density, (c) kinetic current density, (d) peroxide yield estimated by the ring current, (e) half way potential and (f) potential at 0.1 mA cm^{-2} .

The pyridinic nitrogen has been associated with a 2x2 electron transfer process towards the ORR. The plots of the relative amount of pyridinic nitrogen of the PGM-free catalyst as affected by the pH are presented in Figure 25. Here, it is immediately clear that the highly acidic and highly basic pHs have very distinctive relative amounts of pyridinic nitrogen, as well as different kinetic and electron transfer parameters.

From figure 8 (a) it is seen that the electron transfer coefficient moves from an electron transfer limited RDS to a surface species limitation as the relative amount of pyridinic nitrogen is increased. Figure 25(b) shows that small changes in the relative pyridinic nitrogen causes big impact in the exchange current density for the pHs that are located in the within the pH range of 2.8 to 6.08. After this, there is not significant changes in the exchange current density with variations in pyridinic nitrogen, which could be indicating that once the pyridinic moieties get deprotonated at pH around 6.5, they do not have an interaction with the hydroxyl ions from the electrolyte. The kinetic current density from Figure 25(c) indicate a clear clustering in the magnitude of the current density related more with the pK_a region where the pH of the electrolyte falls rather than on the pyridinic nitrogen relative amount. It can be seen that for the pHs for after which the pyridinic moieties are deprotonated, there is a significant increase in the kinetic current density, which gradually decreases as the pH increases. Figure 25 (d) indicates a small variation for the peroxide yield as related with changes in the relative amount of pyridinic nitrogen moieties. With respect to the half way potential and the potential at 0.1 mA cm^2 , there is a trend to increase the ORR activity of the PGM-free catalyst as the pyridinic moieties are increased. This points towards signaling the catalytic activity of the pyridinic nitrogen in the ORR reaction.

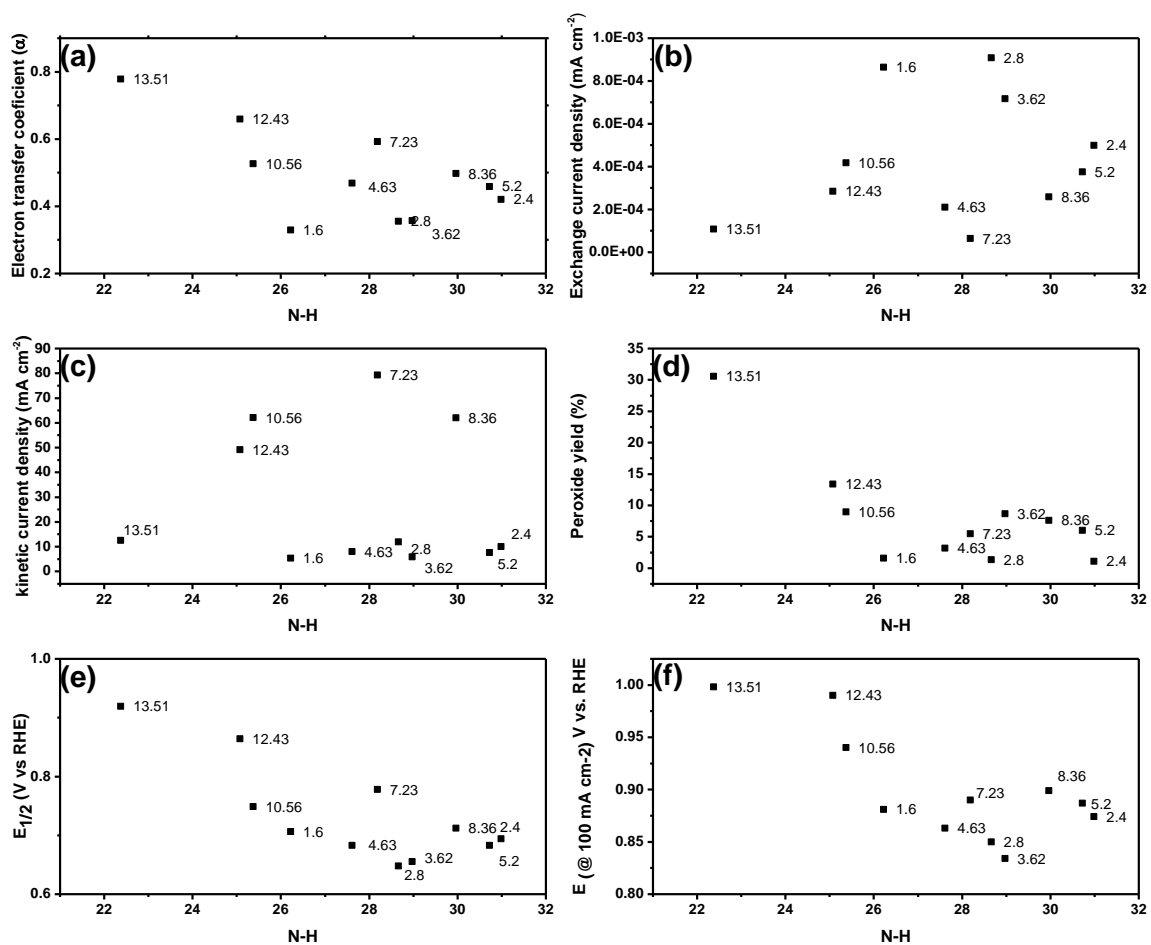


Figure 26. Relative percentage of pyrrolic nitrogen of the PGM-free catalyst after being exposed to the different pHs vs ORR kinetic and electron transfer parameters. (a) Electron transfer coefficient, (b) Exchange current density, (c) kinetic current density, (d) peroxide yield estimated by the ring current, (e) half way potential and (f) potential at 0.1 mA cm^{-2} .

Lastly, pyrrolic nitrogen has been proposed as a moiety that carries out the reduction of oxygen to hydrogen peroxide. The results of Figure 26 relate the changes in relative pyrrolic moieties caused by pH changes and the electron transfer and kinetic parameters for the ORR. Lately, it has been proposed that the pyridinic moieties which possess a proton at pH values below 6.5 would be also identified as pyrrolic. This trend is seen in the plots through Figure 26, as there are trends for pH values of 7.23 and above, whereas no trends for the more acid pHs. The trends that are presented in this figure are strange, this, since the

pyrrolic nitrogen should not change for pH above 6.5, but here is where it actually changes the most and has the biggest effect in the kinetics and electron transfer process. Figure 26 (a) shows that an increase in the pyrrolic moieties lead to a RDS that is more limited by the electron transfer than by the chemical species in the surface. There seems to be not much of effect of pyrrolic moieties towards the exchange current densities (Figure 26(b)). In the case of the kinetic current density shown in Figure 26(c), there is a significant increase in the rate in which the overall ORR proceeds as the relative amount of pyrrolic moieties increases. Figure 26(e) and (f) show that a decrease in the pyrrolic moieties have a positive impact in the activity of the PGM-free catalyst.

Conclusions

In conclusion, the present study shows the effect that pH has in the electrochemical activity of PGM-free catalysts. The change in the concentration of protons and hydroxyls in the electrolyte leads to a change in the surface chemistry of the catalyst itself, as it has functional groups with different acid dissociation constants that might have or not have protons at a certain pH. Based on this multiple pK_a values of the PGM-free catalysts, it was possible to identify the origin of the multiple clusters and trends that exists in terms of electrochemical activity towards ORR and correlate them with the chemical moieties that the PGM-free catalyst possesses and that are active towards the ORR.

List of publications

The publications presented here are the main body of contribution towards my dissertation. Yet, the complete list of the publications where I have made a substantial contribution are the following:

1. **Rojas-Carbonell, S.**, Babanova, S., Serov, A., Artyushkova, K., Workman, M., Santoro, C., Mirabal, A., Calabrese Barton, S., & Atanassov, P., (2017). Integration of Platinum Group Metal-Free Catalysts with Bilirubin Oxidase into a Hybrid Material for Oxygen Reduction Reaction: Interplay of Chemistry and Morphology. *ChemSusChem*.
2. **Rojas-Carbonell, S.**, Santoro, C., Serov, A., & Atanassov, P. (2016). Transition metal-nitrogen-carbon catalysts for oxygen reduction reaction in neutral electrolyte. *Electrochemistry Communications*.
3. **Rojas-Carbonell, S.**, Babanova, S., Serov, A., Ulyanova, Y., Singhal, S., & Atanassov, P. (2016). Hybrid electrocatalysts for oxygen reduction reaction: Integrating enzymatic and non-platinum group metal catalysis. *Electrochimica Acta*, 190, 504-510.
4. **Rojas-Carbonell, S.**, Artyushkova, K., Serov, A., Santoro, C., & Atanassov, P. (2017). Effect of ph on the electrochemical activity of iron-nicarbazin de-rived pgm-free electrocatalysts for oxygen reduction reaction. To be submitted to the Journal of the American Chemical Society
5. Artyushkova, K., Serov, A., **Rojas-Carbonell, S.**, & Atanassov, P. (2015). Chemistry of multitudinous active sites for oxygen reduction reaction in

transition metal–nitrogen–carbon electrocatalysts. *The Journal of Physical Chemistry C*, 119(46), 25917-25928

6. Merino-Jimenez, I., Santoro, C., **Rojas-Carbonell, S.**, Greenman, J., Ieropoulos, I., & Atanassov, P. (2016). Carbon-based air-breathing cathodes for microbial fuel cells. *Catalysts*, 6(9), 127.
7. Santoro, C., Serov, A., Gokhale, R., **Rojas-Carbonell, S.**, Stariha, L., Gordon, J., Artyushkova, K. & Atanassov, P. (2017). A family of Fe-NC oxygen reduction electrocatalysts for microbial fuel cell (MFC) application: Relationships between surface chemistry and performances. *Applied Catalysis B: Environmental*, 205, 24-33.
8. Villarrubia, C. W. N., Soavi, F., Santoro, C., Arbizzani, C., Serov, A., **Rojas-Carbonell, S.**, Gupta, G. & Atanassov, P. (2016). Self-feeding paper based biofuel cell/self-powered hybrid μ -supercapacitor integrated system. *Biosensors and Bioelectronics*, 86, 459-465.
9. Martinez, U., **Rojas-Carbonell, S.**, Halevi, B., Artyushkova, K., Kiefer, B., Sakamoto, T., Asazawa, K., Tanaka, H., Datye, A. & Atanassov, P. (2014). Ni-La Electrocatalysts for Direct Hydrazine Alkaline Anion-Exchange Membrane Fuel Cells. *Journal of The Electrochemical Society*, 161(13), H3106-H3112.

REFERENCES

- (1) Wentworth, K. UNM Fuel Cell Reaches an International Audience :: New Mexico's Flagship University | The University of New Mexico <http://www.unm.edu/features/2013/unm-fuel-cell-reaches-an-international-audience.html> (accessed Nov 14, 2015).
- (2) Pajarito Powder | Fuel Cell Catalysts <http://www.pajaritopowder.com/> (accessed Nov 14, 2015).
- (3) Robson, M. H.; Serov, A.; Artyushkova, K.; Atanassov, P. *Electrochim. Acta* **2013**, *90*, 656.
- (4) Tylus, U.; Jia, Q.; Strickland, K.; Ramaswamy, N.; Serov, A.; Atanassov, P.; Mukerjee, S. *J. Phys. Chem. C. Nanomater. Interfaces* **2014**, *118* (17), 8999.
- (5) Brocato, S.; Serov, A.; Atanassov, P. *Electrochim. Acta* **2013**, *87*, 361.
- (6) Serov, A.; Tylus, U.; Artyushkova, K.; Mukerjee, S.; Atanassov, P. *Appl. Catal. B Environ.* **2014**, *150–151*, 179.
- (7) Ramaswamy, N.; Mukerjee, S. *Adv. Phys. Chem.* **2012**, *2012*, 1.
- (8) Jia, Q.; Ramaswamy, N.; Tylus, U.; Strickland, K.; Li, J.; Serov, A.; Artyushkova, K.; Atanassov, P.; Anibal, J.; Gumeci, C.; Barton, S. C.; Sougrati, M.-T.; Jaouen, F.; Halevi, B.; Mukerjee, S. *Nano Energy* **2016**.
- (9) Artyushkova, K.; Serov, A.; Rojas-Carbonell, S.; Atanassov, P. *J. Phys. Chem. C* **2015**, *acs.jpcc.5b07653*.
- (10) Gumeci, C.; Leonard, N.; Liu, Y.; McKinney, S.; Halevi, B.; Barton, S. C. *J. Mater. Chem. A* **2015**, *0*, 1.
- (11) Shao, M.; Chang, Q.; Dodelet, J.-P.; Chenitz, R. *Chem. Rev.* **2016**, *116* (6), 3594.
- (12) Workman, M. J.; Serov, A.; Halevi, B.; Atanassov, P.; Artyushkova, K. *Langmuir* **2015**, *31* (17), 4924.
- (13) Tripkovic, D. V.; Strmcnik, D.; van der Vliet, D.; Stamenkovic, V.; Markovic, N. M. *Faraday Discuss.* **2009**, *140*, 25.
- (14) Blizanac, B. B.; Ross, P. N.; Markovic, N. M. *Electrochim. Acta* **2007**, *52* (6), 2264.
- (15) Strmcnik, D.; Uchimura, M.; Wang, C.; Subbaraman, R.; Danilovic, N.; van

- der Vliet, D.; Paulikas, A. P.; Stamenkovic, V. R.; Markovic, N. M. *Nat. Chem.* **2013**, *5* (4), 300.
- (16) Blizanac, B. B.; Lucas, C. A.; Gallagher, M. E.; Arenz, M.; Ross, P. N.; Marković, N. M. *J. Phys. Chem. B* **2004**, *108* (2), 625.
- (17) Strbac, S. *Electrochim. Acta* **2011**, *56* (3), 1597.
- (18) Rojas-Carbonell, S.; Santoro, C.; Serov, A.; Atanassov, P. *Transition metal-nitrogen-carbon catalysts for oxygen reduction reaction in neutral electrolyte*; 2017; Vol. 75.
- (19) Song, C.; Zhang, J. In *PEM Fuel Cell Electrocatalysts and Catalyst Layers: Fundamentals and Applications*; Springer London: London, 2008; pp 89–134.
- (20) Antolini, E. *Biosens. Bioelectron.* **2015**, *69*, 54.
- (21) Wang, Z.; Cao, C.; Zheng, Y.; Chen, S.; Zhao, F. *ChemElectroChem* **2014**, *1* (11), 1813.
- (22) Yuan, H.; Hou, Y.; Abu-Reesh, I. M.; Chen, J.; He, Z. *Mater. Horiz.* **2016**, *3* (5), 382.
- (23) Kinoshita, K. (Kim); Electrochemical Society. *Electrochemical oxygen technology*; Wiley, 1992.
- (24) Erable, B.; Féron, D.; Bergel, A. *ChemSusChem* **2012**, *5* (6), 975.
- (25) Minachev, K. M.; Shuikin, N. I.; Rozhdestvenskaya, I. D. *Bull. Acad. Sci. USSR Div. Chem. Sci.* **1952**, *1* (4), 567.
- (26) Santoro, C.; Serov, A.; Narvaez Villarrubia, C. W.; Stariha, S.; Babanova, S.; Artyushkova, K.; Schuler, A. J.; Atanassov, P.; Villarrubia, C. W. N.; Stariha, S.; Babanova, S.; Artyushkova, K.; Schuler, A. J.; Atanassov, P. *Sci. Rep.* **2015**, *5*, 16596.
- (27) Santoro, C.; Serov, A.; Stariha, L.; Kodali, M.; Gordon, J.; Babanova, S.; Bretschger, O.; Artyushkova, K.; Atanassov, P. *Energy Environ. Sci.* **2016**, *9* (7), 2346.
- (28) Zhang, F.; Cheng, S.; Pant, D.; Bogaert, G. Van; Logan, B. E. *Power generation using an activated carbon and metal mesh cathode in a microbial fuel cell*; 2009; Vol. 11.
- (29) Gajda, I.; Greenman, J.; Melhuish, C.; Ieropoulos, I. *Bioelectrochemistry* **2015**, *104*, 58.

- (30) Diodati, S.; Negro, E.; Vezzù, K.; Di Noto, V.; Gross, S. *Electrochim. Acta* **2016**, *215*, 398.
- (31) Di Noto, V.; Negro, E.; Vezzu, K.; Bertasi, F.; Nawn, G. *Interface Mag.* **2015**, *24* (2), 59.
- (32) Negro, E.; Vezzù, K.; Bertasi, F.; Schiavuta, P.; Toniolo, L.; Polizzi, S.; Di Noto, V. *ChemElectroChem* **2014**, *1* (8), 1359.
- (33) Di Noto, V.; Negro, E.; Polizzi, S.; Vezzù, K.; Toniolo, L.; Cavinato, G. In *International Journal of Hydrogen Energy*; 2014; Vol. 39, pp 2812–2827.
- (34) Serov, A.; Robson, M. H.; Halevi, B.; Artyushkova, K.; Atanassov, P. *Electrochem. commun.* **2012**, *22*, 53.
- (35) Serov, A.; Artyushkova, K.; Andersen, N. I.; Stariha, S.; Atanassov, P. *Electrochim. Acta* **2015**, *179*, 154.
- (36) Brouzgou, A.; Song, S.; Liang, Z.-X.; Tsiakaras, P. *Catalysts* **2016**, *6* (10), 159.
- (37) Nguyen, M.-T.; Mecheri, B.; Iannaci, A.; D'Epifanio, A.; Licoccia, S. *Electrochim. Acta* **2016**, *190*, 388.
- (38) Birry, L.; Mehta, P.; Jaouen, F.; Dodelet, J.-P.; Guiot, S. R.; Tartakovsky, B. *Electrochim. Acta* **2011**, *56* (3), 1505.
- (39) Martin, E.; Tartakovsky, B.; Savadogo, O. *Electrochim. Acta* **2011**, *58*, 58.
- (40) Nguyen, M.-T.; Mecheri, B.; D'Epifanio, A.; Sciarria, T. P.; Adani, F.; Licoccia, S. *Int. J. Hydrogen Energy* **2014**, *39* (12), 6462.
- (41) Zhao, F.; Harnisch, F.; Schröder, U.; Scholz, F.; Bogdanoff, P.; Herrmann, I. *Application of pyrolysed iron(II) phthalocyanine and CoTMPP based oxygen reduction catalysts as cathode materials in microbial fuel cells*; 2005; Vol. 7.
- (42) Zhang, X.; Pant, D.; Zhang, F.; Liu, J.; He, W.; Logan, B. E. *ChemElectroChem* **2014**, *1* (11), 1859.
- (43) Lu, G.; Zhu, Y.; Lu, L.; Xu, K.; Wang, H.; Jin, Y.; Jason Ren, Z.; Liu, Z.; Zhang, W. *Iron-rich nanoparticle encapsulated, nitrogen doped porous carbon materials as efficient cathode electrocatalyst for microbial fuel cells*; 2016; Vol. 315.
- (44) Yang, W.; Logan, B. E. *ChemSusChem* **2016**, *9* (16), 2226.
- (45) Santoro, C.; Serov, A.; Gokhale, R.; Rojas-Carbonell, S.; Stariha, L.;

- Gordon, J.; Artyushkova, K.; Atanassov, P. *Appl. Catal. B Environ.* **2017**, *205*, 24.
- (46) Watson, V. J.; Nieto Delgado, C.; Logan, B. E. *Environ. Sci. Technol.* **2013**, *47* (12), 6704.
- (47) Merino-Jimenez, I.; Santoro, C.; Rojas-Carbonell, S.; Greenman, J.; Ieropoulos, I.; Atanassov, P. *Catalysts* **2016**, *6* (9), 127.
- (48) Kattel, S.; Wang, G. *J. Mater. Chem. A* **2013**, *1* (36), 10790.
- (49) Kattel, S.; Atanassov, P.; Kiefer, B. *J. Phys. Chem. C* **2012**, *116* (33), 17378.
- (50) Kattel, S.; Atanassov, P.; Kiefer, B. *Phys. Chem. Chem. Phys.* **2013**, *15* (1), 148.
- (51) Rojas-Carbonell, S.; Babanova, S.; Serov, A.; Ulyanova, Y.; Singhal, S.; Atanassov, P. *Electrochim. Acta* **2016**, *190*, 504.
- (52) Mallela, V. S.; Ilankumaran, V.; Rao, S. N. **2004**.
- (53) Wei, X.; Liu, J. *Front. Energy Power Eng. China* **2008**, *2* (1), 1.
- (54) MacVittie, K.; Halámek, J.; Halámková, L.; Southcott, M.; Jemison, W. D.; Lobel, R.; Katz, E. *Energy Environ. Sci.* **2013**, *6* (1), 81.
- (55) Zebda, A.; Cosnier, S.; Alcaraz, J.-P.; Holzinger, M.; Le Goff, A.; Gondran, C.; Boucher, F.; Giroud, F.; Gorgy, K.; Lamraoui, H.; Cinquin, P. *Sci. Rep.* **2013**, *3*, 1516.
- (56) Atanassov, P.; Apblett, C.; Banta, S.; Brozik, S.; Barton, S. C.; Cooney, M.; Liaw, B. Y.; Mukerjee, S.; Minteer, S. D. *Electrochem. Soc. Interface* **2007**, *16* (2), 28.
- (57) Calabrese Barton, S.; Gallaway, J.; Atanassov, P. *Chem. Rev.* **2004**, *104* (10), 4867.
- (58) Cracknell, J. A.; Vincent, K. A.; Armstrong, F. A. *Chemical Reviews*. 2008, pp 2439–2461.
- (59) Borole, A. P.; LaBarge, S.; Spott, B. A. *J. Power Sources* **2009**, *188* (2), 421.
- (60) Opallo, M.; Bilewicz, R. *Advances in Physical Chemistry*. 2011,.
- (61) Shleev, S.; Shumakovich, G.; Morozova, O.; Yaropolov, a. *Fuel Cells* **2010**, *10* (4), 726.

- (62) Lau, C.; Adkins, E. R.; Ramasamy, R. P.; Luckarift, H. R.; Johnson, G. R.; Atanassov, P. *Adv. Energy Mater.* **2012**, 2 (1), 162.
- (63) Gupta, G.; Lau, C.; Rajendran, V.; Colon, F.; Branch, B.; Ivnitski, D.; Atanassov, P. *Electrochem. commun.* **2011**, 13 (3), 247.
- (64) Gutiérrez-Sánchez, C.; Jia, W.; Beyl, Y.; Pita, M.; Schuhmann, W.; De Lacey, A. L.; Stoica, L. *Electrochim. Acta* **2012**, 82, 218.
- (65) Lopez, R. J.; Babanova, S.; Ulyanova, Y.; Singhal, S.; Atanassov, P. *ChemElectroChem* **2014**, 1 (1).
- (66) Ulyanova, Y.; Babanova, S.; Pinchon, E.; Matanovic, I.; Singhal, S.; Atanassov, P. *Phys. Chem. Chem. Phys.* **2014**, 16 (26), 13367.
- (67) Babanova, S.; Artyushkova, K.; Ulyanova, Y.; Singhal, S.; Atanassov, P. *J. Power Sources* **2014**, 245, 389.
- (68) Tsujimura, S.; Kano, K.; Ikeda, T. *J. Electroanal. Chem.* **2005**, 576 (1), 113.
- (69) Gupta, G.; Lau, C.; Branch, B.; Rajendran, V.; Ivnitski, D.; Atanassov, P. In *Electrochimica Acta*; 2011; Vol. 56, pp 10767–10771.
- (70) Santoro, C.; Babanova, S.; Atanassov, P.; Li, B.; Ieropoulos, I.; Cristiani, P. *J. Electrochem. Soc.* **2013**, 160 (10), H720.
- (71) Jaouen, F.; Proietti, E.; Lefèvre, M.; Chenitz, R.; Dodelet, J.-P.; Wu, G.; Chung, H. T.; Johnston, C. M.; Zelenay, P. *Energy Environ. Sci.* **2011**, 4 (1), 114.
- (72) Serov, A.; Artyushkova, K.; Atanassov, P. *Adv. Energy Mater.* **2014**, 4 (10).
- (73) Ramasamy, R. P.; Luckarift, H. R.; Ivnitski, D. M.; Atanassov, P. B.; Johnson, G. R. *Chem. Commun.* **2010**, 46 (33), 6045.
- (74) Brocato, S.; Lau, C.; Atanassov, P. *Electrochim. Acta* **2012**, 61, 44.
- (75) Ivnitski, D.; Artyushkova, K.; Atanassov, P. *Bioelectrochemistry* **2008**, 74 (1), 101.
- (76) Dos Santos, L.; Climent, V.; Blanford, C. F.; Armstrong, F. a. *Phys. Chem. Chem. Phys.* **2010**, 12 (42), 13962.
- (77) Sebastián, D.; Baglio, V.; Aricò, A. S.; Serov, A.; Atanassov, P. *Appl. Catal. B Environ.* **2016**, 182, 297.
- (78) Chen, R. J.; Zhang, Y.; Wang, D.; Dai, H. .
- (79) Strack, G.; Babanova, S.; Farrington, K. E.; Luckarift, H. R.; Atanassov, P.;

- Johnson, G. R. *J. Electrochem. Soc.* **2013**, *160* (7), G3178.
- (80) Moore, C. M.; Akers, N. L.; Hill, A. D.; Johnson, Z. C.; Minteer, S. D. *Biomacromolecules* **2004**, *5* (4), 1241.
- (81) Cindrella, L.; Kannan, A. M.; Lin, J. F.; Saminathan, K.; Ho, Y.; Lin, C. W.; Wertz, J. *Journal of Power Sources*. 2009, pp 146–160.
- (82) Bidault, F.; Brett, D. J. L.; Middleton, P. H.; Brandon, N. P. *J. Power Sources* **2009**, *187* (1), 39.
- (83) Rojas-Carbonell, S.; Babanova, S.; Serov, A.; Artyushkova, K.; Workman, M. J.; Santoro, C.; Mirabal, A.; Calabrese Barton, S.; Atanassov, P. *ChemSusChem* **2017**.
- (84) Zhang, J. *PEM fuel cell electrocatalysts and catalyst layers: Fundamentals and applications*; Zhang, J., Ed.; Springer London: London, 2008.
- (85) Vielstich, W.; Lamm, A.; Gaseiger, H. A. *Handb. Fuel Cells—Fundamentals, Technol. Appl.* **2003**, *3* (August 2003), 190.
- (86) Pant, D.; Van Bogaert, G.; Diels, L.; Vanbroekhoven, K. *Bioresour. Technol.* **2010**, *101* (6), 1533.
- (87) Pandey, P.; Shinde, V. N.; Deopurkar, R. L.; Kale, S. P.; Patil, S. A.; Pant, D. *Appl. Energy* **2016**, *168*, 706.
- (88) Rasmussen, M.; Abdellaoui, S.; Minteer, S. D. *Biosens. Bioelectron.* **2016**, *76*, 91.
- (89) Leech, D.; Kavanagh, P.; Schuhmann, W. *Electrochimica Acta*. 2012, pp 223–234.
- (90) Du, Z.; Li, H.; Gu, T. *Biotechnol. Adv.* **2007**, *25* (5), 464.
- (91) Minteer, S. D.; Liaw, B. Y.; Cooney, M. J. *Curr. Opin. Biotechnol.* **2007**, *18* (3), 228.
- (92) Rismani-Yazdi, H.; Carver, S. M.; Christy, A. D.; Tuovinen, O. H. *J. Power Sources* **2008**, *180* (2), 683.
- (93) Kim, J.; Jia, H.; Wang, P. *Biotechnol. Adv.* **2006**, *24* (3), 296.
- (94) Zhao, F.; Harnisch, F.; Schröder, U.; Scholz, F.; Bogdanoff, P.; Herrmann, I. *Environ. Sci. Technol.* **2006**, *40* (17), 5193.
- (95) Rabaey, K.; Verstraete, W. *Trends Biotechnol.* **2005**, *23* (6), 291.
- (96) Malko, D.; Kucernak, A. R.; Lopes, T. *Nat. Commun.* **2016**, *7*, 13285.

- (97) Erable, B.; Etcheverry, L.; Bergel, A. *Electrochem. commun.* **2009**, *11* (3), 619.
- (98) Serov, A.; Artyushkova, K.; Niangar, E.; Wang, C.; Dale, N.; Jaouen, F.; Sougrati, M.-T.; Jia, Q.; Mukerjee, S.; Atanassov, P. *Nano Energy* **2015**, *16*, 293.
- (99) Chen, R.; Li, H.; Chu, D.; Wang, G. *J. Phys. Chem. C* **2009**, *113* (48), 20689.
- (100) Kruusenberg, I.; Matisen, L.; Shah, Q.; Kannan, A. M.; Tammeveski, K. *Int. J. Hydrogen Energy* **2012**, *37* (5), 4406.
- (101) Morozaan, A.; Joussetme, B.; Palacin, S. *Energy Environ. Sci.* **2011**, *4* (4), 1238.
- (102) Li, X.; Hu, B.; Suib, S.; Lei, Y.; Li, B. *J. Power Sources* **2010**, *195* (9), 2586.
- (103) Zhang, P.; Li, K.; Liu, X. *J. Power Sources* **2014**, *264*, 248.
- (104) Wang, B. *J. Power Sources* **2005**, *152*, 1.
- (105) Karim, N. A.; Kamarudin, S. K. *Appl. Energy* **2013**, *103*, 212.
- (106) Lefèvre, M.; Proietti, E.; Jaouen, F.; Dodelet, J.-P. *Science* **2009**, *324* (5923), 71.
- (107) Santoro, C.; Serov, A.; Narvaez Villarrubia, C. W.; Stariha, S.; Babanova, S.; Schuler, A. J.; Artyushkova, K.; Atanassov, P. *ChemSusChem* **2015**, *8* (5), 828.
- (108) Ghindilis, A. L.; Atanasov, P.; Wilkins, E. *Electroanalysis* **1997**, *9* (9), 661.
- (109) Gallaway, J.; Wheeldon, I.; Rincon, R.; Atanassov, P.; Banta, S.; Barton, S. C. *Biosens. Bioelectron.* **2008**, *23* (8), 1229.
- (110) Rincón, R. A.; Lau, C.; Luckarift, H. R.; Garcia, K. E.; Adkins, E.; Johnson, G. R.; Atanassov, P. *Biosens. Bioelectron.* **2011**, *27* (1), 132.
- (111) Kang, C.; Shin, H.; Heller, A. *Bioelectrochemistry* **2006**, *68* (1), 22.
- (112) Mano, N.; Kim, H. H.; Zhang, Y.; Heller, A. *J. Am. Chem. Soc.* **2002**, *124* (22), 6480.
- (113) Soukharev, V.; Mano, N.; Heller, A. *J. Am. Chem. Soc.* **2004**, *126* (27), 8368.
- (114) Lopez, R. J.; Babanova, S.; Artyushkova, K.; Atanassov, P. *Bioelectrochemistry* **2015**, *105*, 78.

- (115) Brunauer, S.; Emmett, P. H.; Teller, E. *J. Am. Chem. Soc.* **1938**, *60* (2), 309.
- (116) Barrett, E. P.; Joyner, L. G.; Halenda, P. P. *J. Am. Chem. Soc.* **1951**, *73* (1), 373.
- (117) Anibal, J.; Romero, H. G.; Leonard, N. D.; Gumeci, C.; Halevi, B.; Calabrese Barton, S. *Appl. Catal. B Environ.* **2016**, *198*, 32.
- (118) Leonard, N.; Nallathambi, V.; Barton, S. C. *J. Electrochem. Soc.* **2013**, *160* (8), F788.
- (119) Ustinov, E. A.; Do, D. D.; Fenelonov, V. B. *Carbon N. Y.* **2006**, *44* (4), 653.
- (120) Artyushkova, K.; Pylypenko, S.; Olson, T. S.; Fulghum, J. E.; Atanassov, P. *Langmuir* **2008**, *24* (16), 9082.
- (121) Kothandaraman, R.; Nallathambi, V.; Artyushkova, K.; Barton, S. C. *Appl. Catal. B Environ.* **2009**, *92* (1), 209.
- (122) Milton, R. D.; Giroud, F.; Thumser, A. E.; Minter, S. D.; Slade, R. C. T. *Chem. Commun. (Camb)*. **2014**, *50* (1), 94.
- (123) Milton, R. D.; Giroud, F.; Thumser, A. E.; Minter, S. D.; Slade, R. C. T. *Electrochim. Acta* **2014**, *140*, 59.
- (124) Matanovic, I.; Babanova, S.; Chavez, M. S.; Atanassov, P. *J. Phys. Chem. B* **2016**, *120* (15), 3634.
- (125) Cracknell, J. A.; McNamara, T. P.; Lowe, E. D.; Blanford, C. F. *Dalt. Trans.* **2011**, *40* (25), 6668.
- (126) Larminie, J.; Dicks, A. *Fuel Cell Systems Explained*; 2003; Vol. 93.
- (127) Ryan O'hayre, Suk-Won Cha, W. G. C. *Fuel Cell Fundamentals*; 2016.
- (128) Ogden, J. M.; Steinbugler, M. M.; Kreutz, T. G. *J. Power Sources* **1999**, *79* (2), 143.
- (129) Vishnyakov, V. M. *Vacuum* **2006**, *80* (10), 1053.
- (130) Smitha, B.; Sridhar, S.; Khan, A. A. *Journal of Membrane Science*. 2005, pp 10–26.
- (131) Logan, B. E.; Elimelech, M. *Nature* **2012**, *488* (7411), 313.
- (132) Steele, B. C. H.; Heinzl, A. *Nature* **2001**, *414* (6861), 345.
- (133) Logan, B. E.; Hamelers, B.; Rozendal, R.; Schröder, U.; Keller, J.; Freguia,

S.; Aelterman, P.; Verstraete, W.; Rabaey, K. *Environmental Science and Technology*. 2006, pp 5181–5192.

- (134) Logan, B. E. *Nat. Rev. Microbiol.* **2009**, 7 (5), 375.
- (135) Rabaey, K.; Boon, N.; Siciliano, S. D.; Verstraete, W.; Verhaege, M. *Appl. Environ. Microbiol.* **2004**, 70 (9), 5373.
- (136) Luckarift, H. R.; Atanassov, P.; Johnson, G. R. *Enzymatic Fuel Cells: From Fundamentals to Applications*; 2014.
- (137) Ziegelbauer, J. M.; Olson, T. S.; Pylypenko, S.; Alamgir, F.; Jaye, C.; Atanassov, P.; Mukerjee, S. *J. Phys. Chem. C* **2008**, 112 (24), 8839.
- (138) Schaeztle, O.; Barrière, F.; Schröder, U. *Energy Environ. Sci.* **2009**, 2 (1), 96.
- (139) Olson, T. S.; Pylypenko, S.; Atanassov, P.; Asazawa, K.; Yamada, K.; Tanaka, H. *J. Phys. Chem. C* **2010**, 114 (11), 5049.
- (140) Gasteiger, H. A.; Kocha, S. S.; Sompalli, B.; Wagner, F. T. *Appl. Catal. B Environ.* **2005**, 56 (1), 9.
- (141) Kuzume, A.; Herrero, E.; Feliu, J. M. *J. Electroanal. Chem.* **2007**, 599 (2), 333.
- (142) Ou, L.; Chen, S. *J. Phys. Chem. C* **2013**, 117 (3), 1342.
- (143) Zadick, A.; Dubau, L.; Sergent, N.; Berthomé, G.; Chatenet, M. *ACS Catal.* **2015**, 5 (8), 4819.
- (144) Markovic, N. M.; Schmidt, T. J.; Stamenkovic, V.; Ross, P. N. *Fuel Cells* **2001**, 1 (2), 105.
- (145) Liu, L.; Zhu, Y.-P.; Su, M.; Yuan, Z.-Y. *ChemCatChem* **2015**, 7 (18), 2765.
- (146) Dai, L.; Xue, Y.; Qu, L.; Choi, H.-J.; Baek, J.-B. *Chem. Rev.* **2015**, 115 (11), 4823.
- (147) Ben Liew, K.; Daud, W. R. W.; Ghasemi, M.; Leong, J. X.; Su Lim, S.; Ismail, M. *Int. J. Hydrogen Energy* **2014**, 39 (10), 4870.
- (148) Maldonado, S.; Stevenson, K. J. *J. Phys. Chem. B* **2005**, 109 (10), 4707.
- (149) Liu, G.; Li, X.; Lee, J.-W.; Popov, B. N. *Catal. Sci. Technol.* **2011**, 1 (2), 207.
- (150) Dong, H.; Yu, H.; Wang, X.; Zhou, Q.; Feng, J. *Water Res.* **2012**, 46 (17), 5777.

- (151) Ikeda, T.; Boero, M.; Huang, S. F.; Terakura, K.; Oshima, M.; Ozaki, J. *J. Phys. Chem. C* **2008**, *112* (38), 14706.
- (152) Subramanian, N. P.; Li, X.; Nallathambi, V.; Kumaraguru, S. P.; Colon-Mercado, H.; Wu, G.; Lee, J.-W.; Popov, B. N. *J. Power Sources* **2009**, *188* (1), 38.
- (153) Lai, L.; Potts, J. R.; Zhan, D.; Wang, L.; Poh, C. K.; Tang, C.; Gong, H.; Shen, Z.; Lin, J.; Ruoff, R. S. *Energy Environ. Sci.* **2012**, *5* (7), 7936.
- (154) Arbizzani, C.; Righi, S.; Soavi, F.; Mastragostino, M. *Int. J. Hydrogen Energy* **2011**, *36* (8), 5038.
- (155) Geng, D.; Chen, Y.; Chen, Y.; Li, Y.; Li, R.; Sun, X.; Ye, S.; Knights, S. *Energy Environ. Sci.* **2011**, *4* (3), 760.
- (156) Guo, D.; Shibuya, R.; Akiba, C.; Saji, S.; Kondo, T.; Nakamura, J. *Science* (80-.). **2016**, *351* (6271).
- (157) Santoro, C.; Stadlhofer, A.; Hacker, V.; Squadrito, G.; Schröder, U.; Li, B. *J. Power Sources* **2013**, *243*, 499.
- (158) Kodali, M.; Santoro, C.; Serov, A.; Kabir, S.; Artyushkova, K.; Matanovic, I.; Atanassov, P. *Electrochim. Acta* **2017**, *231*, 115.
- (159) Negro, E.; Di Noto, V. *J. Power Sources* **2008**, *178* (2), 634.
- (160) Ramaswamy, N.; Tylus, U.; Jia, Q.; Mukerjee, S. *J. Am. Chem. Soc.* **2013**, *135* (41), 15443.
- (161) Strickland, K.; Miner, E.; Jia, Q.; Tylus, U.; Ramaswamy, N.; Liang, W.; Sougrati, M.-T.; Jaouen, F.; Mukerjee, S. *Nat. Commun.* **2015**, *6*, 7343.
- (162) Choi, C. H.; Baldizzone, C.; Grote, J.-P.; Schuppert, A. K.; Jaouen, F.; Mayrhofer, K. J. J. *Angew. Chemie Int. Ed.* **2015**, *54* (43), 12753.
- (163) Wu, N.; Wang, Y.; Lei, Y.; Wang, B.; Han, C.; Gou, Y.; Shi, Q.; Fang, D. *Sci. Rep.* **2015**, *5*, 17396.
- (164) Kramm, U. I.; Herrmann-Geppert, I.; Fiechter, S.; Zehl, G.; Zizak, I.; Dorbandt, I.; Schmeißer, D.; Bogdanoff, P. *J. Mater. Chem. A* **2014**, *2* (8), 2663.
- (165) Ge, X.; Sumboja, A.; Wu, D.; An, T.; Li, B.; Goh, F. W. T.; Hor, T. S. A.; Zong, Y.; Liu, Z. *ACS Catal.* **2015**, *5* (8), 4643.
- (166) Gokhale, R.; Chen, Y.; Serov, A.; Artyushkova, K.; Atanassov, P. *Electrochim. Acta* **2017**, *224*, 49.

- (167) Serov, A.; Workman, M. J.; Artyushkova, K.; Atanassov, P.; McCool, G.; McKinney, S.; Romero, H.; Halevi, B.; Stephenson, T. *J. Power Sources* **2016**, *327*, 557.
- (168) Schmidt, T. J.; Gasteiger, H. A. *Handb. Fuel Cells* **2010**, 1.
- (169) Stariha, S.; Artyushkova, K.; Serov, A.; Atanassov, P. In *International Journal of Hydrogen Energy*; 2015; Vol. 40, pp 14676–14682.
- (170) Stariha, S.; Artyushkova, K.; Workman, M. J.; Serov, A.; Mckinney, S.; Halevi, B.; Atanassov, P. *J. Power Sources* **2016**, *326*, 43.
- (171) Arrigo, R.; Hävecker, M.; Wrabetz, S.; Blume, R.; Lerch, M.; McGregor, J.; Parrott, E. P. J.; Zeitler, J. A.; Gladden, L. F.; Knop-Gericke, A.; Schlögl, R.; Su, D. S. *J. Am. Chem. Soc.* **2010**, *132* (28), 9616.
- (172) Kundu, S.; Xia, W.; Busser, W.; Becker, M.; Schmidt, D. A.; Havenith, M.; Muhler, M. *Phys. Chem. Chem. Phys.* **2010**, *12* (17), 4351.
- (173) Leon y Leon, C. A.; Solar, J. M.; Calemma, V.; Radovic, L. R. *Carbon N. Y.* **1992**, *30* (5), 797.
- (174) Brennan, J. K.; Bandosz, T. J.; Thomson, K. T.; Gubbins, K. E. In *Colloids and Surfaces A: Physicochemical and Engineering Aspects*; 2001; Vol. 187–188, pp 539–568.
- (175) Suárez, D.; Menéndez, J. A.; Fuente, E.; Montes-Morán, M. A. *Langmuir* **1999**, *15* (11), 3897.
- (176) Contescu, A.; Contescu, C.; Putyera, K.; Schwarz, J. A. *Carbon N. Y.* **1997**, *35* (1), 83.
- (177) Boehm, H. . *Carbon N. Y.* **2002**, *40* (2), 145.
- (178) Gileadi, E.; Argade, S. D.; Bockris, J. O. *J. Phys. Chem.* **1966**, *70* (6), 2044.
- (179) Stöber, W.; Fink, A.; Bohn, E. *J. Colloid Interface Sci.* **1968**, *26* (1), 62.
- (180) Boehm, H. P. *Carbon N. Y.* **2002**, *40* (2), 145.
- (181) Li, B.; Sun, X.; Su, D. *Phys. Chem. Chem. Phys.* **2015**, *17* (10), 6691.
- (182) Herranz, J.; Jaouen, F.; Lefèvre, M.; Kramm, U. I.; Proietti, E.; Dodelet, J. P.; Bogdanoff, P.; Fiechter, S.; Abs-Wurmbach, I.; Bertrand, P.; Arruda, T. M.; Mukerjee, S. *J. Phys. Chem. C* **2011**, *115* (32), 16087.
- (183) Fears, K. P. *Anal. Chem.* **2014**, *86* (17), 8526.

- (184) Shinagawa, T.; Garcia-Esparza, A. T.; Takanabe, K. *Sci. Rep.* **2015**, *5*, 13801.